Enhancing Wind Farm Wake Recovery Through Kite-Induced Vertical Entrainment

Development and Application of K-TWIST

Timothy van Niekerk

TU Delft

Enhancing Wind Farm Wake Recovery Through Kite-Induced Vertical Entrainment

Development and Application of K-TWIST

MSc Thesis report

by

T.C.J. van Niekerk

To obtain the degree of Master of Science in
Aerospace Engineering
at the Delft University of Technology

To be defended publicly on November 25, 2025 at 09:30 AM

Thesis committee:

Chair:	Dr. ing. R. Schmehl
Supervisors:	Dr. ir. W.A.A.M. Bierbooms
	Dr. ir. D.A.M. de Tavernier
External examiner:	Prof. dr. R. Pecnik

Place:	Faculty of Aerospace Engineering, Delft
Project Duration:	November, 2024 - November, 2025
Student number:	4667395
Date:	November 10, 2025

An electronic version of the thesis report is available at `http://repository.tudelft.nl/`.

Wind Energy Group — Faculty of Aerospace Engineering — Delft University of Technology

Preface

This thesis marks the end of my academic journey at the Delft University of Technology. It has been a challenging yet deeply rewarding experience, allowing me to grow both personally and professionally. After four study switches, five home moves, and a pause during COVID, I returned to Delft with renewed determination and completed my bachelor's degree in Mechanical Engineering. Motivated by a strong interest in renewable energy and sustainability, I stared the wind energy master at the faculty of aerospace engineering.

At first, I would like to express my gratitude to my supervisors, Dr.ir. Wim Bierbooms and Dr.ir. Delphine de Tavernier, for their guidance, patience, and support throughout this project. Wim, thank you for your constant encouragement, insightful feedback, and for remembering me to keep the bigger picture in mind. I would also like to thank Dr. Roland Schmehl for his inspiring lectures on airborne wind energy and for taking on the role of chair of my graduation committee. Your enthusiasm for the field has greatly contributed to my own interest in kite-based systems. Additionally, I would like to extend my gratitude to Prof.dr. Rene Pecnik for stepping in as an external member of my committee at short notice. Your willingness was invaluable in completing the final phase.

Beyond the academic environment, I would like to thank my friends in Delft for their support and companionship during my student days. Thank you for the enjoyable coffee breaks at the faculty, the occasional distractions over beers, and the motivating moments in the gym. To my close friend group from high school, *The Musketeers*, thank you for being there through both happy and difficult times. I am truly grateful to have you guys in my life, you feel like brothers to me.

I owe my deepest gratitude to my family, especially my parents. Thank you for your unconditional support and encouragement. From financial aid, to emotional guidance and helping with yet another move, you were always there for me. Your love and belief in me have made it possible for me to achieve this milestone. Finally, a special heartfelt thanks to my sister, for being there when it mattered most.

Looking back, I feel proud to have completed this journey. It has been a period of professional and personal growth, for which I am deeply grateful. I look forward to the next chapter of my career, using the knowledge and experience gained to contribute towards a more sustainable world in the future.

T.C.J. van Niekerk
Delft, November 2025

Executive summary

Improving the aerodynamic efficiency of wind turbines is essential to lower the cost of renewable energy and speed up the global transition towards a sustainable future. One of the primary sources of energy loss in wind farms is the wake flow generated by upstream turbines, characterized by reduced wind speed and increased turbulence. The wake region diminishes the performance of downstream turbines and can shorten the operation lifetime due to structural fatigue. In 2017, a TU Delft student group introduced an innovative concept to mitigate these wake losses by utilizing tethered kite systems. The kites, flying above the wind farm, generate a lift-induced downwash that enhances the vertical transport of high-momentum air flow towards the wake. By advancing the turbulent mixing process, the wake recovers more swiftly and higher overall wind farm efficiency can be achieved.

This thesis further explores the potential of kite-assisted wake recovery by analyzing the vorticity dynamics in the flow. The study is conducted using the Kite-Turbine Wake Interaction Simulation Tool (K-TWIST), which has been developed as part of the thesis. The solver combines a non-linear lifting-line representation with a free-wake vortex formulation to capture time-dependent effects. The model is extended with a viscous-splitting algorithm, to account for effects due to viscous diffusion and vortex stretching. This mid-fidelity tool captures the unsteady, three-dimensional flow phenomena of the coupled kite-turbine system, while remaining computationally efficient through parallel processing.

The K-TWIST framework builds on a well-established lifting-line free-wake method that has been extensively validated in previous research. Therefore, the study focuses on verifying the numerical behavior within the new framework, rather than validating the theoretical methods once again. Verification tests confirm that the model accurately reproduces key flow phenomena such as vortex roll-up, downwash, and wake contraction, in close agreement with analytical solutions. These results show that the solver provides a solid foundation to study the wake interaction of kite-turbine systems.

To demonstrate the application of K-TWIST in analyzing kite-induced effects on rotor wakes, a case study performed on a scaled NREL-5MW reference turbine. Results show that the kite deployment enhances the transport of momentum in the vertical direction and accelerates wake re-energisation. The work was expanded with a qualitative parametric study on a simplified model to assess the impact of varying kite wingspans. It revealed that larger kites create a stronger effect, although there appeared to be an upper limit. These findings highlight the promising potential of kites as an active wake recovery technique.

Future research should focus on improving the K-TWIST framework and exploring a wider range of kite-turbine configurations. A new version of the solver should include more realistic flight patterns of the kite, variable inflow conditions and further increase the computational efficiency via tree codes or cut-off methods. This opens up new possibilities for optimization studies of the coupled system, maximizing wind farm output and contributing towards a scalable, renewable energy solution.

Contents

Nomenclature

List of Abbreviations

ABL	Atmospheric Boundary Layer
AWE	Airborne Wind Energy
AWT	Airborne Wind Turbine
BEM	Blade Element Momentum
CFD	Computational Fluid Dynamics
CPU	Cental Processing Unit
DNS	Direct Numerical Simulation
FE	Forward Euler Integration Method
FW	Free Vortex Wake
GHG	Greenhouse Gas
HPC	High-Performance Computing
HVM	Hybrid Vortex Method
K-TWIST	Kite-Turbine Wake Interaction Simulation Tool
LES	Large Eddy Simulation
LHS	Left-Hand Side
LLM	Lifting Line Method
LUT	Airfoil Look-up Table
NASA	National Aeronautics and Space Administration
OWEZ	Offshore Windpark Egmond aan Zee
PC	Predictor-Corrector Integration Method
PM	Vortex Panel method
PW	Pre-described Vortex Wake
RANS	Reynolds Averaged Numerical Simulation
RHS	Right-Hand Side
SDG	Sustainable Development Goals
SGS	Sub-Grid-Scale model
UN	United Nations

VLM	Vortex Lattice Method
VM	Vortex Method
VMF	Vertical momentum flux
VPM	Vortex Particle Method
VRM	Vortex Ring Method
VSM	Vortex Step Method

List of Symbols

α	Angle of attack [°]
α_i	Induced angle of attack [°]
α_{eff}	Effective angle of attack [°]
β	Section pitch angle [°]
β_p	Blade pitch angle [°]
β_t	Section twist angle [°]
δ_ν	Effective viscosity diffusion parameter
δ_U	Velocity deficit
$\varnothing_T$	Turbine rotor diameter [m]
ℓ	Straight vortex filament length [m]
ϵ_w	Downwash angle [°]
Γ	Vortex strength (circulation) [m^2/s]
γ_1, γ_2	Vortex filament view angles
Γ_B, Γ_S, Γ_T	Vortex strength of bound, shed, and trailing vortices, respectively [m^2/s]
Γ_v	Tip vortex strength (circulation) [m^2/s]
κ_w	Linear wake expansion rate
λ	Tip speed ratio
μ	Dynamic viscosity [kg/ms]
∇	Gradient operator [$1/m$]
∇^2	Laplace operator [$1/m^2$]
ν	Kinematic viscosity [m^2/s]
ω, Ω	Angular velocity [rad/s]
Ω_R	Rated rotor speed [rad/s]
Φ	Scalar (velocity) potential [m^2/s]
Ψ	Vector (velocity) potential [m^2/s]

ρ	Flow density [kg/m^3]
σ_U	Standard deviation
θ_e	Kite elevation angle [°]
θ_s	Kite sideslip angle [°]
ε	Vortex filament strain
φ_i	Inflow angle [°]
ϑ, φ, ψ	Turbine angles (roll, pitch, yaw) [°]
$\vec{f}$	External body force per unit mass [m/s^2]
$\vec{n}$	Normal vector
$\vec{q}$	Velocity field [$1/s$]
$\vec{r}$	Position vector of Lagrangian marker [m]
ξ_t	Wake age [s]
ξ_ψ	Azimuthal wake age [°]
ζ	Vorticity [$1/s$]
a	Axial induction factor
a_{lo}	Lamb-Oseen constant
a_{sq}	Squire parameter
AR	Wing aspect ratio
b	Wing span [m]
c	Blade chord [m]
C_D	Aerodynamic drag coefficient
C_L	Aerodynamic lift coefficient
C_T	Thrust coefficient
$C_{d,i}$	Induced drag coefficient
D	Aerodynamic lift force [N]
d	Orthogonal distance [m]
E	Aerodynamic lift-to-drag ratio
e	Span efficiency factor
F_a	Aerodynamic resultant force [N]
f_r	Reeling factor
K_v	Regularization parameter
L	Aerodynamic lift force [N]

L'	Lift per unit span [N/m]
N_B	Respective amount of blades or wings
N_D	Number of aerodynamic devices
N_S	Number of spanwise sections on a single blade or wing
N_T	Time step count, defined as a natural number ($\in \mathbb{N}$)
N_{BN}	Total number of blade nodes, combined for the entire simulation geometry
N_{CPU}	Number of CPU cores for parallel computation
N_{tot}	Total number of elements that need to be computed
P	Power extracted by the rotor [W]
p	Pressure [N/m^2]
P_R	Rated power [MW]
q_w	Dynamic wind pressure [N/m^2]
q_θ	Swirl-, tangential velocity [m/s]
q_i	Induced velocity [m/s]
q_i	Vortex-induced velocity [m/s]
R	Rotor radius [m]
r, ϕ, x	Local cylindrical coordinates [$m, °, m$]
r_c	Viscous core radius [m^2/s]
Re_v	Vortex Reynolds number
S	Wing surface area [m^2]
t	Time [s]
T_{tot}	Total simulation time [s]
TI	Turbulence intensity
u, U	Velocity [m/s]
U_R	Resultant wind velocity [m/s]
v_k, v_w, v_a	Kite kinematics: kite, wind and apparent wind velocity, respectively [m/s]
w	Downwash velocity [m/s]
X, Y, Z	Global cartesian coordinates [m]
x, y, z	Local cartesian coordinates [m]

List of Subscripts & Superscripts

$\hat{x}_R$	Non-dimensional distance, normalized by rotor radius R
$\hat{x}_{rc}$	Non-dimensional distance, normalized by core radius r_c

x_0	Initial value at $t = 0$
x_a, x_t	Axial and tangential components, respectively
x_k	Corresponding kite-specific property
$x_{\infty,d}$	Quantity of downwind infinity (far downstream)
x_∞	Quantity at undisturbed, upwind free-stream flow
x_{AC}	Quantity at the wing's aerodynamic center
x_{max}	Maximum value of input parameter, used to define distribution functions
x_{wt}	Corresponding turbine-specific property

List of Figures

List of Tables

Part I

Introduction

1

Motivation

Wind energy plays a crucial role in the global transition to renewable energy sources. Due to its scalability and the continuously technological development, wind energy is considered as the key to reduce greenhouse gas emissions and reach climate goals [1]. Despite its enormous potential, wind turbines cause an aerodynamic wake effect on other turbines in a farm, losing 10% annual energy yield on average [2]. These regions of decreased wind velocity and increased turbulence not only reduce the power production of downstream turbines, but also increase the structural fatigue. Hence, wind farm optimization and wake recovery strategies are of uttermost importance to the energy yield and lifespan of wind farms. The flow of wind turbine wakes is dominated by phenomena such as turbulent mixing and momentum transfer, to recover from the turbine interference and regain energy from the undisturbed airflow [3]. To current day, countess techniques can be found in the literature to tackle this culprit, most of which have been adopted from the aviation sector. Both passive and active wake control strategies, including a diffuser-shroud [4], dynamic induction control (DIC) [5] and wake steering [6], have been investigated extensively with varying degree of fidelity. Conversely, innovative approaches using external devices, including airborne wind energy (AWE) systems, show to be extremely promising and requires more research.

AWE systems are recognized as an emerging wind energy technology, offering several potential advantages in comparison with traditional wind turbines [7]. These novel devices replace only the most efficient part of wind turbines, the blade tip, with a tethered kite flying at high velocities and remove everything else. This opens up the possibility to capture energy-rich flow at even higher altitudes than is currently achievable with traditional turbines, which are limited by the tower foundation. In addition to the promising prospect for electric power production, kites may also be utilized in assisting the wake recovery. As they create a lift-induced downwash and large turbulent structures, kites may enhance flow recovery via vertical entrainment of the high-momentum flow from outer-wake regions. This unique idea originated as a draft during the design synthesis at the Delft University of Technology in 2011, *the Deaolus kite system* [8]. Their conceptual study, solely based on theoretical calculations, showed a promising efficiency gain of 6%. The concept was further refined and translated into a simulation setup for high-fidelity CFD analysis by Ploumakis in 2016 [9]. His research revealed that the projected efficiency improvement was overestimated in the conceptual study, suggesting a more conservative yet noticeable gain of 2%. Due to the significant computational costs of the LES in Ploumakis's work, Kokkedee opted in 2022 to model the kite-turbine effects using a lower-fidelity CFD model, RANS [10]. This acceleration enabled an initial parametric study on the kite, including the surface area, kite altitude, angle of attack and relative positioning. Despite the considerable efforts to find an optimal kite configuration, the RANS simulations failed to accurately model unsteady, dynamic flow phenomena in the wake flow.

In aerodynamic wake modeling, it remains a challenge to find the optimal balance between numerical accuracy and computational efficiency. Experimental methods, such as wind tunnel measurements, and numerical methods, like high-fidelity CFD simulations, are very capable to capturing the most complex three-dimensional unsteady flow phenomena, but they are extremely expensive for conceptual studies and systematic design optimizations. While on the other hand, low-order analytical models or simplified numerical methods, such as the BEM method, are significantly faster yet fail to capture the dynamic flow behavior, as these simplify the wake physics.

Since the primary driver of the kite-induced wake recovery, the vertical entrainment, it is crucial to use modeling technique that is able to represent induced velocities and the evolution of three-dimensional vortical flow structures. Vortex-based methods are particularly suited for this purpose, as they naturally capture phenomena like tip vortex roll-up and downwash. Unlike low-order models, free wake vortex methods explicitly solve the time-evolution of the induced velocity field, making it a strong option to study unsteady effects, like those in the kite-turbine interaction. However, there is no publicly available tool that can model multiple wind turbines and kites within an unsteady, dynamically coupled simulation environment. These limitations motivate the development of a new simulation tool that extends existing vortex-based approaches, providing a more physically representative framework for analyzing kite-induced wake recovery. The resulting model, termed the Kite–Turbine Wake Interaction Simulation Tool (K-TWIST), combines a circulation-based iterative scheme for computing the unsteady distribution of bound circulation with a lifting-line free wake vortex formulation. The solver employs a time-marching Forward Euler scheme coupled with a viscous-splitting algorithm, incorporates the time evolution of the viscous core, and accounts for vortex stretching to capture the three-dimensional dynamics of the wake.

2

Research definition

This chapter lays the foundation for the current study by defining key elements that will guide the research. At first, the current problem of modeling the potential role of tethered kites in mitigating wake losses will be presented. Based on this, the thesis work is delineated in the research objective and the scope of this, including the assumptions and boundaries of the modeling approach. The research is even further articulated into a clear research question that will be answered at the end of the study. This is divided into a small set of sub-questions to break down the work into more specific, manageable parts, that collectively support the answer to the main question. With clearly defined research elements, the stage is set for further methodological development and analysis. The chapter is concluded with the thesis outline, providing the structure of the report for quick access to relevant information.

2.1. Problem statement

State-of-the-art wind farm operations suffer major losses in energy yield and revenue as a consequence of wind turbine wake effects. These flow regions of reduced velocity not only affects the power extraction for downstream turbines in the farm, but also increase the turbulence phenomena that lead to fatigue. In order to mitigate these wake effects, researchers have proposed several wake recovery strategies to tackle the culprit, both actively and passively. While most methods focus on modifying the turbines themselves, more recent efforts have proposed to use airborne kite systems as a potential external solution. This novel concept offers the possibility to re-energize the flow and enhance wake recovery by means of the principle of vertical entrainment. Previous work on the topic has been based on purely theoretical models or on with high-fidelity CFD simulations. Despite the promising results from the LES simulations, it was not possible to conduct a large parametric study on the kite due to the extreme computational costs. The later work using RANS was significantly faster but failed to reproduce the LES findings, indicating that key dynamic flow interactions between the kite and turbine were not captured. These limitations inspired the current research, which investigated the kite-induced effect on wake recovery using vortex-based methods. This mid-fidelity approach offers a strong balance between computational efficiency and the numerical accuracy. It provides both a valuable new source of comparative data in relation to standing methods, as well as a practical tool for accelerated kite-turbine simulations. The latter opens up the possibility for exploration of numerous kite configurations through parametric studies.

2.2. Research Objective

The main objective of this research is presented in the text box below. The aim here is to create a simulation framework that can serve as a starting point for future parametric and optimization studies on the kite-induced wake reduction. It should be noted that the original plan was to use an existing vortex-based model, such as openFAST or Q-Blade, to conduct a first parametric study. However, as there was no suitable model available to model the kite-turbine interaction, a different model had to be developed from scratch. This shifted the focus to the development of the K-TWIST model and the verification of its accuracy and applicability.

Research objective:
Develop and validate a new lifting-line free wake vortex tool to investigate the effect of kite deployment on the flow recovery of wind turbines wakes.

2.3. Scope of study

The scope of this research is limited to the development and verification of the K-TWIST model and its application to simplified kite-turbine configurations. All work in this study is conducted on the wake of a single turbine under steady, uniform axial inflow conditions. Effects due to wind shear, ground effects, atmospheric stability, yaw-misalignment, aero-elasticity and farm-scale flow interactions are not considered.

It should be noted that the turbulence intensity is not modeled explicitly. Instead, its influence is represented by an average apparent parameter, which is included in the temporal evolution of the viscous core radius. The kite's dynamics will be simplified to a rigid, untwisted wing in straight flight. Since the principle of downwash is considered as the main driver of the kite-turbine flow interaction, the simplistic kite model is sufficient for a first study on the subject.

This research provides a novel simulation tool that can be used to simulate and optimize future designs of hybrid kite-turbine systems, potentially contributing to improved wind farm efficiency. The model is constructed in basic building blocks such that it can be extended to more complex methods where necessary.

The work includes a comprehensive verification of the numerical implementation. This includes configuration tests, sensitivity analyses of both numerical and physical input parameters, as well as an investigation of performance and efficiency in parallel computations. The underlying methods of the K-TWIST model are validated against reference results. In order to demonstrate the potential use of the model, a case study is conducted on the kite-induced effect on the wake from a scaled version of the NREL-5MW wind turbine. At last, a qualitative parameter variation on the kite's span is included to show the tool's capability for future parametric studies.

2.4. Research Question

The research question is the outcome of the extensive literature review on wake recovery, previous work on kite utilization and consultation with the supervisors. The research question for this thesis is outlined as follows:

Main research question:
To what extent can kites be deployed to enhance wind turbine wake recovery and improve the overall wind farm efficiency?

As this research question is considerably broad and consists of multiple underlying elements, it is split up into five smaller sub-questions. Each individual sub-question encompasses one of these elements and provides a more detailed view of the main question at hand. The results of these sub-questions will help support the answer to the core question, in order to achieve the research objective.

1. How accurate are vortex methods to model the aerodynamic interactions between the kite and wind turbine in comparison with reference data?
2. What numerical and physical input parameters influence the convergence and stability of the developed model?
3. What are the computational limitations and performance characteristics of the developed framework?
4. How does the kite's presence influence the flow behavior in the wake of a wind turbine?
5. What is the optimal configuration of the kite for wake re-energisation?
6. How does the kite-turbine integration affect the overall wind farm energy efficiency?

2.5. Thesis outline

This thesis work is structured into five parts, where *Part I* provides the introduction of the paper. Chapter 1 briefly introduces the topic with some background information on wind energy, turbine wakes and the previous work on the subject. Chapter 2 follows with the research framework, including the problem statement, research objective, questions and scope, and closes with the general structure of the thesis.

Part II provides a comprehensive literature review, covering a wide range of relevant topics. Chapter 3 discusses the global importance of renewable energy in addressing the climate crisis and reaching global sustainability goals. Chapter 4 describes the wake flow behind wind turbines, including their formation, characteristics and key influencing factors. Chapter 5 outlines existing strategies to mitigate wind turbine wake effects, divided into three main branches: passive, active and external solutions. Chapter 6 introduces the topic of airborne wind energy systems (AWEs), the kite aerodynamics and their application for wake recovery via the principle of vertical entrainment. Chapter 7 provides a complete overview of wake modeling techniques, ranging from experiments, to (semi-)analytical, numerical and data-driven methods. Subsequently, Chapter 8 delves deeper into vortex-based modeling techniques and its ability to capture unsteady, dynamic flow behavior. To finalize the literature review, Chapter 9 summarizes relevant results from previous work using theoretical calculations, as well as high-fidelity CFD analysis.

Part III presents the methodology of the **K**ite-**T**urbine **W**ake **I**nteraction **S**imulation **T**ool (K-TWIST). Chapter 10 describes the development of the modeling tool, from vortex theory to the numerical implementation and the post-processing techniques to extract meaningful wake metrics for comparative analysis.

Part IV contains the research results and analysis. Chapter 11 shows the verification and validation of the new solver, covering consistency checks, configuration trials and sensitivity studies on both critical input parameter and hardware conditions. In Chapter 12 the K-TWIST model is used to conduct a case study on the kite-induced effect on wind turbine wakes. Here, the NREL-5MW reference wind turbine is scaled down to a 2MW version to mimic the simulation setup of the previous CFD studies. The simulation result of the turbine in isolation is compared with the kite-turbine configuration, in order to investigate its effect on the wake recovery. These downstream performance gains are then compared with previous research and any differences are discussed.

Finally, *Part V* concludes this thesis work. Chapter 13 summarizes the main research findings and addresses the research questions. Chapter 14 closes the paper by providing recommendations for future research work, identifying opportunities to improve the K-TWIST model or configuration setups that may be relevant to further investigate the concept of *the Deaolus kite system*

Part II

Literature Review

3

Global importance of renewable energy

That we need to become more ”sustainable” is by now well known among the average Joe, but there is still some debate about what this entails in practice. Sustainability is defined as achieving our goals without compromising the ability of future generations to meet their needs [11]. To help guide the transition, at the Earth Summit in 1922, international organizations have agreed to collectively tackle the human interference with the earth's system [12]. This meeting led to the 17 sustainability development goals (SDGs) in 2015, which addresses the most important global issues concerning poverty, hunger, inequality, health and climate [13]. Later that year, the United Nations have established the Paris agreement, limiting the temperature increase to 1.5° above pre-industrial levels [14]. To achieve this goal, the global GHG emission need to be halved by 2030 and net-zero by 2050 [15].

The transition to renewable energy sources has become inevitable to mitigate climate change and secure a sustainable future for following generations. As seen in Figure 3.1, the main culprit here is the combustion of fossil fuels for electricity and heat [16]. This extremely polluting production accounts for no less than 32% of the global GHG emissions. In the year 2021, over 50 billion tonnes of CO_2-equivalent were emitted worldwide, corresponding to a staggering 6 tonnes per person [17]. Whereas forecasting studies at the start of the millennium anticipated 2025 as the peak year, current data show that this is far from reality. Despite major initiatives in developed countries to cut the emissions, we are still on an upward trend. This rise is mainly due to population growth, increased energy demand per capita and the industrialization in emerging economies, such as China and India.

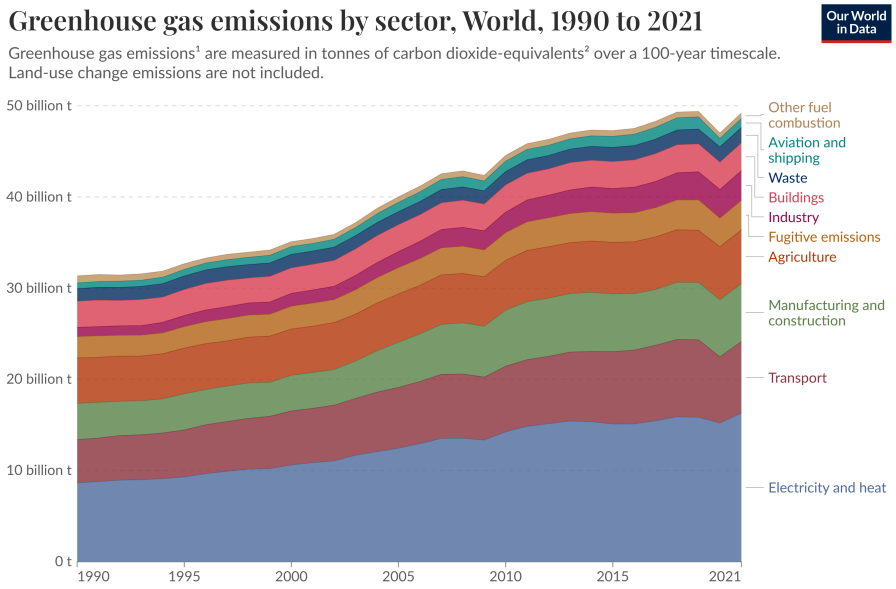

Figure 3.1: Development of global GHG emissions by sector, from 1990 to 2021 [16]

Although opinions widely differ, studies from NASA have shown that climate change is not a problem of the future. The human-caused effects of global warming are already being observed today and will grow exponentially [18]. Growing wind speeds, causing an increase in hurricane frequency and intensity [19] in the United States; Rising sea level, causing increased flood risk around the Mediterranean Sea [20]; yet another record on the highest temperature measured, intensifying the drought in the Amazon [21] and Europe [22] as well as significant increase of forest fires in India [23]. This can also be seen in the ever-rising line of natural disasters from the International Disaster Database, where the number has quadrupled since 1970 [24]. The hard facts emphasize once again the climate problem is not a distant concern, but a present-day reality.

The depletion of global fossil fuel supply and the long-term energy security demand, create additional pressure on the transition to low-carbon energy systems. Key energy sectors, including buildings, transport and industry, are already engaged in electrification. This even further increases the demand for green electricity. Although it is a great vision to use only renewable sources for all our future energy applications, the electricity production is currently far from clean. From data of the Energy Institute [25] and Ember [26], 60% of the electricity is produced from fossil fuels, and only 20% comes actually from renewable sources. The question remains whether this detour is truly better than using it directly.

Renewable energy resources are defined to come from natural origin and to replenish faster than it can be used on a human time-scale [1]. They can be divided into categories, based on their natural resource: wind, solar radiation, hydropower, biomass, geothermal and ocean energy. With the limitation of available hydropower and ocean energy due to geographical features and solar energy already being on track to hit the expectations of the energy goals of 1.5 deg, the focus is on expanding the wind energy sector. However, the annual additions of onshore wind farms is way off track, due to high inflation rates, permit delays and un-supportive governmental policies [27]. In addition, the prospects of offshore wind turbines are falling behind as well [1]. The most optimal spots, the locations close to shore, are beginning to run out. Developments are already occurring to places the turbines further at sea by support on floating structures [28], but this is not nearly as fast and as much as needed. Therefore, it is of significant importance that the wind farms that do can be placed are then entirely optimal in their energy production. This motivates further research into wake recovery strategies and wind farm optimization.

4

Wind Turbine wakes

With the development of wind turbines as a fully renewable source of energy, it was thought to be the solution to climate change by generating clean electricity without any emissions. Wind turbines, originating from the wind mills used to grind grain in the first centuries, extract kinetic energy from the wind and convert it to electricity via mechanical energy of the rotor shaft. From the law of conservation of energy, the total energy in a closed system needs to remain constant over time. Therefore, where energy is generated, energy must be lost somewhere else. In simple terms, for wind turbines this happens by slowing down the air behind the rotor, creating an area of decreased velocity, the velocity deficit (Eq. 4.1). As the airflow outside of the rotor area sees no blockage of the flow, at the edge of the rotor disk, the blade tip, an instability develops. This creates a turbulent flow of vortices, which are suctioned in the low-pressure area behind the rotor. The region of disturbed flow behind a turbine is called the wake. A similar phenomenon can be found while sailing a boat. When you look behind the motor of the boat, a Kelvin wake pattern is created due to density differences and gravity. In airflow, this phenomenon is caused by viscosity, the dynamic resistance of changing shape. The effect can be visualized by putting a cylinder in line with the fluid flow. The flow perceives the cylinder as an obstruction, causing the flow to go around the cylinder. Just behind the cylinder there is no flow, causing a pressure difference to suctioning of air in the gap. At the edge of the cylinder, vortices are produced and are shed periodically behind the cylinder, creating the well-known von Kármán vortex street. However, the wakes behind a wind turbine are far more complex, since the vorticity arises from the rotational motion of the blades rather than the regular formation of vortex shedding behind bluff bodies.

When a turbine is placed inside the wake of another turbine, it can no longer operate in optimal conditions. Due to the presence of the upwind turbine, it perceives a lower incoming wind speed and a higher level of turbulence, producer less energy than in isolation. Turbine wakes can extend to a very long distance downstream of the rotor before completely returning to the free-stream conditions. Due to space optimization in most wind farms, turbines cannot be placed in full solitude and are often in line with multiple other turbines. If the wakes are not taken into account properly, the energy yield of the wind turbine can be overestimated significantly. Depending on the distance between subsequent turbines, the losses can go up to a substantial 50% in isolation [29]. For large wind farms, like Horns Rev, Lillgrund, and Nysted, research shows an average power loss of the order of 10% [2]. Wake losses will not only cause reduced revenue, but also cause a too high demand of essential equipment, such as generator and cable capacity. Therefore, it is extremely important to map wake effects correctly when modeling a wind farm.

Wake physics

The wake behind a wind turbine can be described by splitting the downstream wake in three regions, as seen in Figure 4.1: near-, intermediate-, and far wake. The near wake region is fully characterized by the initial conditions, like blade aerodynamics, tip vortices, tower blockage. Here, the flow is mostly dominant by inviscid processes and the fluid motion can be described by the Euler equations. At the root and the tip of the blade, helicoidal vortices are shed due to a pressure difference between the two sides of a rotor blade. This phenomenon of tip and root vortices creation has been researched extensively already over the years, where the focus lied on the more impactful tip vortices. Also, their stability and the breakdown mechanisms are greatly studied. The wake extends until the maximum velocity deficit is reached at the center line and the pressure has reached the same value as the free-stream. Often, it is assumed that the near wake region stretches out to approximately two rotor diameters (2D) behind the rotor [3]. When the flow reaches the intermediate wake region, a shear layer develops between the free-stream flow and the wake. The shear layer is a tiny region of strong vorticity and large velocity gradients [30]. As the flow in the wake region moves significantly slower than that of the free-stream, a gradient occurs, causing shear stresses. Here, turbulent structures, eddies, start to form at the edge of the wake and the flow starts to mix. The vortices are broken down into smaller vortices and slowly move to the center line. At approximately 6D, the influence of the rotor has disappeared and the wake enters the far wake region. From this point, the wake is considered to be fully developed and the flow is assumed to be axisymmetric, self-similar and shows a Gaussian profile. The velocity will continue to increase asymptotically to the initial free-stream conditions.

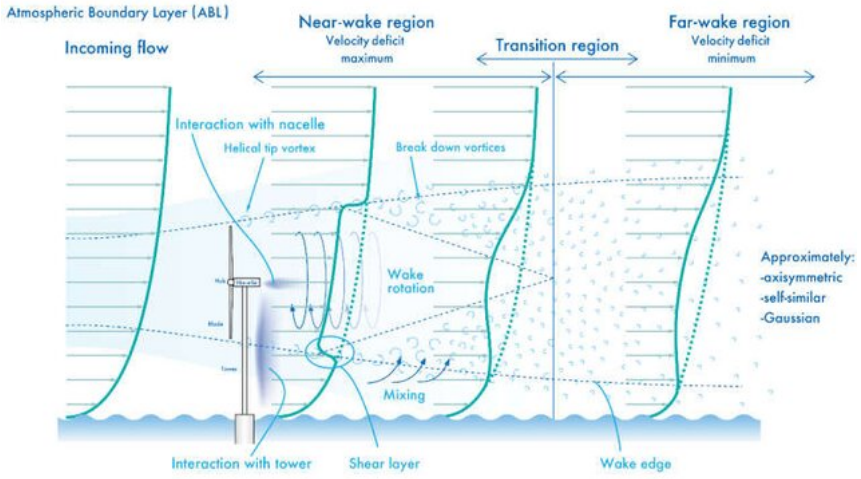

Figure 4.1: Schematic diagram of wind turbine wake regions in the atmospheric boundary layer (ABL) [31]

The interaction of turbulent flow structures can be explained by the theory of turbulence energy cascade of the atmospheric boundary layer. A visual representation of the basic principles is presented in Figure 4.2 Large turbulent eddies are produced due to instabilities in the flow. These eddies, also called vortices, will roll up, merge together and create large vortical structures. The shear layers inside these structures will roll up again, forming new vortices on a smaller scale. In this process, turbulence energy is transferred to the smaller scale structures, which is referred as the energy cascade. This will proceed to even smaller scales and at the smallest scale, the vortices dissipate and the turbulence energy is scattered and dissipated into heat.

Turbulence is chaotic, irregular, anisotropic fluid behavior that occur in situations with high Reynolds number, where the inertial forces of the fluid are more dominant than the viscous forces [32]. The strength of turbulence, the turbulence intensity (TI), is defined as the standard deviation of the wind velocity component divided by the average free-stream wind speed at hub height (Eq. 4.2). It is an effective statistical measure of the fluctuation level during a time interval. The increased turbulence in the wake creates a less uniform inflow for downstream turbines. This generates additional low-and high-frequency fatigue loading on the rotor blades. Dependent on the surface roughness, atmospheric stability and the spacing, turbulence causes wake-induced fatigue damage and can substantial impact the life-time [33],

[34].

Another important parameter in wake dynamics is the momentum flux, quantifying the rate at which momentum is transferred across a surface. For wind turbines, it provides a measurable quantity for evaluating mean kinetic energy entrainment, which is strongly related to wake recovery. It can represent either the mean flow transport or isolate the contribution from turbulent eddies, which is equivalent to the Reynolds stress commonly used in CFD analysis. Of particular interest for this study is the vertical momentum flux, as defined in Eq. 4.3, which characterizes the vertical transport of axial momentum. In other words, it quantifies how horizontal momentum is transferred from the faster moving, undisturbed flow above the wind turbine into the wake region. Since the incoming free-stream air has a higher axial velocity, hence a higher momentum, downward transport from this flow region will contribute to enhanced wake recovery.

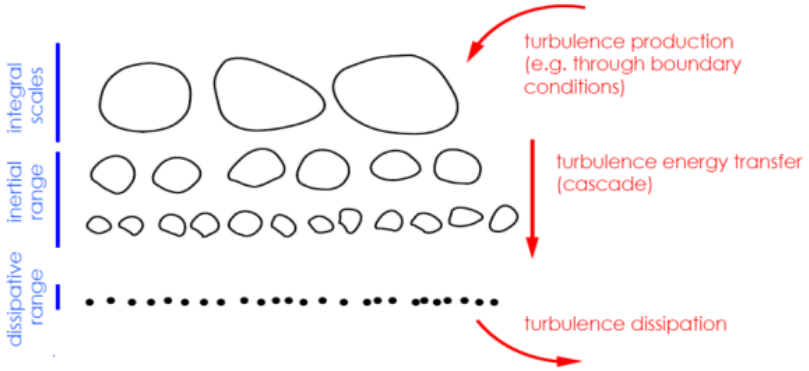

Figure 4.2: The theory of turbulence energy cascade, where the production of large eddies transfer to smaller scales and eventually dissipate into heat [10]

$$\delta_U = \frac{U_\infty - U}{U_\infty} \tag{4.1}$$

$$TI = \frac{\sigma_U}{U_\infty} \tag{4.2}$$

$$\Phi_z = \rho \iint_A U_x U_z dA \tag{4.3}$$

Driven by large-scale turbulence, the wake can move in addition to the downstream direction (horizontal), also in lateral- and vertical direction. This dynamic behavior of the wake is called wake meandering. Studies have shown that the wake meandering movement can be related to low-frequency activities around a Strouhal number of 0.3 and it effectively reduces the turbulence intensity levels and velocity deficit of measurement equipment. This effect is taken into account in state-of-the-art wake models by interpreting the meandering as a passive tracer, leaving the fluid dynamics unchanged [35].

Critical wake drivers

One of the key factors that influence the turbulent mixing in the wake region is the atmospheric stability of the ABL. The ABL is accumulated by the surface layer (up until 100m) and the Ekman layer (100-2000m), just below the free atmospheric layer. From this point, the influence of the ground is no longer felt by the flow, the pressure gradient and the Coriolis force are balanced out and the wind flows parallel to constant lines of pressure, isobars. The atmospheric stability is found from the shape of the potential temperature profile with height. Potential temperature is defined as the temperature a parcel would have if it is brought to the standard pressure in adiabatic conditions [36]. If the line is vertical, the atmosphere is considered neutral and a deviation from this line causes either stable or unstable conditions, if the derivative is positive or negative, respectively. The effect of atmospheric stability can be explained by focusing on a single air

parcel. If the air parcel moves upwards in a stable environment, the forces counteract the movement and the parcel is pushed back down. This can have significant influence on the turbulent mixing in the wake, as the vortices have a harder time to move than in unstable conditions, where, on the contrary, they are given an added support. Neglecting stability effects may cause changes in the wind shear and turbulence intensity profile against height, resulting in incorrect estimates of the wind speed, the turbulence and the energy output of the wind turbine.

Another important factor for wake losses is turbine spacing. The further the distance from the rotor, the more the wake flow is recovered from the presence of the wind turbine. Not only the distance, but the angle is also of influence. The yawing motion of the turbine can lead to a slight steer of the wake, eventually reducing the impact on downwind turbines. These are therefore also consulted as wake recovery techniques, starting already from the design phase of wind farms. Many hours of simulations of the optimal turbine-layout configuration are performed, using several wake models. These and other approaches for enhancing wake recovery will be explained in further detail in Chapter 5.

The presence of a wind turbine affects not only the flow behind the rotor, but the upwind flow, in front of the rotor, as well. This region of lower velocity, the induction zone, is caused by the same principle of flow blockage. As the fluid needs to go around the structure, it costs less energy to move in a smooth path. Similar to the concept of path of least resistance, the flow feels the presence of the turbine already further upstream and starts to move out of the way of the obstruction. The induction zone start at approximately two rotor diameters, where velocity losses up to 25% can be found at the center of the rotor [37].

Understanding the wake behind a single wind turbine is one thing, but the wake in a find farm is even more complicated. Here multiple wakes are overlapping each other, causing additional complex three-dimensional flow interactions. Usually these effects are modeled using superposition principles, where individual wake effects are cumulated according conservation of momentum or energy. The most common techniques are linear [38] and root sum square [39], respectively shown in Eq. 4.4 (a) and (b). Here the difference lies in the influence of the individual velocity deficit on the total. As shown in Eq. 4.5, the incoming velocity at the rotor can either be defined initial to the wind farm, referred as global (I), or to the local turbine (II). Another important aspect of wake modeling is the partial wake overlap. As wind turbines are sometimes not placed directly behind each other, the rotor may be only in a part of the wake of the upwind turbine. Therefore, often a simple correction is made, based on the percentage of wake overlap to the frontal rotor area. However, recent studies have shown that these superposition methods are not proven to come from physical laws and should be interpreted as empirical relations. Bastankhah et al. have developed an innovative solution to deal with this issue, by integrating over the entire wind farm to solve the equations [40].

$$\underset{\text{(a)}}{\Delta U = \textstyle\sum_{i=1}^{n} \Delta U_i} \qquad \underset{\text{(b)}}{\Delta U = \sqrt{\textstyle\sum_{i=1}^{n} \Delta U_i^2}} \tag{4.4}$$

$$\underset{\text{(I)}}{\Delta U_i = U_\infty - U_i} \qquad \underset{\text{(II)}}{\Delta U_i = U_{\infty,local} - U_i} \tag{4.5}$$

5

Wake recovery

After the air flows through the wind turbine rotor it reaches a drained state, as it loses energy to the blades. In this drained state, the wake, the large-scale turbulent structures, like the ones that are produced by the instabilities of the mixing layer, entrain and introduce a mean-flow kinetic energy flux from the undisturbed free-stream flow to the depleted wake. This process of re-energizing the wake flow occurs mostly in the far wake, starting from approximately three turbine diameters (3D) behind the rotor, shortly after the transition region from the near wake. In the near wake, the flow has just passed the rotor and starts to adjust to the new energy state. Initially, the flow structures are relatively organized, propagating smoothly downstream. Here, one can obtain a region of velocity deficit as large as the rotor diameter with a swirling motion counteracting the blade rotation. The flow across the shear layer of the wake is predominated by the intermittent tip-vortex structures, acting as a shield to the ambient flow. These vortices result in a net-zero flux of mean kinetic energy, opposing the recovery of the wake. Breaking down these tip vortices is therefore one of the options to improve wake recovery, effectively speeding up the transition to the far wake and accelerating the instabilities in the fluid.

Wind farm locations are becoming more scarce and wind farms must become more efficient to compete with fossil fuels in the energy sector. In addition to improving individual wind turbines and the optimization of the wind farm layout, wake losses and wake recovery has been one of the biggest topics in the wind energy research. Over the last decades, engineers have been fighting against these so called wake effects, hoping to improve the overall efficiency of the wind farm. Countless solutions have been developed over the years and they can be divided into three categories: passive, active and external solutions.

Passive strategies

Starting off with the passive strategies, these are modifications to the design to enhance wake flow recovery without the need for operational energy input or external devices. As wind turbine blades have an aerodynamic shape, a lot of research on aircrafts can be used in the wind energy sector as well [41]. Here passive flow control solutions can be found for the blade design, like vortex generators and vortilons creating strong vortices to stabilize the flow over the airfoil and creating additional trailing vortices that propagate downstream, similar to the effect of wings at high angles of attack (α). Other solutions are slotted and multi-element airfoils to create more lift at high α and delay stall; flow vanes to induce downwash at the TE; and protuberances at the LE to create 3D vortex flow; TE modifications, like TE serrations to increase the turbulence; slots to reduce the pressure difference and tip modifications to breakdown the tip vortices. In addition to adaptions to the blade design, also other passive solutions have been studied in the research field, of which a diffuser is the most common. This diffuser augmentation creates additional fluid interaction with the free-stream flow. They come in many forms, but the most efficient is the conical-shaped lens with a brim and shroud, as shown in Figure 5.1a . The design has a conical-shape to increase the area at the end of the diffuser, effectively expanding the stream-tube. As can be explained by the actuator disc theory and mass conservation, an increased area creates a lower pressure at the exhaust in comparison to the inlet of the diffuser. This pressure difference accelerates the flow through the rotor, creating an increase in perceived velocity by the blades. The inlet shroud creates a smooth entrance to the diffuser, making it easier for the air to flow trough the rotor. At the end of the diffuser, a broad flange is placed, the brim, to create separation vortices. These vortices create a low pressure region behind the diffuser, adding to the suction of the flow trough the rotor as well as enhancing the turbulence mixing of the wake [4].

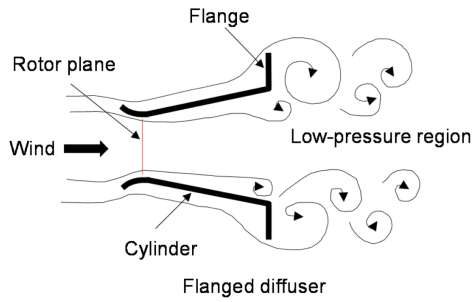

(a) Schematic representation of a diffuser-shroud design [4]

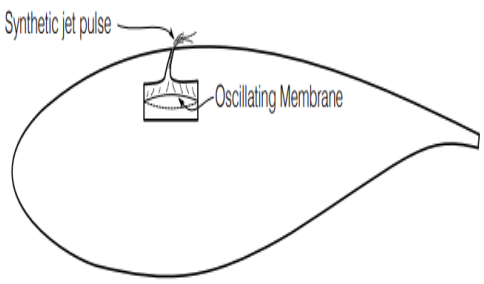

(b) Section view of a synthetic jet mechanism with oscillating membrane [41]

(c) Top view yaw misalignment techniques, in negative orientation [6]

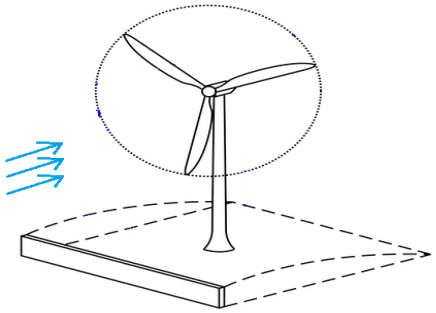

(d) Schematic representation of windbreaks, adapted from [42]

Figure 5.1: Overview of different active- and passive control strategies for wake recovery

Active strategies

Regarding the active control strategies of wake recovery, there are again many overflowing developments on the blade design coming from the aerospace industry [41]. For example, there are flaps, either in rigid form as in ailerons or flexible, to be used on both the LE and the TE. They create a slight change in the aerodynamic profile of the blade, as they vary the camber of the airfoil and hence the lift coefficient. In wind turbine applications, they are mostly used to regulate the power of the turbine or for load alleviation, a strategy to improve the turbine's performance by reducing the loads on the blade. In addition, there exist designs of deformable or inflatable membrane, acting as stall ribs. As the name suggests, these are used to induce stall in a controlled manner. By strategically placing these membranes, usually near the LE, they disrupt the flow early on, causing an early flow separation. Furthermore, there are spoiler devices to create additional disturbances in the flow leading to large instabilities, such as reversed flow and separation bubbles behind the spoiler. Other flow control strategies are boundary layer suction and blowing, effectively either by removing air or adding momentum to the boundary layer to improve blade performance, respectively. The last set of blade modifications for active flow control are the actuators. Here, the most researched approach is the Zero Mass Flux actuator (ZMG), an advanced implementation of a combination of boundary layer suction- and blowing. They manipulate the flow around the airfoil by inducing oscillations, causing a net zero mass flux over time. The most common type is the synthetic jet actuator, a piezoelectric oscillating membrane that creates pulses of air (Figure 5.1b). As the diaphragm moves, it ejects a burst of air into the flow, consisting of layered vortex rings, followed by a suction phase where the surrounding air is drawn in the actuator cavity space. Another actuator device is the plasma actuator. In simple terms, it creates an electric field between two electrodes and an insulator by applying a high voltage. The dielectric layer, the insulator, causes the generation of plasma from discharge. Plasma is a region of ionized air that is electrically conductive. The collision of plasma ions and air molecules creates induced flow close to the wall surface. It adds momentum to the boundary layer flow and causes additional formation of instabilities in the flow that are propagated downstream.

Besides all the progress on the rotor blades for active wake control, there are several other techniques to dynamically decrease the wake effects of the wind farm. One way to control the wake behind a wind turbine is to change the individual turbine power production of the upstream wind turbines, to reduce the velocity deficit, enhancing wake recovery and speed up the flow for the downstream turbines. By intentionally running a turbine sub-optimally, more energy can be extracted further on in the farm to achieve a net-positive outcome. These strategies are aimed to decrease the strength of the wake by modifying the induction factor upstream are called axial induction control (AIC) techniques. The turbine power production can be regulated by pitch-, torque- or cone angle control. In literature research there is quite a disagreement on the actual efficiency improvement of these control strategies, but almost all list the cone angle control as ineffective, as it leads to an net-negative power production of the wind farm [43]. Recently, the scientific community has developed a new line of AIC, which dynamically vary over time. These dynamic induction control (DIC) techniques use dynamic blade pitching to induce an early start of the natural mixing process. Currently, two discrete approaches can be found in research: the pulse- and helix design. The difference lies in the actuation of the blades. For the pulse design, the blade pitch of the entire rotor is varied with a sinusoidal function, creating a pulse of turbulent wind flow [5]. In contrast, by individually varying the blade pitch angle of the rotor blade with sinusoidal functions and phase differences, a more helicoidal wind flow can be generated. Simulations of both methods have shown positive effects of the wake recovery, increasing a two-turbine wind farm power production of up to 5 and 15%, respectively [44].

The other series of concepts are related to changing the direction of the wake: wake steering. Approaching the problem in two-dimensional form, looking at the front of the rotor, the wake behind the rotor can be steered in two directions. One way is to redirect the wake in the vertical direction, upwards towards the canopy above the wind farm. Note that only positive angles are possible, otherwise the rotor would collide with the tower. This strategy is based on controlling the tilt angle of the rotor. However, as many existing turbines have no integrated control system to actively control this angle, it has not been studied excessively. By contrast, an already widely used method is yaw control or yaw misalignment. Again looking at the rotor plane from the front, yaw angle control effectively steers the wake in the lateral direction, so either to the left or the ride side of the plane (Figure 5.1c). Here, a particular relation has been discovered between the direction of yaw misalignment and location on the globe. It has been found that counter-rotating yaw misalignment (positive yaw angle) in the northern hemisphere has a positive impact on the annual energy production, wherein a clockwise yaw rotation, on the contrary, causes a cutback. LES studies of this phenomenon retraced the cause back to the turbine rotation itself and the Coriolis effect [6]. Also a combination of the two, a hybrid of tilt- and yaw angle control, has been researched in the wind energy sector, where significant improvements in the power production can be found of 4% [45].

External techniques

In parallel to the large number of innovations related to the design of the wind turbine, the blades, the rotor or the tower, there are also external systems to improve wake recovery. Rather than focusing on the flow up and around an individual turbine, these external techniques manipulate the flow in a wider context. They are aimed to disrupt the flow before and after the wind turbine, in order to enhance the turbulent mixing process and hence add assistance to faster dissipation of the undesirable region of velocity deficit, the wake. Without a doubt, the most widely used technique in any wind farm to tackle the wake effects is wind turbine alignment optimization [46]. Highly depending on the site-specific environment, regarding the wind characteristics and the terrain conditions, it involves optimal placement of wind turbines within a farm. It should be noted that in addition to the ambient conditions, there are often also a high number of constraints involved. Here, there can be considered restrictions such as navigational shipping lines, protected marine life, bird migration, maintenance constraints and wind farm boundary limitation [47]. This optimization has been widely researched in the field of wind energy and a range of commercial software has already come out to solve this computationally, of which the WAsP application is the most popular [48]. WAsP is an advanced software bundle, developed by DTU Wind, that predicts optimal energy yield based on the models of the terrain, the wind turbine, the wake, the stability and the wind climate.

One way to intervene with the wind flow around a wind turbine is by adding obstacles or structures upstream. Two distinct types of innovations can be found in literature: wind barriers and windbreaks. The barriers are designed to break up large-scale structures in the flow and to induce controlled turbulence downwind. They particularly depend on the porosity of the material and its height with respect to the rotor swept area and have direct affect on the wind speed and the turbulence production [49]. As it blocks the undisturbed flow direction, it reduces the wind speed in most cases due to drag forces. However, in specific configurations of the barrier, where it is mounted to the ground, the height is significantly lower than the turbine and stretches out multiple rotor diameters to the sides, the barrier can add additional speedup of the flow into the rotor, amplifying the power production of the turbine (Figure 5.1d). These upstream bumps, with ranging material porosity and potentially of vegetable origin, are called windbreaks and have been proven to increase the performance of the wind farm [42]. It is also possible to position the obstructor in such a way that it is only partially in the rotor's path. This enables the flow to be deflected, which is especially useful for vertical axis wind turbines (VAWT). As they have their rotational axis in the vertical direction, unlike the more common horizontal turbine types which have the axis in the same direction as the wind flow, VAWT have blade rotation against the wind direction. By blocking the wind in this returning phase, the rotor loses less energy and can reach a higher efficiency [43], [50].

Along the same lines are all the developments regarding terrain modification. From preliminary research on wind turbine wakes in complex terrains, it has been found that the landscape is of significant influence on the annual energy production of a wind farm, as it affects the wind velocity profile with height and increases the mean-flow turbulent kinetic energy flux [51]. Despite the fact that most studies focus on the optimal power production in an existing convoluted domain, it is not a daft thought to turn this around. As these flow effects on ground-level can be of positive impact to the flow characteristics at turbine-level, such as the phenomenon of wind speed-up over hills, why not create artificial roughness elements to enhance the power production of a wind farm [52]. Onshore, there are numerous opportunities for these field adjustments, like adding slopes, ridges or mounds. These can be placed randomly in the domain or in specific order, creating a patterned surface on the ground. Here, also natural forms of terrain roughness can be used, such as vegetation or crop placement. The main purpose of this modification is to optimize the airflow close to the ground by disruption and to increase turbulence mixing in the wake. Similarly, man-made disturbances of the sea water, like wave generators, can be used to shorten the wake by increasing the turbulence mixing in counter-acting configuration of the wind- and wave direction [53].

Wake recovery is essentially about retrieving enough energy back in the flow for the downstream turbine to generate power. This principle is referred as wake re-energisation and usually involves either direct injection or entrainment from the outer flow, where the presence of the wind turbine is not felt by the fluid. Existing techniques to directly add energy to the flow are jet injection, large fans and heat sources. The latter also creates local thermal gradients that create convective currents in the flow, adding to the turbulence mixing process. Other external devices usually operate according to the theory of vertical entrainment, the entanglement of one substance by another. Bringing it back to the context of wind turbine wakes, it involves the suction or steering of the yet energetic flow outside of the wake. This may be via heat transfer from heat sources or reflective material, as well as via the downwash in aerodynamic lift devices. Which can be achieved for example by placing a small turbine or an elevated airfoil to create artificial turbulence to the flow and enhance wake mixing. However, these options require a large foundation to attain turbine boundary layer height, where it is most effective. Let this be the very principle of one of the most recent developments in the wind energy sector: airborne wind energy (AWE), a tether-supported aerodynamic device to create lift.

6

Kite theory

One of the upcoming research topics in the wind energy sector, airborne wind turbine (AWT), is an innovated concept of the standard wind turbine. In these designs, an aerodynamic lifting device, supported to the ground with a tether is used to generate electric energy from the wind. In this way, there is no foundation needed and substantial material can be reduced. Horizontal-axis wind turbines tend to produce the largest amount of energy at the tip of the blades due to the higher relative wind speed. AWT systems can be used to operate in these particular locations for optimal power extraction. In addition, they provide tremendous flexibility in their placement in three-dimensional space. This allows the operation to be adjusted to the optimum wind resources, both in height and spatial location. In the case that the environment changes, for example due to a new wind farm, they can be moved to a more efficient site due to its high mobility. However, this new generation of wind turbines also entails a number of challenges. As these systems have more degrees of freedom, sources of failure and also more severe consequences, the aerodynamic behavior of kites is far more complex than traditional wind turbines. To achieve full automated power conversion in the air, one has to make substantial advances on the material and especially kite's control system. With this new devices, the regulatory framework of the aviation needs to be adjusted so they could operate safely within the current airspace [54].

AWT systems fall under the airborne wind energy (AWE) sector, as they directly use or generate wind energy using aerodynamic or aerostatic lift devices at high altitudes. These consist of both powered concepts, such as helicopters and airships, as well as unpowered mechanisms like balloons, kites, kytoons and gliders. These concepts can be characterized by either heavier-than-air or lighter-than-air. The first category are the aerodynamic systems that rely on the wind to support the device, due to aerodynamic forces like lift and drag. In contrast, the second set depends on the buoyancy force to keep the aerostatic devices in the air. As the name suggests, a kytoons (blend of kite and balloon) falls right in between, creating both aerodynamic and aerostatic lift.

Kites have a long and varied history before it was implemented to produce electricity. While the exact origin remains unsolved, one has found first signs of kite use in Polynesia on cave paintings, estimated around 5000 BC. They used kites for fishing purposes as well as for religious reasons, like offering wishing to the gods for fertility or harvest [55]. As the word spread across the world by Asian traders, the application of kites extended towards cultural and military purposes. They were employed to signal troops, measure distances or to scare the enemy away. It did not take long before the scientists, too, started to explore with this innovation. Primarily in the meteorology sector it has made a lot of impact, where measurements could be taken at previously unreachable heights, later used by Benjamin Franklin to prove that lightning is electricity. Also in engineering, they started experimenting with kites, particularly to move humans, both on the ground as in the air. The latter is the founding father of the aviation as we know it today, as the Wright brothers used the concept of box-kites to create the world's first successful airplane, the *Wright Flyer* [56]. Later in the 20th century, a pioneer van Gries saw the possibility of kites to lift onboard wind turbines to higher altitudes [57]. Based on his work, Loyd published his paper in 1980 on crosswind kite power extraction, which is considered as the foundation of kite theory [58].

AWE system designs

The AWE continues to rise in size and can certainly be considered as a full new branch in the wind energy sector. As the outlook of higher power densities, defined as energy extraction per square meter (W/m^2), is very promising, a lot of developments are currently being made. Think of material compounds, flex-wings, autonomous control systems and above all scaling [59]. Scaling-up the kite sizes has been the biggest issue over the past years, due to the square-cube law [60]. A larger kite surface area can theoretically extract more energy, but the faster-growing added mass requires thicker tethers, stronger materials and more complex control systems. Currently, experiments are being conducted of both horizontal and vertical AWE farms, to even further optimize earth's ground surface area [61]. Despite the high financial entry-level for AWE research, the first commercial systems start to occur.

While new concepts of AWE implementation are still appearing in the field, a clear distinction can be made based on the location of power generation. In ground-gen systems, the power generation occurs at the ground by flying the kite at high-altitudes in a pre-defined pattern. This trajectory is commonly either a circle or a figure-of-eight. As the wind causes the creation of aerodynamic forces on the kite, the kite starts to ascend in the sky. The tether-connected kite pulls on a rotating drum on the ground, which is converted into electricity with a generator. At some point, the kite reaches its maximum tether length and needs to be reeled back in to restart the power generation phase. During this retraction phase the kite is de-powered to minimize energy use and create a net-positive power cycle, often referred as the pumping cycle. There is, however, a subtype of these ground-gen techniques that does not involve a cyclic operation. These systems are characterized by their rotational behavior. Multiple aerodynamic devices are connected with each other under high tension, supported by a lifter kite, causes the entire structure to rotate. This spinning motion creates a torque and is converted into electricity by a generator on the ground. The other type of AWE systems, the fly-gen, has an onboard power generation. A small wind turbine with generator produces electricity in the air. This energy is channeled via a conducting tether to the ground, where it is stored for later use or directly transferred to the grid. An overview of the different principles is given in Figure 6.1.

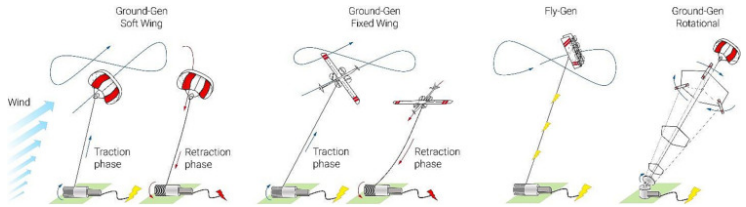

Figure 6.1: Overview of ground- and fly-gen AWE operational principles (adapted from [59])

Kite designs have a large range of shapes and sizes, both in fixed-wing or a soft-wing concepts, with varying pros and cons. The rigid devices, usually made of carbon fiber-reinforced polymers are based on airplane knowledge and are often similarly shaped to gliders. They offer high lift-to-drag ratios, are more stiff and reliable. Due to the additional support required by the heavy onboard power generation, fixed wings are therefore favored in fly-gen systems. However, these structures are heavier and need aerodynamic systems to control its direction. On the contrary, the soft-wing kites are made from flexible membranes, allowing for less mass and easier steer-ability. Here you can imagine kite flying on the beach, were the kite is controlled by actuation of specific bridle lines. As a result, this type is superior during take-off and landing maneuvers. Although there is more research currently taking place on soft-wing systems, a winning shape has not yet emerged and both technologies are still under development [62].

Kite aerodynamics

An aerodynamic device creates lift due to a pressure difference between the upper and the lower side [63]. This causes a circulation effect on the flow field of the surrounding wind. For a 2D wing with infinite span, this circulation causes an equal flow movement upwards before and downwards behind the wing. As seen in the top frame of Figure 6.2, this flow behavior can also be retraced in the 3D wing. However, as the 3D wing has a finite span, the flow has another way of passing the blockage. At the tip of the wing, the flow can simply move around the edges instead of going over. This principle of tip vortex creates an additional

downward velocity component throughout the whole wing. As indicated by the second frame of Figure 6.2, this component affects even the free-stream flow in front of the wing. Summing these two together shows the velocity field around the 3D wing with finite span. This leads to an overall negative velocity component of the flow behind the airfoil, the downwash. In the vicinity of the airfoil, this downwash leads to a slightly rotated local relative wind speed. This can be interpreted as if the airfoil is being tilted, creating an additional angle with the free-stream velocity. This angle, the induced angle of attack, decreases the effective angle of attack perceived by the wing (Eq. 6.1). From basic aerodynamic principles, it is known that the drag force is parallel to the relative wind vector and the lift force is perpendicular. Due to a shift in this vector, the local lift vector is now inclined backwards. As the lift vector has a component in the direction of free-stream velocity, it effectively creates a drag force. Due to the presence of downwash, the lift force creates an additional drag component: the lift-induced drag. From potential flow theory, the velocity induced by a single semi-infinite straight vortex filament can be retrieved from the Biot-Savart law (Eq. 6.2). This relation shows the effect of a single point of circulation to any other point in space. In the work of Prandtl, it was found that the strength of this vortex filament (Γ) is related to the local lift force from the Kutta-Joukowski theorem (Eq. 6.3). From this, the lift-induced drag contribution can be obtained in non-dimensionalised form, as seen in Eq. 6.4

$$\alpha_{\text{eff}} = \alpha_0 - \alpha_i \tag{6.1}$$

$$q_i = \frac{\Gamma}{4\pi h} \tag{6.2}$$

$$L' = \rho V_R \Gamma \tag{6.3}$$

$$C_{d,i} = \frac{C_L^2}{\pi e AR} \tag{6.4}$$

$$AR = \frac{b^2}{S} \tag{6.5}$$

Where the key parameters of influence can be achieved. Not surprisingly, the lift force is from ultimate significance, even accounting for a quadratic involvement. The second parameter, e, is the span efficiency factor. Depending on the spanwise lift distribution this value ranges from 0 to 1, with 1 being the most optimal. This particular value can be found for elliptical lift distributions, where both downwash and induced angle of attack are constant along the span. This distribution yields for the minimum drag penalty due to lift and is therefore of high interest to the industry. Another important aspect of the lift-induced drag appears to be the wing aspect ratio (AR). This geometric property, defined by the span and the surface area of the wing, is shown in Eq. 6.5. The inversely proportional relation with the induced drag shows that for drag reduction, wings with high aspect ratios are preferred. Unfortunately this parameter is also important for other aerodynamic performance characteristics, like structural stability. As this is critical for kites, it is uncommon to find a very slender wing in this field and it is rather optimized with other parameters. For very high values of the aspect ratio, the effect on the lift curve decreases and it shows similar behavior of an infinite wing [63].

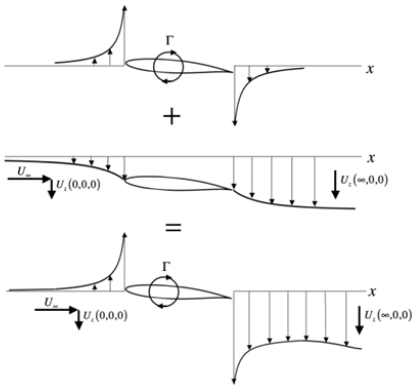

Figure 6.2: Velocity field around a 3D lifting wing of finite wing span, at the aerodynamic center [64]

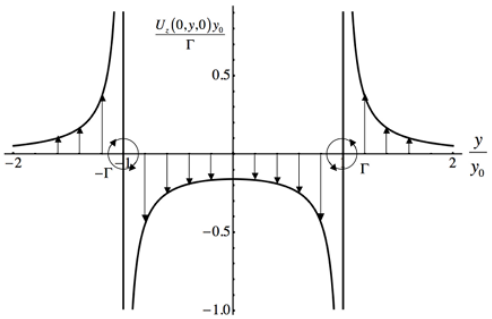

Figure 6.3: Induced downwash by two parallel infinite vortex lines of opposite sign, viewed from the vortex wake [64]

The direct relation between the aspect ratio and the induced downwash can be explained using two parallel infinite vortex lines. Looking at Figure 6.3, these vortices create large vertical velocity components at the vicinity of the lines. Moving away from these lines, its impact tends to diminish. Going back to an airfoil, these vortex lines represent the tip vortices at the end of the wing. The larger the distance between these lines, the smaller the effect is at the center. Therefore, a very wide wing, with high aspect ratio, approximates the flow behavior of an infinite wing. The effect on the lift coefficient is visualized in Figure 6.4.

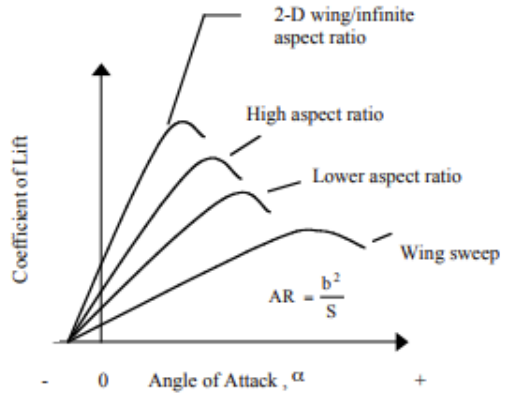

Figure 6.4: Lift curve slope for different wing aspect ratios [64]

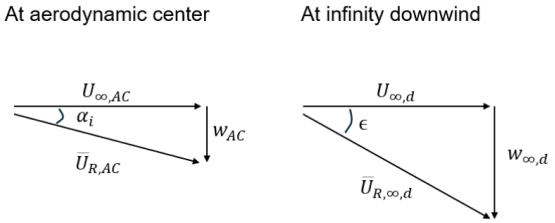

Figure 6.5: Definition of induced angle of attack (α_i) and total downwash angle (ϵ)

It should be noted that multiple definitions are used in the literature regarding the angles due to downwash. For clarity, a clear distinction is made, based on downwash location, as shown in Figure 6.5 The total downwash angle (ϵ) is defined as the angle between the free-stream velocity and the downwash at infinite downwind. Assuming small angles, this relation is found in Eq. 6.6. Conversely, the induced angle of attack is defined with the downwash velocity at the wing's aerodynamic center. Therefore these angles are not equal to each other. As the wing is hypothetically located in the center of infinity- upwind and downwind, they correlate with a factor of two (Eq. 6.7).

$$\epsilon = \frac{w_{\infty,d}}{U_{\infty,d}} \tag{6.6}$$

$$\epsilon = 2\alpha_i \tag{6.7}$$

3D Kite theory

The basic working principle of kites can be simplified by assuming the kite and tether to be massless and all forces to be concentrated in a single point *K*. By removing mass from the equation, the tether can be assumed straight and there is a geometric similarity between the kite's kinematic- and force triangles. In real-case scenario, the gravitational forces on the kite will counteract the lift force and reduce the overall tension in the tether. Additionally, due to the tether's own weight, the line will start to sag to better deal with the loads. As shown in Figure 6.6, the kinematics of the kite is defined by the wind velocity (v_w) and the kite velocity (v_k). Summing these vectors together, according to Eq. 6.8, is the wind velocity that is felt by the kite, the apparent wind velocity (v_a). At this velocity, the aerodynamic forces, lift (L) and drag (D), act on the kite and create an aerodynamic resultant force (F_a). As the apparent wind velocity does not have to be aligned with the chord line, two relative angles can be defined: the angle of attack (α) and the sideslip angle (θ_s). For simplification, the effect of the sideslip angle is neglected.

$$\vec{v_a} = \vec{v_w} - \vec{v_k} \tag{6.8}$$

$$L = 1/2\rho C_L S(v_a)^2 \tag{6.9}$$

$$D = 1/2\rho C_D S(v_a)^2 \tag{6.10}$$

$$F_a = \vec{L} + \vec{D} = 1/2\rho C_R S(v_a)^2 \tag{6.11}$$

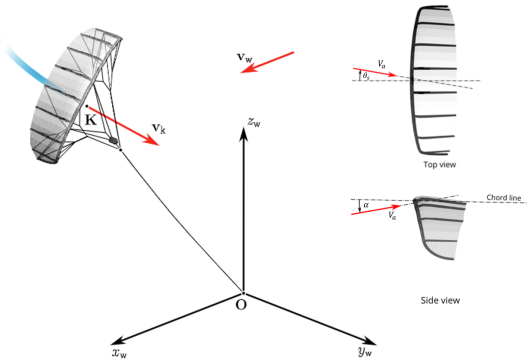

Figure 6.6: Schematic representation of the kite's kinematics and relative angles, adapted from [54]

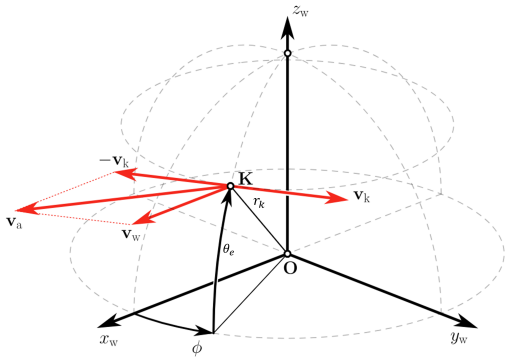

Figure 6.7: Schematic representation of tethered flight in 3D space, adapted from [54]

As kites fly in three-dimensional space, it is easier to define its position in spherical coordinates. At every point in time, the kite's location can be described by three parameters: the radial distance from the attachment point of the tether (r_k), the azimuthal angle (ϕ_k) and the elevation angle (θ_e). To better show these parameters, a three-dimensional representation is shown in Figure 6.7. Here, the ideal crosswind theory of Loyd [58] can be applied in the $e_{r_k} - v_a$ plane to establish the aerodynamic resultant force in a more general form:

$$\frac{F_a}{q_{w_\infty} S} = C_L \sqrt{1 + \frac{1}{E^2}} (1 + E^2)(cos\theta_e \, cos\phi_k - f_r)^2 \tag{6.12}$$

Where f_r is defined as the ratio between the radial kite velocity and the wind velocity (reeling factor) and E as the ratio between the aerodynamic lift- and drag coefficients (C_L/C_D). The force is non-dimensionalised with the dynamic wind pressure (q_{w_∞}) and the kite's surface area (S_k).

Kites for wake recovery

Besides the bright future of AWE systems for power production, by effectively mimicking the behavior of HAWT blade tips, kites can also be used to improve the energy-efficiency of wind farms [9]. Due to their high relative wind speed and dynamic movement pattern, they create highly turbulent flow, with large vortical structures. Here, active mixing takes place between the region of velocity deficit and the outer-layer. This principle of vertical entrainment can be used to enhance the turbulent mixing between two wind turbines and speed up the wake recovery. As kites are mobile and can reach high altitudes, their three-dimensional positioning can be optimized to interact with wake flow in real-time. The focus for this study, therefore, is not on the kite's power generation, but rather on the aerodynamic behavior of these devices in three-dimensional steady flight.

7

Modeling techniques

Over the past decades, the wind energy sector has expanded rapidly. More, larger and better wind farms have been placed recently, trying to produce the much-wanted green energy. The biggest culprit, next to space allocation, has been the wake effects within the farm. As previously explained in Chapter 4, this is due to increased turbulence and reduced velocity region of the upwind wind turbine. Accurately modeling this behavior is therefore crucial for designing wind farms, both for life cycle and energy yield. The research on this topic has not rested because of this and the number of published papers is still increasing exponentially [65]. With this, the speed and accuracy of wake modeling has increased and a wide range of software tools has been developed. While most of the recent progress on wake models has been on adaptations and modifications on specific fields, like offshore- and floating wind energy, generally they can be classified into four methods: experiments, analytical or semi-empirical, numerical and data-driven. Figure 7.1 shows a generic overview of the recent developments, followed by a short description of the four categories.

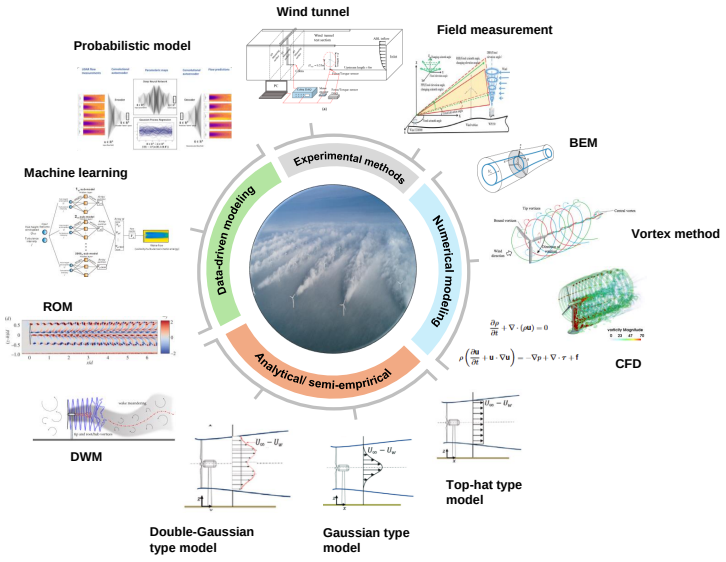

Figure 7.1: Overview of numerous methods for wind turbine wake modeling, adapted from [65]

Experimental methods

The most evident method to model the behavior of wind turbine flow is to use real-time experiments. Whether these are wind tunnel studies or even in-field measurements, they provide an accurate representation of the flow interaction of the real scenario. Hereby, similarity principles on the geometry, flow and dynamics are used to simulate the aerodynamic behavior of the wind turbine in operation. Generally speaking, many experiments can be conducted at wind tunnels. It allows for a controlled environment and is cost-effective for the early design phases. However, they are limited by size of the facility. In some occasions, the scaling of the relevant parameters is too difficult to produce a reasonable setup in the wind tunnel. Here, wind field measurements can be the solution. These concern specific experiments of the wind turbine at full-scale and require advanced instruments. As they are very time-consuming and extremely expensive, this option is often applied only as a last resort. It should be noted that these field measurements are different from operational data from existing wind farms. They are purpose-driven, conducted in a controlled manner to address a specific issue of research. In contrast, operational data contains important information of existing wind farms during regular functioning, like power output, wind speed and turbulence. This data is more accessible and therefore often used as reference material in comparative studies.

Analytical wake models

Wake formation is a very complex phenomenon of non-linear and viscous flow interactions. However, it can be simplified to a simple negative jet by assuming a top-hat shape of the wake-velocity deficit. One of the groundbreaking figures, N.O. Jensen [66], used this simplification to find a linear relation between the incoming wind speed (U_∞) and the distance downwind to the turbine (x), as seen in Eq. 7.1. From Figure 7.2 it can be obtained that the model assumes an uniform velocity distribution with linear wake expansion. His theory was based on one-dimensional conservation of mass, the stream-tube. During the study he found that the thrust coefficient (C_T), the expansion rate (k_w) and the turbine diameter ($\varnothing_T$) were of influence to the velocity deficit. The model was validated with wind measurements and it was concluded that the wind profile showed more of an Gaussian profile than a top-hat. Based on his work, Larsen improved the wake model by allowing for additional radial dependency of the velocity deficit [67].

$$\frac{U_\infty - U_w}{U_\infty} = \frac{1 - \sqrt{1 - C_T}}{(1 + \frac{2\kappa_w x}{\varnothing_T})^2} \tag{7.1}$$

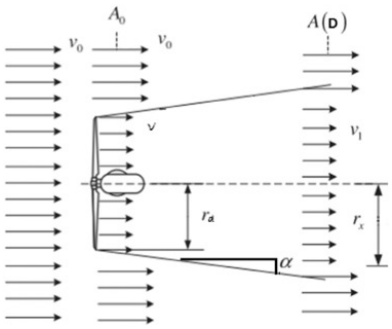

Figure 7.2: Top-hat type wake model of Jensen for a single turbine, based on 1D conservation of mass [66]

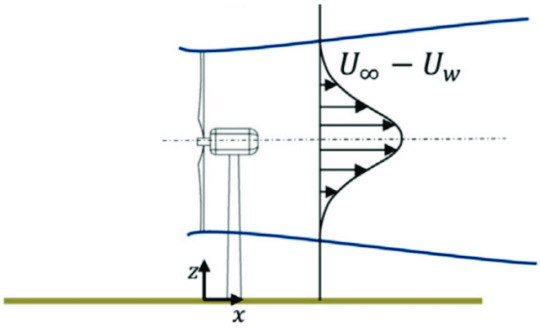

Figure 7.3: Gaussian type wake model of Bastankhah, adapted from [68]

In contrast to Jensen, which used a control volume downwind of the rotor, Frandsen et al. [69] improved the expression by considering the flow in front of the turbine as well. Next to mass conservation, also the conservation of momentum was applied, but they still assumed an incorrect top-hat shape of the velocity deficit. This was later refined by Bastankhah and Porté-Agel (BP) [68], where they assumed a Gaussian velocity distribution to solve the mass and momentum equation. Their research showed to better predict the wake effects, especially in the near wake region. Despite explicit vertical and spanwise coordinates in the equation, the BP model is effectively symmetric around the central-axis of the rotor. However, due to the effects of atmospheric stability and ground surface interaction, this is surrealistic. This affect of wind shear is added to the Gaussian wake model by Xie and Archer [70]. Further innovations are based on these models and enhance the accuracy based on other aspects of wake modeling, such as meandering (DWM), yawing, wake-added turbulence and ABL interaction [71].

Data-driven models

With the fast increasing involvement of artificial intelligence (AI) technologies, it is the most recent line of developments for wake modeling [72]. Data-driven systems originate from the earliest forms of reduced-order models (ROM). These aimed to increase the accuracy of lower-order models, by using high-fidelity data integration in the models' weak spots. With the development of probabilistic machine learning algorithms, a more accurate representation of the flow behavior around the wind turbine can be simulated. Research states that it combines the power of numerical- and empirical models, providing high-fidelity approximations at lower computational costs. However, it requires substantial data training and complex statistical analysis. Currently it is still in its infancy and further research is necessary.

Numerical methods

Numerical modeling the fluid interaction of wind turbine wakes can be conducted via three approaches: BEM, vortex methods and CFD. The blade element momentum theory (BEM) is the most simple, assuming simplified flow behavior and blade independency. The model is fast, but cannot be used for dynamic wake prediction. Vortex methods are based on the interaction of bound vortices, produced by circulation due to lift and shed vortices in the wake. The vortex filaments, as described in Section 8.2, can either be prescribed or move freely. In frozen vortex methods, the location of the filaments is described by the rotor speed, the radial distance and the wake convection rate. In contrast, free vortex wake methods (FW-VM) accounts for wake deformation, self-induction of wake velocity and induced velocity by the blade's circulation. The last set contains all forms of computational fluid dynamics (CFD), that solves the three laws of conservation: mass, momentum and energy. These equations, better known as the Navier-Stokes (NS) equations, can be solved for all scales of turbulent vortex structures using DNS. However, as this requires substantial computational costs, it is often preferred to model some of the scales. In LES models, only the large-scale eddies are resolved and the small scales are modeled using a sub-grid scale (SGS) model. As most of the energy transport occurs at the large scales, LES is accurate but cheaper. However, it still requires extensive computational power and it could be advantageous to simplify the numerical problem even further. Decomposing the NS-equations into a mean and fluctuating component, Reynolds has found a simplified way to solve the time-averaged equations of motion. Due to nonlinearity of the NS-equations, averaging all terms lead to a new unknown term: Reynolds stress. This turbulence closure problem is solved by modeling this additional stress term in the equation. The RANS method is therefore the least expensive, but unable to capture complex flow phenomena.

The effects of the wind turbine on the flow is modeled by discretisation of the blades. These represent the forces on the blade, like as lift and drag, that disturb the free-stream wind flow. The geometry of the blades can be fully-resolved, but since this requires large computational resources, it is cheaper to use discretisation methods. In most simple terms, the rotor can be assumed as a porous disk, exerting forces to the flow. This method can be used in combination with the BEM theory in CFD. Another way to model the blades is by representing the loads on a single line on the blade. This technique is used in both CFD, the actuator line method, and in lifting-line vortex methods. Further accuracy improvement can be done by dividing the blade geometry into surfaces, rather than line segments. These are also conducted in both CFD as vortex methods: actuator surface and vortex lattice method, respectively.

Model selection

In the context of this research, the model needs to represent the dynamic flow interaction between wind turbines and kites. As this particular setup is still just a concept, no wind tunnel experiments or field measurements are available at the moment. The scarce data that is currently accessible contains only simulations and not yet validated. Data-driven and theoretical models based on empirical data can therefore be eliminated right away. Although the prospect of the efficiency-benefit is very promising, experimental methods are very expensive and the implementation will have to be further explored first for funding purposes. The sole remaining option of this study leaves numerical methods. In this regard, there will be a trade-off between key modeling characteristics, such as simulation speed, computational cost, complexity and accuracy. From comparative studies on wind turbine wake modeling, CFD modeling with LES seems the best option, since it is mainly governed by large-scale eddies [71]. This new technique for wake recovery enhancement is conducted in a LES study by Ploumakis, were positive effects were found for wind farm efficiency. However, as LES still requires substantial computational power, the parametric study on the kite remained open. Here, it was stated that the effect may be related to the downwash principle. Previously explained in Section 6.2, downwash is produced by vortex generation of aerodynamic lift devices. Accordingly, the turbine-kite interaction might be accurately modeled by vortex methods. This creates both comparison material for the LES study, as well as an extension on the parametric kite study due to accelerated simulations.

8

Vortex method

Vortex methods (VM) are seen as medium-fidelity models for modeling the wake effects in wind farms, with an acceptable accuracy and significant less computational cost in comparison with high-fidelity CFD models [73]. The vortex theory is based on the assumption of inviscid, incompressible and irrotational flow. Here, the continuity equation can be rewritten as the Laplace's equation and the potential flow theory can be used to solve for the motion of the fluid. The circulation due to lift generation of the blade is represented by vorticity of vortex elements. The evolution of the vortices is established using fundamentals of fluid mechanics, like the Biot-Savart law (Eq. 10.14), Helmholtz's theorem and the Kelvin-Stokes theory. In literature, a wide range of different vortex methods can be found, with varying levels of fidelity and efficiency. Often corrections have been made to better simulate specific dynamic flow interactions, like wake meandering, ground effect and wave interaction for floating offshore wind turbines. A rough overview of common vortex-based methods found in literature is presented in Figure 8.2. For this review study, a classification is made on four bases: blade discretisation, wake characterization, vortex structures and flow behavior. The four bases, as shown in Figure 8.1, will be briefly described below.

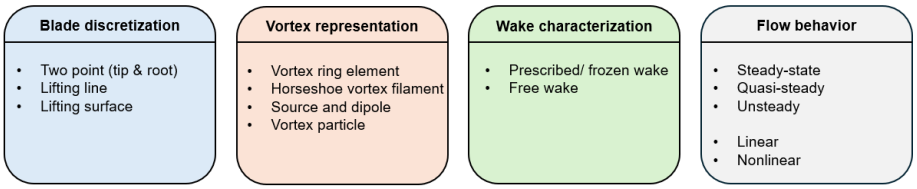

Figure 8.1: Classification of vortex-based methods based on four criteria: blade discretization, vortex representation, wake characteristics and flow behavior

Blade discretisation

To model the aerodynamic effects on the flow due to the loading, the blade needs to be discretized into elements. The most simple form is to represent the blade by two vortex points, one at the blade tip and one at the root. As the dominant vortex is at the tip, it is often used for simple estimates of wake effects. Here, the priority lies on computational speed, which can be useful for real-time modeling. To account for spanwise effects of the blade's lift, the blade can be discretized more accurately as a lifting line (LL). On this line, often the quarter-chord line, the aerodynamic forces are aggregated. In this theory of Prandtl, it is assumed that the total circulation on the blade can be divided into line segments, each contributing to a small share of the total lift. Modifications of the lifting line exist, to account for swept-, tapered wings and unsteady effects. However, the LL methods are unable to capture three-dimensional effects of the blade, due to the representation of the vortex element as a single line. To better account for the shape of the blade, blade Discretization methods of lifting surfaces can be used. By dividing the blade into a sheet of vortex lattices, the flow around the blade can be modeled more accurate. The lifting surfaces are assumed to be of infinitely thin and, therefore, cannot consider effects due to thickness effects. For these particular situations, the blade can be represented with both upper and lower surfaces in a panel method (PM). These techniques, of which the source-doublet is the most common, use the most advanced blade discretisation method, at the cost of higher computational time.

Vortex representation

Modeling the behavior of the vortex elements depends heavily on the manner in which vorticity is initiated and how it convects downstream with the flow. These modes are called vortex singularities and play a major role in wake simulation, by mimicking the rotational nature of the flow. The most basic representation is the vortex ring method (VRM), where the wake is described by discrete rings of constant circulation. In these methods, it is assumed that the effects of an helicoidal vortex structure can be replaced by rings at the middle of the circular projection [74]. While, the ring's center is always at the rotor axis, the radius is not consistent in all methods. Ranging from simple disc shapes, replacing the tip vortex, to complex time-varying doughnut shapes, simulating both tip- and vortices. Another relatively simple representation of the vortex system is with vortex filaments. These lines of arbitrary shape are subjected to the Helmholtz' theorem have constant circulation strength along its entire length. These filaments are generally placed in a horseshoe pattern, with a bound vortex connected to the blade's span and two trailing vortices that extend downstream. The trailing vortices are assumed to stretch to infinity, complying with Helmholtz. Basic horseshoe methods appear in single form, with trailing vortices shed at the blade's tip. However, this implies completely uniform circulation along the wingspan. For most cases this is impractical due to irregular lift distribution and multiple shoes are needed to produce realistic effects. More advanced methods also account for the temporal lift changes by adding shed vortex filaments between Lagrangian markers, creating a vortex sheet pattern [75]. In potential flow theory, a velocity potential can be described by linear superposition of elementary flow potentials. Therefore, the flow field can be represented as a sheet of sources and sinks. However, as these do not create any lift, a doublet distribution must be added to the blade. It is often used in combination with vortex filaments for wake modeling of complex aerodynamic devices, like propellors [76]. The most enhanced description of flow behavior are the viscous vortex particle methods (VPM). These high-fidelity models track the progression of individual vortex elements. The particles can move freely in a Lagrangian framework, offering incredible modeling accuracy at the cost of higher computational cost. In contrast to all other methods, the VPM does not assume potential flow. Potential flow methods heavily depend on empirical relations from experimental data, in order to account for complex turbulence phenomena, like viscous dissipation and vortex stretching [77]. Unlike filaments methods, the vortex structures, or vortilons in 3D, are not bound to their neighbors and can move independent from each other. The time-dependent movement can be established from the local velocity vector, where the velocity described the speed and the gradient the direction. The VPM directly simulates the flow field by solving the incompressible Navier-Stokes equations in the vorticity-velocity form. This Lagrangian approach to wake modeling can be used for 2D and 3D flows and is considered as a mesh-free alternative to conventional CFD methods.

Wake characterization

An essential component of wake vortex modeling is the characterization of the wake markers. The shape of the wake can be predefined (PW) to significantly reduce the computational costs of the model. The initiation of vorticity in the wake remains unaffected, but its evolution is determined by empirical functions of the unperturbed flow velocity and the induction speed. These relations are often assumed linear, similar to actuator disk momentum theory. The induced velocity by the loading on the blades and the wake self-induction is neglected. It can be seen as an accumulation of steady-state wakes, frozen in time [78]. Despite the computational efficiency, the model is greatly simplified and fails to capture complex wake phenomena, such as roll-up, instabilities and dynamic interaction. Conversely, free wake models (FW) allow for these time-dependent wake exchanges. The wake shape is not fixed and deforms over time due to local effects. The time-marching free-wake methods enable vortices to convect, spread and diffuse [79]. Taking into account the induction of wake structures (n) on other wake structures, increases the numerical order of magnitude of the problem to $\mathcal{O}(n^2)$, as well as making it sensitive to numerical instabilities.

Flow modeling

While specific combinations of the classification options, like the LL-FWVM or the steady-VRM, appear more often than others, almost all combinations possible can be found in literature. For potential flow methods, the basic theory is often based on either steady or quasi-steady flow of first-order. Depending on the context, this may not be representative and corrections must be implemented to account for unsteady or non-linear effects. Unsteady vortex-based methods (UVM) allow for flow changes in time, allowing them to model a more realistic scenario. According to research, the blade loading has low- and high frequency fluctuations, so it should be reflected in the vorticity as well. These oscillations of the flow circulation causes inconsistencies in unsteady methods, which requires an auxiliary condition to ensure smooth flow. The unsteady methods are often based on the Kutta condition for the closure problem of the wake vortex sheet, stating that the strength of the new shed vortex is equal to the bound vortex of the previous time-step [80]. Further corrections of the viscous wall effects use a relaxation on the Kutta condition in combination with the triple-deck boundary layer theory to better simulate boundary flow separation in highly unsteady conditions [81]. The nonlinear corrections, on the other hand, are rather less straightforward. Nonlinearity of wind turbine wake flow appear in many forms. Think of rotational augmentation, leading edge separation, wake meandering, dynamic stall, ground effect, wake diffusion and post-stall effects. As the list goes on and on, there is no standard best option either. From simple integration with the lift and drag polar, the so-called airfoil look-up table (LUT), obtained from high-fidelity CFD analysis, to empirical functions or complex viscous coupling to predict stall behavior [80]. In the earlier days, most vortex-based studies were build on the assumption of steady linear flow, but almost all modern research models do account for the time-dependency and have at least one correction for nonlinear or viscous effects. Here, the LUT is the most common due to its efficiency and practicality, with alteration on the lift- and drag coefficient, the angle of attack or the vortex strength.

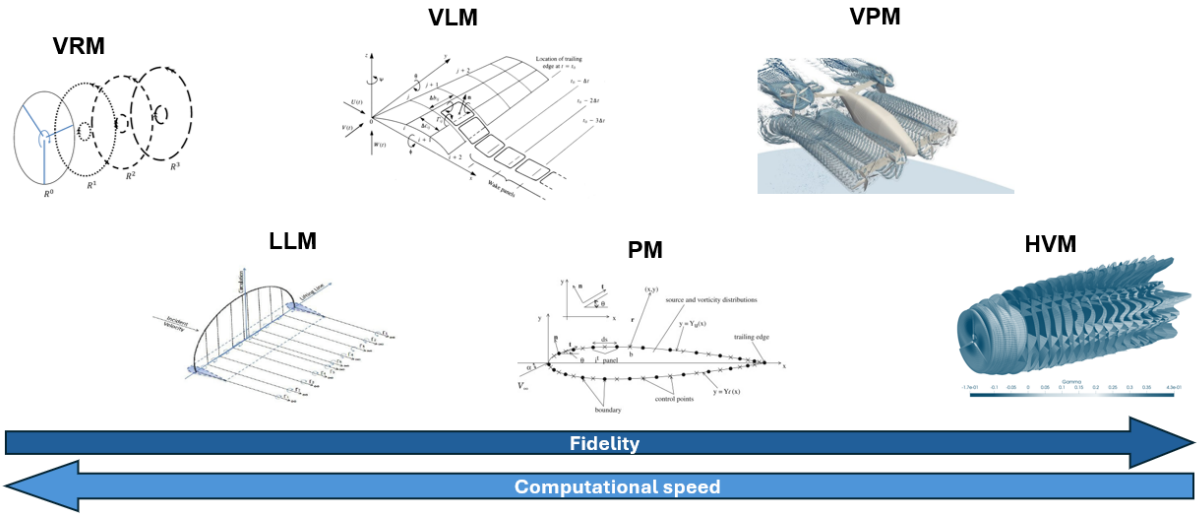

Figure 8.2: Overview of common vortex-based methods, showing the trade-off between fidelity and computational speed

Hybrid methods

Despite the many different options of vortex-based methods for wake modeling, there is not always an accurate model to be found in literature. As a result, researches have further expanded the world of vortex methods the last decade. Integrations between techniques can be found. Where the near wake is modeled with a high-fidelity option, while the far wake is modeled with less accuracy, like the VRM, in order to shift the focus of interest and increase the computational efficiency [74]. Additionally, there are hybrid vortex methods (HVM) that combine vortex-based power with other wake modeling methods, ranging from analytical- to CFD methods. Here, the shortcomings of, for example implementing boundary conditions in VPM, are addressed by the strength of grid-based techniques like LES [77]. On the spectrum of modeling fidelity of Figure 8.2, these are often found at the very ends, where computational speed naturally moves in opposite direction.

Applications to Turbine-Kite modeling

While all vortex methods are used for research studies on wind turbine wakes, to current date is the lifting line is still the most popular [82]. Turbine blades are often very slender, with simple airfoil shapes in the cross-section. Representing the blade loading at the quarter-chord line is, therefore, often very accurate yet fast option to consider. It is not surprising, in that respect, that existing vortex-based tools are based on this approach. The three largest applications, QBlade [83], OLAF [84] and CACTUS [85] all use an unsteady LL-FWVM in their model, with possibilities to consider nonlinearity. However, as wind turbines are become larger by the day, the blades become longer and thicker as well. Additionally, modeling modern-day wind turbines have additional complexity due to offshore wind shear and platform motion of floating turbines far at sea. The call for more accurate simulates grows louder by the day, extending the lifting line theory more often to lifting surfaces with UVLM [80]. Among many comparative studies is shown that these tools can be used to accurately model wake effects for both HAWT [86], [87] and VAWT [88], [89] in three-dimensional flow, from steady- to turbulent inflow conditions. As with all modeling techniques, increased accuracy means increased computational time. Vortex-based methods are, therefore, a considerable middle ground of both culprits, allowing for fast modeling of concept-phase type studies.

Airborne wind energy system, particularly fixed-wing kites, are much like wind turbine performance when it comes to wake-flow dynamics [90]. Hence, initial studies were often conducted using the same lifting line concept, yet soon became apparent that additional corrections were needed to account for the nonlinear effects [91]. These enhanced methods were often based on the vortex step method (VSM), in which stepwise adjustments were applied based on 2D aerodynamic polars to account for viscous stall effects at high angle of attack, as used in the special kite-version of OLAF: kiteFAST [92]. However, unlike wind turbines, kites are not fixed to the ground but to a tether; have a complex movement pattern; and, with the rise of flex-kites, are also irregular in shape. Ever more frequent, the lifting line is no longer representative and a 3D-VLM or a 3D-PM, as implemented in the APAME software [93], is used resorted instead. Only in special cases where very complex dynamic interactions need to be modeled, such as multi-rotor systems, VPM is used [94].

For the purpose of this research, which investigates the impact of kites on wake recovery, the model must be able to simulate multiple turbines and kites simultaneously, within a dynamically coupled environment. Existing tools, such as openFAST with both OLAF and kiteFAST integrated, provide strong frameworks for individual modeling of either devices. However, these tools cannot be used directly to represent a multi-turbine or turbine-kite system with accompanying wake interaction. Dedicated tools for a wind farm setup often resort to an analytical-based model, such as the DWM in fastFARM [95]. This simplified method assumes quasi-steady flow and cannot be used to model the complex 3D unsteady flow effects of the kite interaction. Furthermore, current implementations often rely on simplified wake descriptions that limit their ability to capture unsteady wake dynamics and effects due to viscosity. These restrictions motivate the development of a new simulation tool that extends the current vortex-based models. This advanced model provides a more representative framework for studying kite-induced wake recovery.

9

Previous work

Kite deployment for enhancing wind turbine wake recovery is a new concept, aiming to increase turbulent mixing via vertical entrainment of the outer flow. Over the past few decades, several studies have examined the potential kite-induced effects on the wake flow, ranging from conceptual design to advanced computational methods. Early studies mainly focused on theoretical models and simple designs, providing initial estimates of the potential efficiency improvements. Later studies have further evolved the concept, using high-fidelity CFD simulations, which allows for a more accurate representation of the complex three-dimensional flow interactions between the turbine and the kite. This chapter provides an overview of previous contributions, highlighting their findings and limitations.

DSE group (2011)

At the Delft university of technology in 2011, a group of 10 students from the faculty of aerospace engineering performed their design synthesis on the development of an external device to improve the efficiency of the Offshore Windpark Egmond aan Zee (OWEZ) wind farm [8]. The objective of their study was to reduce energy losses by at least 3%, by mixing the wake of a wind turbine with the undisturbed flow above the wind farm. During the conceptual phase of the design, they came up with diverse ideas on how to theoretically solve the problem at hand. The options were based on half a dozen of principles: suction, downwash, gravitational convection, thermal convection, vortex generation, and obstruction. Based on the requirement of low cost and low energy needed, they have chosen to focus on the principle of downwash. Downwash is defined as the change in direction of air in the production of lift in aerodynamic devices [96]. Multiple concepts came to light, from rotating cylinders to kytoons, a mishmash of a heavier-than-air kite and a lighter-than-air balloon. With an extensive trade-off, they came to the conclusion of using kites in their final design to enhance the mixing of the wind turbine wake: *the Deaolus kite*, see Figure 9.1.

Figure 9.1: The Deaolus kite system, a conceptual design of using kites to enhance flow recovery of wind turbine wakes [8]

The calculations of their innovative design were solely based on theory. Although they applied considerable questionable simplifications of the aerodynamic behavior of the wake flow in the presence of the kite, they found a substantial improvement in the efficiency of the wind farm of 4.3%. The main limitation to this efficiency refinement was the kite dimension, as they put a constraint on the maximum projected kite span to be out of the way of the rotor disk when the kite is in the retracted position. Despite this restriction, the increase in practical performance was found to be around 6%, after considering several correction factors to account for wind direction, power rating, and mixing efficiency. For wind farm developers, this order of efficiency improvement is significant and it is therefore of high interest to the field of wind energy to further research this disruptive design of vertical entrainment of the wake behind wind turbines. In addition, they established an outline of the key factors that affect the efficiency increase with the kite and made a first draft of a parametric study on the kite area. It was found that, among others, the rated wind speed, the current wind farm efficiency, the wind direction, the rotor diameter, the turbine height and the turbine spacing were influencing the results.

Ploumakis (2015)

This research done by the DSE study group is the precursor of further follow-up studies regarding the use of kites to improve the wake recovery behind a wind turbine. In 2015, a master student at the TU Delft, Ploumakis, is the first to continue on this work [9]. He retraced the design steps and ran a deeper analysis on the kites' influence on the wake flow. Here he discovered a slight misjudgment of the kite's facing, which caused the wind farm efficiency to be overestimated by the DSE group and had to be dialed back to 2%. In contrast to using analytical calculations of the wind turbine wake by the DSE group, Ploumakis used a high-fidelity model to simulate the wake flow. To fully describe the dynamic behavior of the fluid, one has to solve the Navier-Stokes equations 9.2. These are partial differential equations to mathematically express the mass and momentum equation of homogeneous, isotropic, incompressible Newtonian fluids , based on the continuity equation (9.1) and Newton's second law motion.

$$\nabla \cdot \vec{V} = 0 \tag{9.1}$$

$$\underbrace{\rho}_{\text{Fluid density}} \left[\underbrace{\frac{\partial \vec{V}}{\partial t}}_{\text{Change of velocity with time}} + \underbrace{(\vec{V} \cdot \nabla)\vec{V}}_{\text{Speed and direction of fluid}} \right] = \underbrace{-\nabla p}_{\text{Pressure gradient}} + \underbrace{\rho \vec{f}}_{\text{External forces}} + \underbrace{\mu \nabla^2 \vec{V}}_{\text{Viscous forces}} \tag{9.2}$$

To approximate the solution to the Navier-Stokes equation, Ploumakis used the large eddy simulation (LES). Here, only the large scaled motion of the fluid is resolved and the smaller scales are modeled using a sub-grid-scale model (SGS). As the computational cost is proportional to Re^3, it was preferred to use LES over solving the equations without any modeling, as used in direct numerical simulation (DNS). Since the motion of the fluid in the wake is mainly governed by large vortical structures, LES is better at approximating the flow than a lower-fidelity model such as RANS, despite its significantly lower computational cost. With RANS, the fluid motion is averaged out in time, making the unsteady behavior of the fluid harder to model. In addition, LES is expected to be more close to the predicted energy range of interest.

The new projection of wind farm efficiency improvement of 2% is considerably close to the uncertainty of numerical simulation. Here, errors can occur during the physical modeling of the Navier-Stokes equation (simplification, boundary conditions, geometry), in the discretisation method (spatial, temporal), as well as in the programming (iteration, convergence, computer round-off) [97]. Therefore, next to the qualitative study on the mean flow statistics after the implementation of kites in the array of wind turbines, he tried to optimize the kite characteristics.

Ploumakis started off with the setup of the numerical wind flow in the ABL, where a neutral stability and incompressible flow was assumed. This simplified the fluid motion, as thermal effects and compressibility effects can be neglected in the turbulence mixing process. These two assumptions were validated with literature, as the research was focused on high turbulent, quasi-steady, isothermal flow for low mach numbers ($Ma < 0.3$). With his setup, he managed to simulate the behavior similar to the logarithmic law approximation of velocity with height after ten flow passes trough the domain. The average turbulence

intensity at domain height was found to be 12% and this setup was used as the basis for further simulations. In his simulation, he found that the LES model was not able to capture correct flow behavior near the wall. This phenomenon of excessive mean velocity gradients near the wall is a common problem in LES models of the ABL, as the fluid motion is here dominated by smaller turbulence scales. This discrepancy can be approximated with a wall-model, but a better solution was found in literature in the work of Mason and Thompsen [98], by introducing a back-scatter model to transfer energy from the unresolved SGS scales to the larger resolved scales. However, since Ploumakis used the software of Ansys Fluent in his LES modeling, he was unable to use this type of model and is therefore not considered in the simulation.

The next step in his research was to fill the computational domain with wind turbines. Where he started with only two wind turbines, he soon discovered the wake to be under-developed in this configuration and extended the wind farm to four turbines with a turbine spacing of six turbine diameters (6D). To simulate the wake of the wind turbine, the actuator disc model was used. Two versions of this model were compared and it was concluded that the ADM model with both axial and tangential induction (ADM-R) was a better approximation to the validation case in comparison with the non-rotating option (ADM-NR), due to the consideration of added swirl effects. This added swirl results in rotational kinetic energy losses, which are representing the rotational motion of the wind turbine blades [99]. Assuming sub-optimal power production of all four turbines at an induction factor of $a = 0.17$ and a thrust coefficient of $C_T = 0.56$, the four-turbine wind farm efficiency was found to be 54.7%. This number is used as a base case for the comparative study of the kite implementation.

In the study of the kite's influence, four cases were conducted: validation with the DSE study, the effect of kite surface area, the impact of turbine loading and lastly, the consequence of higher kite power densities. The kite was assumed to be a fixed flat elliptical wing with a constant angle of attack of 10° along the wing span. It was modeled as a discontinuous pressure jump, spread out over an infinitely thin surface, as a function of the free-stream velocity. During all cases, the domain size, number of turbines, turbine spacing, AD model and pressure jump of $39Pa$ were kept constant. The first case found a significantly lower efficiency in comparison with the DSE study. This was due to the previously explained kite facing, where the adverse effects of the aerodynamic drag were neglected, and the difference in initial conditions regarding the kite surface area and the turbine loading. In the parametric study of the kite surface area, the velocity deficit was found to increase with the surface area, as anticipated. However, an unexpected reduction of the turbulence intensity in the downstream direction was established. This strange behavior was found inconclusive to the turbulence mixing, as the mixing is primarily in the out-of-plane motion of the flow. Therefore, a new parameter was evaluated to better characterize the mixing, the mean kinetic energy flux. The simulation showed a substantial increase, indicating the prediction of faster wake recovery, resulting in an array efficiency 62.9% for the largest kite. The third study on turbine loading, effectively changing the thrust coefficient of the turbine, resulted in a larger velocity deficit behind the first wind turbine. The wind turbines further downstream showed less affected and the impact of the kite seems to be less effective in this full-load operation. With the higher turbine loading came higher values of turbulence intensity in the x-direction, but the kinetic energy flux was virtually identical to the partial load case. As the formula for array efficiency was based on the power production of the first turbine, the array efficiency was lower in the full-load case. A last parametric study on the kite power density showed a clear correlation with the efficiency. The wake recovery at hub height with respect to the base case was notably higher for larger densities. As the turbulence intensity is a function of the forcing, the TI_x was found lower due to the strong vertical velocity component from the kite's wake. The simulated wake flow dynamic behavior is found to be very similar to the turbulence characteristics of uniform tree canopies [100]. Which is not a surprising discovery, as it was already obtained in literature that the canopy behavior is dominated by large scale eddies. The inflection point, where the peak of shear production of turbulence kinetic energy can be found, was found to lie on the same level as the canopy studies at approximately 3/4 canopy height.

Kokkedee (2022)

In the research of Ploumakis, a LES model is used to simulate the wake effects of the kite. Since LES models require substantial computational cost, the number of simulations was limited. Therefore, his study only contained a small parametric study of the kite size and made recommendations for other key factors, like location downstream of the turbine, kite height and rotor performance, for future work. This was the starting point of the following research on this system by Kokkedee [10], where he used a simpler model, RANS, to model the wake flow to significantly speed up the amount of simulations that could be conducted. The wind turbine was modeled similarly with an actuator disc model, but not accounting for rotational flow (ADM-NR) and the kite was modeled following the principle of actuator line (AL). Although RANS has been proven to approximate the dynamic behavior of the wake-flow more poorly, it has been chosen to reduce the computational cost in order to validate and extend the parametric study of Ploumakis. In the validation study of Kokkedee to compare his simulation with the work of Ploumakis, significant differences were obtained and were further away from measurement results from the literature. Therefore, the results of Kokkedee are solely used as a qualitative study for the kite parameters. The parametric study of the kite consisted of six cases: surface area, height, downwind location, angle of attack, number of kites and inflow velocity. Similar to the work of Ploumakis, a positive effect was found of increasing the kite surface area. The kite height was found to reach an optimum location of 130m for a wind turbine hub height of 80m, where an even higher value showed better wake recovery of downstream wind turbines. The location of the kite was of high influence, were the biggest improvement was found by placing the kite as close to the rotor as possible. The angle of attack showed a linear relation with the velocity deficit reduction, somewhat expected from the relation of angle of attack and downwash lift production of the kite, causing the velocity downwards and the flow entrainment from the outer layer of the ABL. However, since the drag force is not a linear relation with the angle of attack, the efficiency tends to reach an optimum around 18°, which is considered relatively large and raises questions of the wake model. In the application of a single kite between all turbines, it was found that the largest power increase was at the last wind turbine. Here, also the biggest improvement of the velocity deficit was found. This despite the maximum point of the turbulence kinetic energy, the better characteristic to describe the turbulence mixing, was found to be behind the second wind turbine. This might come from the wake effect of the kite upstream on the downstream kite, but the velocity deficit is relative small in comparison to the wind turbine. However, in the study of Ploumakis this is not accounted for, as he assumes a constant pressure jump for each kite. This assumption is unsubstantiated and needs to be explored further in a follow-up study.

Part III

Methodology

10

Methodology

For this research, a new aerodynamic tool was developed to simulate kite-turbine wake interactions: K-TWIST (**K**ite-**T**urbine **W**ake **I**nteraction **S**imulation **T**ool). The model combines classical lifting-line theory with a nonlinear free wake vortex method, based on the AWSM code by van Garrel [101]. The vorticity field is described by a system of discrete wake vortex filaments, where the temporal evolution is handled with a time-marching method. The effects due to viscosity are captured using the viscous-splitting algorithm, which separates inviscid convection of the Lagrangian marker and the viscous diffusion [102]. The K-TWIST model is written in Python code, using the Numba just-in-time compiler to perform the computation in parallel to reduce runtime [103]. All simulations are performed on the HPC12, a cluster of high-performance computing nodes at the Delft University of Technology [104]. The resulting velocity field is subjected to azimuthal and annular averaging in data post-processing, to reduce un-physical oscillations and extract representative metrics, such as the axial velocity deficit (δ_U) and vertical momentum flux (Φ_z).

This chapter describes the methodology of the K-TWIST model, structured in three main sections. In Section 10.1 the theoretical framework will be presented, including the fundamental principles like vortex theory, lifting-line and the Biot-Savart law. Subsequently, Section 10.2 described how these theories have been translated into numerical Python code. Here, the most important numerical techniques, such as the viscous-splitting algorithm, time integration scheme and parallel computing, will be explained. In addition, this section present all coordinate transformations used, the system of bound- and wake vortices, as well as the model's input variables. To conclude this chapter, Section 10.3 shows the post-processing techniques that are applied on the raw simulation data.

10.1. Theoretical framework

The K-TWIST framework is built on fundamentals such as classical vortex and potential flow. Unlike traditional methods that directly solve the Navier-Stokes equations, the fluid dynamics are described by the temporal evolution of vorticity in the flow. This method approaches the flow field from a different angle and can reduce complexity through dimension reduction via lumped forms of sheets or lines. The potential flow theory provides the background for linear superposition, while the viscous effects near the vortex cores are accounted for through core models and core growth methods.

10.1.1. Vorticity equation

Vortex-based methods are used to describe the dynamic motion of a fluid element, by solving the vorticity transport equation instead of the Navier-Stokes equation. In order to understand the fundamental aerodynamic principles of free wake vortex theory, some basic knowledge on fluid dynamics is needed.

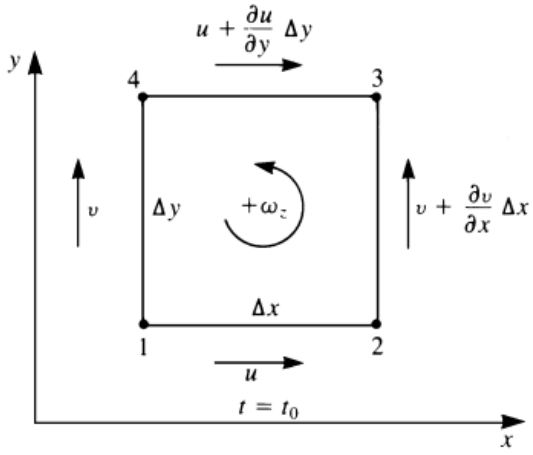

Figure 10.1: Angular velocity of infinitesimal rectangular element [105]

The erratic motion of a fluid element, like an infinitely small rectangular element of Figure 10.1, can be described by a translation, rotation and deformation. For a simple translation in the z-plane, the edges of the element may experience different velocities, which causes a deformation and rotation. Since the angular velocity is defined as the relative velocity divided by the radius, the z-component of the fluid element (ω_z) can be established from the average of the contributions in each direction. For convenience, the vorticity is defined as twice the angular velocity. As seen in Eq. 10.2, the vorticity is basically the curl of the velocity field ($\vec{q}$) and describes the local fluid rotation.

$$\vec{\omega} = \frac{1}{2}\nabla \times \vec{q} \tag{10.1}$$

$$\vec{\zeta} \equiv 2\vec{\omega} = \nabla \times \vec{q} \tag{10.2}$$

Circulation is defined as the line integral of the velocity field around a closed contour. Using the theory of Kelvin-Stokes: ”The line integral of a vector field over a loop is equal to the surface integral of its curl over the enclosed surface”, circulation can be related to vorticity. This link is presented in Eq. 10.3, where $\vec{n}$ symbolizes the normal vector to the surface S. From Gauss' divergence theorem, the surface integral of a vector field over a closed surface is equal to the volume integral of the enclosed volume V. For any incompressible, inviscid flow with conservative body forces, the circulation around a closed fluid path remains constant in time. This conservation of circulation, known as Kelvin's circulation theorem, supports the concept of shed vortex generation. When circulation is suddenly introduced on a lifting surface, there must exist an equal, counter-rotating vortex in the wake. In vortex theory, this phenomena, known as the starting vortex, preserves total circulation in the system.

$$\Gamma = \oint_C \vec{q} \cdot d\vec{l} = \iint_S \vec{\zeta} \cdot \vec{n}\, d\vec{S} \tag{10.3}$$

$$= \iiint_V \nabla \cdot \vec{\zeta}\, d\vec{V} \tag{10.4}$$

$$\frac{D\Gamma}{Dt} = 0 \tag{10.5}$$

To describe the fluid dynamics with vorticity, the variation of the vorticity in time must be described. This can be established from the incompressible Navier-Stokes equation governing fluid motion, as seen in Eq. 9.2. Taking the curl of the equation and using vector calculus identities, results in the vorticity transport equation of Eq. 10.6. It describes the rate of change of the vorticity and can be simplified further to Eq. 10.7, in the absence of non-conservative (rotational) forces.

$$\frac{D\vec{\zeta}}{Dt} = \frac{\partial\vec{\zeta}}{\partial t} + (\vec{q}\cdot\nabla)\vec{\zeta} = (\vec{\zeta}\cdot\nabla)\vec{q} + \nabla\times\vec{f} + \nu\nabla^2\vec{\zeta} \tag{10.6}$$

$$\frac{D\vec{\zeta}}{Dt} = \frac{\partial\vec{\zeta}}{\partial t} + \underbrace{(\vec{q}\cdot\nabla)\vec{\zeta}}_{convection} = \underbrace{(\vec{\zeta}\cdot\nabla)\vec{q}}_{strain} + \underbrace{\nu\nabla^2\vec{\zeta}}_{diffusion} \tag{10.7}$$

10.1.2. Potential flow theory

Potential flow theory is based on the assumption of irrotational flow. As seen in Figure 10.2, the rotation of the flow describes the change in orientation of the fluid element's movement inside a flow field. Since the rotation of the element is the result of the shear force of adjacent elements, irrotational flow often occurs in high Reynolds number or inviscid flows.

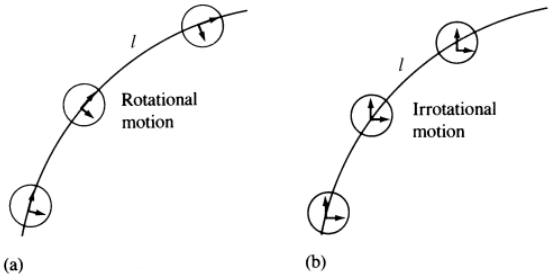

Figure 10.2: Rotational- (a) and irrotational (b) motion of a fluid element [105]

In potential or irrotational flow, both the vorticity vector field and the circulation are therefore equal to zero (Eq. 10.8). From vector calculus, any zero-curl vector field can be described as the gradient of a scalar, since the curl of a gradient is always zero. This scalar function (Φ) is called the velocity potential (Eq. 10.9).

$$\vec{\zeta} = \nabla\times\vec{q} = 0 \tag{10.8}$$

$$\vec{q} = \nabla\Phi \tag{10.9}$$

$$\nabla^2\Phi = 0 \tag{10.10}$$

Using the definition of velocity potential in the incompressible continuity equation of Eq. 9.1, it can be reduced to a linear differential equation: the Laplace's equation (Eq. 10.10). Therefore, a velocity potential can be created by linear superposition of elementary flow solutions, such as uniform-, source-, sink- and vortex flow. It is somewhat counterintuitive to note that a vortex flow is a potential flow, as it does create circulation. However, all rotation is created at the vortex core and everywhere else the flow is irrotational.

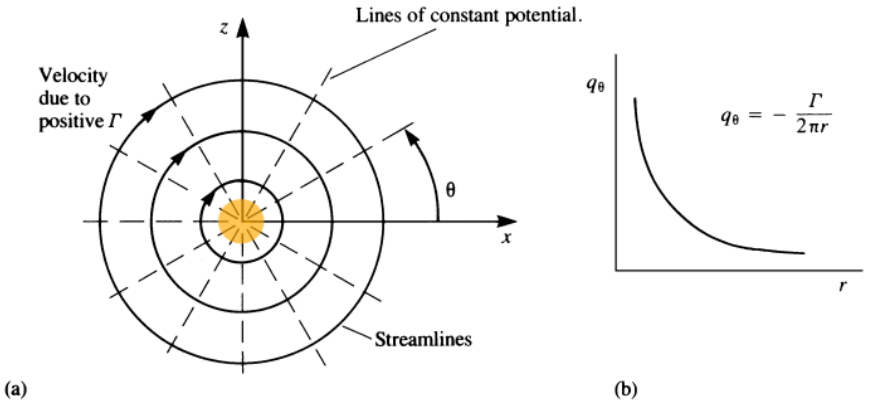

Figure 10.3: (a) Two-dimensional *free* vortex flow. (b) Tangential induced velocity components as a function of the radius, adapted from [105]

The vortex flow of Figure 10.3, is referred as *free* vortex flow, due to the absence of external forcing to create the rotation. The equipotential lines are independent of the radius and the induced velocity by the 2D vortex only has a tangential component. As seen in in Figure 10.3b, it is inversely proportional to the radius. This creates nonphysically large induced velocities for small values of r and an singularity at the center point ($r = 0$). At these smaller scales, viscous forces become relevant and the assumption of inviscid flow does not hold. Therefore, it is often preferred to treat this region, the viscous core (indicated in orange), differently from free vortex flow. The most simple solution to remove the singularity is to use a cut-off radius, but more common is to use viscous core models to better mimic ”real” vortex flow behavior. One approach is to interpret the viscous core as a solid body, rotating in a viscous fluid at a constant angular velocity. This fluid behavior is often found in externally forced flow, like a blender, and is therefore referred as *forced* vortex flow. The tangential component of the induced velocity is a simple linear function of the radius and the angular velocity. This combination of vortex flow with a forced core is called a Rankine vortex. Other methods exists as well, based on the Kaufmann vortex or even account for the viscous diffusion in time, like the Lamb-Oseen model.

10.1.3. Vortex filament

Similar to the definitions of streamlines being tangential to the local velocity vector, the lines parallel to the vorticity vector in the flow field are called vortex lines (Figure 10.4). When multiple vortex lines pass trough a closed curve in space, it forms a vortex tube. If the cross-sectional area of the tube becomes infinitely small, it is defined as a vortex filament.

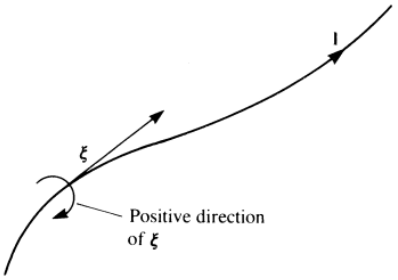

Figure 10.4: Vortex line [105]

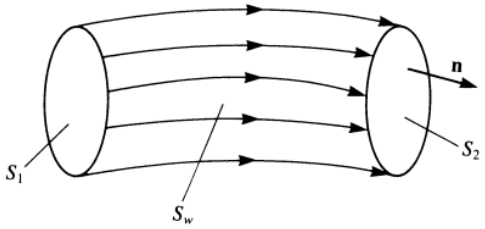

Figure 10.5: Vortex tube [105]

As visualized in Figure 10.5, the volume inside the vortex tube is enclosed by two base surfaces and one lateral surface. As the lateral surface is parallel to the vortex lines, it does not contribute to the circulation. Only the outside caps of the tube have non-zero circulation. Since the normal vector ($\vec{n}$) is the outward normal and their sum must be equal to zero, according to Eq. 10.4, the circulation on any cross-sectional

surface of the tube is equal. Based on these results, Hermann von Helmholtz developed his theorem on inviscid incompressible vortex filament flow, fundamental to lifting-line theory:

1. The strength of a vortex filament is constant along its length
2. A vortex filament cannot start nor end in a fluid, it must form a closed path or extend to infinity
3. A fluid element that is initially irrotational remains irrotational

One of the fundamental theories of vector calculus notes that any well-behaved vector field can be decomposed into a divergence-free (solenoidal) and an curl-free (gradient) field. Applying this Helmholtz decomposition to a velocity field results in Eq. 10.11, where Φ is a scalar potential and Ψ a vector potential. Taking the curl of the full equation to obtain the vorticity, results in Eq. 10.12. Here, the contribution of the scalar function to the vorticity vanishes due to the definition of irrotational flow, as described in Section 10.1.2. The formulation of vorticity reduces to the vector potential Poisson's equation, which can be solved using Green's theorem to establish a solution to the partial differential equation (Eq. 10.13). Here the vector potential is evaluated at an arbitrary point in space with a distance of $\vec{r}$ to a vortex element.

$$\vec{q} = \nabla \times \Psi + \nabla\Phi \tag{10.11}$$

$$\vec{\zeta} = \nabla \times (\nabla \times \Psi) = -\nabla^2\Psi \tag{10.12}$$

$$\Psi = \frac{1}{4\pi} \iiint_V \frac{\vec{\zeta}}{|\vec{r}|} d\vec{V} \tag{10.13}$$

When the velocity field can be expressed solely by the vorticity field, the vortex induced velocity can be obtained from the curl of the solution to the vector potential. In lifting-line theory, the contribution of external potential flow is handled separately, trough the bound circulation on the blade. Taking the curl of Eq. 10.13 and using the relation of vorticity to circulation, it results in the Biot-Savart law. This function, as in Eq. 10.14, allows for calculation of the velocity induced by a vortex segment at any point in space.

$$\vec{q_i} = \frac{\Gamma}{4\pi} \int \frac{dl \times \vec{r}}{r^3} \tag{10.14}$$

$$q_{\theta_{12}} = \frac{\Gamma}{4\pi d} \left(cos\gamma_1 - cos\gamma_2\right) \tag{10.15}$$

The Biot-Savart law can be further simplified under the assumption of a straight vortex segment. For reasonably small discretisation of the vortex line, the straight-line segment does not require additional correction for self-induced velocity due to the curvature effects [106]. It is comparable to the trapezoidal rule, of the second-order accuracy. With this, the integral of Eq. 10.14 can be removed and the induced-velocity is purely tangential. The result is a function of its strength (Γ) and the angles between the evaluation point ant the two end points of the vortex segment, as seen in Eq. 10.15. For a semi-infinite vortex line that starts at the origin, this relation reduces to that of Eq. 6.2. The direction of the velocity is normal to the spanned plane by the vortex line segment and the point, which is purely in the tangential direction for a straight vortex segment.

10.1.4. Viscous-splitting algorithm

In most practical problems, the phenomena due to viscosity occur on much smaller length scales in comparison to potential flow events. Therefore, vortex model use a Lagrangian approach to describe the flow with discrete vortex lines of concentrated vorticity: vortex filaments. In inviscid, irrotational conditions, the vortex lines behave like fluid material lines, where their motion is described by a simple convection of a Lagrangian marker (Eq. 10.16). In free wake vortex methods, these markers are found at the end points of the vortex filament.

The principle of separate treatment of the inviscid convection and viscous diffusion of the vortex filament is known as the viscous-splitting algorithm. While the inviscid methods often give good approximations to the flow, it is more accurate to account for these effects due to viscosity. This includes a definition of

the vorticity field within the vortex filament core, instead of purely mathematical techniques like cut-offs to simply avoid the singularity of the Biot-Savart law, as well as a representation for the actual viscous diffusion of the filaments. The independent convection of the two end points of the filament via Lagrangian marker partly accounts for the strain term of the vorticity equation (Eq. 10.7), but there are some coupled effects that are often overlooked.

In free-vortex wake methods, the vorticity field within the vortex filament is either neglected or described by viscous core models. These algebraic methods approximate the tangential component of the induced-velocity, the swirl velocity, in the close vicinity of the vortex core. These radial profiles are a function of the non-dimensionalised radius and is either based on modeling key features of the core, or based on empirical data fitting. The radius from the vortex line is normalized by the viscous core radius. By definition, at this radial distance the swirl velocity is at a maximum.

To account for the viscous effects in time, the evolution of the viscous core radius must be considered. This principle is known as the core spreading or core growth method and is introduced by the Lamb-Oseen model. With the assumption that both the axial and radial components of the induced-velocity are zero, they were able to find an axisymmetric solution to the laminar, one-dimensional Navier-Stokes equation. The swirl velocity quickly decays from its peak and the vorticity is diffused in radial direction, as the core size expands with time. The viscous core radius can be expressed as a function of the kinematic viscosity and time, as presented in Eq. 10.17. In this context, time is represented in terms of vortex age (ξ_t), denoting the elapsed time since vortex initiation. The parameter a_{lo} is the Oseen constant, which comes from the differentiation of the swirl velocity with respect to the radius to obtain the point of maximum tangential velocity: the core radius.

$$\frac{d\vec{r}}{dt} = \vec{q}(\vec{r}, t) \qquad , \vec{r}(0) = \vec{r_0} \tag{10.16}$$

$$r_c(\xi_t) = \sqrt{4a_{lo}\,\nu\xi_t} \tag{10.17}$$

$$Re_v = \frac{\Gamma_v}{\nu} \tag{10.18}$$

$$\delta_v = 1 + a_{sq} Re_v \tag{10.19}$$

$$r_c(\xi_\phi) = \sqrt{r_{c_0}^2 + \frac{4a_{lo}\,\delta_v \nu\,\xi_\phi}{\Omega}} \tag{10.20}$$

Due to the laminar flow assumption of the Lamb-Oseen models, the core growth rate is underestimated in comparison with experimental data. It does account for molecular diffusion, but neglects other forms like turbulent diffusion due to large-scale eddies or due to vortex merging of neighboring elements. Therefore, Squire instigated a modified version of the model to account for the effects of self-generated turbulence. He added a viscosity diffusion parameter (δ_v), which is effectively an average of the background turbulence. In Squire's hypothesis, this average apparent parameter was a function of the non-dimensional vortex strength: the vortex Reynolds number of Eq. 10.18. Correlative studies with experimental observations confirmed this hypothesis, where an average value of $a_{sq} = \mathcal{O}(10^{-4})$ for rotating wings [107]. For large-scale rotors with orders of magnitude larger vortex Reynolds number, this would result in ($\delta_v \approx 100$). This implies that the viscous diffusion of real vortex flows appears around hundred times faster than molecular diffusion alone. Furthermore, the time-wise growth of the Lamb-Oseen has another shortcoming. For wakes of very small age, meaning $t \to 0$, the function shows a singularity. This leads to artificially high values close to the vortex' origin. The modified version of Squire takes this into account by including a time ordinate-shift, which provides a more physically correct swirl velocity. For rotating wings like wind turbine rotors, it is more convenient to describe the wake age as an angle. This can be easily rewritten using the definition of angular velocity in the rotor plane. The final form of the improved Lamb-Oseen result is given in Eq. 10.20. Here, the time-shift parameter r_{c0} controls the effective core radius at the initial time of the vortex origin.

The coupled effects between the viscous diffusion and the filament stretching can be explained with Helmholtz first law, from Section 10.1.3. Starting from the conservation of mass in incompressible flow, an increase in length of the vortex filament is directly related to a decrease in cross-sectional area. As the strength of the vortex filament must be constant in time, a deformation of the filament will therefore cause a counteracting change of vorticity. Since these effects are most prominent in the close vicinity of

the vortex filament, general adaptations are applied on the viscous core radius. Vortex stretching can be implemented as a correction factor on the core radius, as shown in Eq. 10.21, where ε denotes the relative change of length. Since the vortex' future state is now included in the computation of the current movement, it creates a coupling issue. The most common approach to tackle the issue at hand is the concept of "equivalent-time" [102]. Here, the additional straining effects are translated to a time-offset of the core's origin, presented in Eq. 10.22. The numerical implementation of the complete viscous-splitting algorithm in the free-vortex wake code will be further explained in Section 10.2.4.

$$r_{c_{eff}} = r_{c_0} \cdot \frac{1}{\sqrt{1+\varepsilon}}, \qquad \varepsilon \equiv \Delta\ell/\ell_0 \tag{10.21}$$

$$r_c(\xi_t, \varepsilon) = \sqrt{4\alpha_{lo}\,\delta_v \nu\,(\xi_{t_{0,eff}} + \xi_t)} \tag{10.22}$$

10.1.5. Flowfield approximation

As previously explained in Section 10.1.3, any well-behaved vector field can be described using the Helmholtz decomposition. This opens up the possibility to define the velocity field around a three-dimensional lifting body as a combination of sources and vortices. The vortex-induced velocity is then a triple field integral of the vorticity field. To reduce the dimension of the integral, the vorticity volume can be lumped into vortex sheets, or twice into vortex lines. It can be interpreted as a shrinkage of the volume element, where one of the spatial dimensions goes to zero. These geometric simplifications to reduce the dimension of the flow field representation are shown in Figure 10.6. In the lifting line method, the vorticity field is concentrated to a single line of vortex strength, located at the quarter chord. The lumping process, however, has one major drawback, as it alters the velocity distribution and creates a singularity at the vortex element.

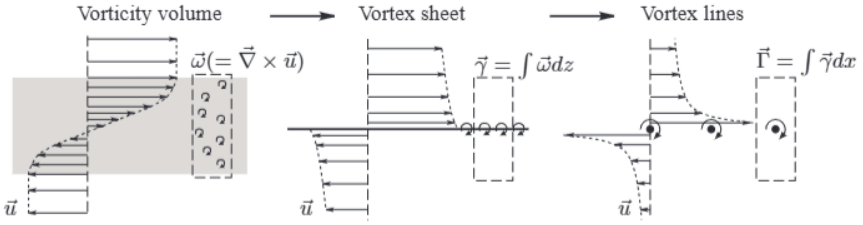

Figure 10.6: Dimension reduction of vorticity field via lumped forms [101]

10.2. Numerical implementation

Based on the theoretical framework, a numerical model has been developed: *K-TWIST*. The flow field is defined in a 3D cartesian coordinate system with an Euclidean frame of reference. The blade aerodynamics are represented by a nonlinear iterative procedure, while the wake system is described by a time-marching free wake method. The viscous-splitting algorithm is applied to treat the effects of vortex convection, diffusion and stretching independently. To accelerate the simulation, the model is equipped with a just-in-time compiler for parallel computation.

10.2.1. Global- and local coordinate system

The LLFVW model will be operating in a global three-dimensional cartesian coordinate system (X, Y, Z). The frame of reference is Eulerian, which means a fixed point of origin and independently of time. The zero-point of all three axis will be located at the base of the first wind turbine tower. As shown in Figure 10.7, the positive x-direction is chosen to be in the downstream direction and the positive z-direction towards the rotor. The positive y-direction is then chosen to coincide with the standard orientation of a right-handed coordinate system.

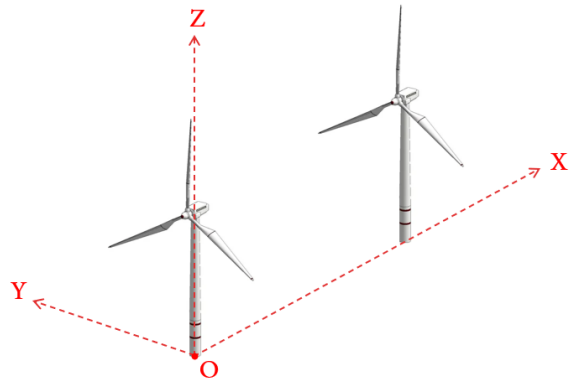

Figure 10.7: Global 3D cartesian coordinate system, with the origin at the first turbine's tower base. X streamwise, Y spanwise and Z vertical.

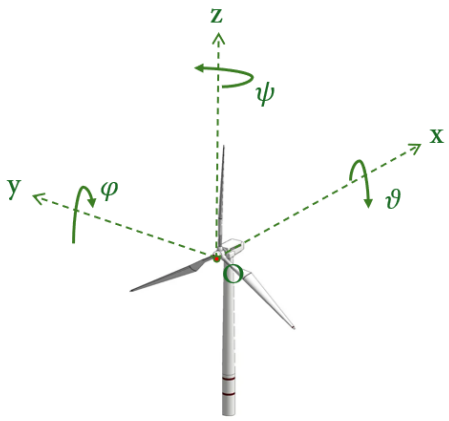

Figure 10.8: Local 3D cartesian coordinate system, with the origin at rotor's center. x streamwise, y spanwise and z vertical. Turbine rotations around the respective axis: roll (ϑ), pitch (φ) and yaw (ψ)

Each individual wind turbine will have their own local cartesian coordinate system. This allows for convenient use of different turbines or a disparity in their orientation with respect to the global reference point. As visualized in Figure 10.8, the origin will be located at the center of the rotor disk: the rotor hub. To reduce the complexity of the coordinate transformation to the global system, the positive direction of the axis are chosen with the same rationale. In order to switch between the local and global coordinate system, the coordinates will be transformed using a combination of translation and rotation. The translation corresponds with the shift of the origin's location, while the rotation provides the difference between the direction of the respective axis. For a wind turbine, these rotations around the x-, y- and z-direction are known as roll (ϑ), pitch (φ) and yaw (ψ), respectively. It must be noted that this pitch angle is not equal to the blade pitch angle, but can be used to rotate the complete turbine, as with floaters. Numerically, these conversions will be conducted using transformation matrices, shown in 10.23, 10.24 and 10.25. These matrices are dependent of the global turbine location and angles, which can be allocated individually.

$$\vec{X} = \mathbf{T} \cdot \mathbf{R} \cdot \vec{x} \tag{10.23}$$

$$\mathbf{T} = \begin{bmatrix} 1 & 0 & 0 & X_t \\ 0 & 1 & 0 & Y_t \\ 0 & 0 & 1 & Z_t \\ 0 & 0 & 0 & 1 \end{bmatrix} \tag{10.24}$$

$$\mathbf{R} = \mathbf{R}_\vartheta \cdot \mathbf{R}_\varphi \cdot \mathbf{R}_\psi \tag{10.25}$$

$$\mathbf{R}_\vartheta = \begin{bmatrix} 1 & 0 & 0 & 0 \\ 0 & cos\varphi & -sin\varphi & 0 \\ 0 & -sin\varphi & cos\varphi & 0 \\ 0 & 0 & 0 & 1 \end{bmatrix}, \mathbf{R}_\varphi = \begin{bmatrix} cos\vartheta & 0 & sin\vartheta & 0 \\ 0 & 1 & 0 & 0 \\ -sin\vartheta & 0 & cos\vartheta & 0 \\ 0 & 0 & 0 & 1 \end{bmatrix}, \mathbf{R}_\psi = \begin{bmatrix} cos\psi & -sin\psi & 0 & 0 \\ sin\psi & cos\psi & 0 & 0 \\ 0 & 0 & 1 & 0 \\ 0 & 0 & 0 & 1 \end{bmatrix}$$

The rotation matrix is a multiplication of three individual matrices, where each computes a rotation around a single axis. For conversions in 3D, the matrices are of the shape *4x4*, such that the rotation and translation can be described in a single matrix framework. Since translation does not conserve the origin, it is considered affine in vector algebra. To write the translation as a vector-matrix multiplication, an additional dimension is needed to close the linear system within a single matrix [108]. This process can be

achieved using homogeneous coordinates, where the extra coordinate is often set to 1. In 2D, this can be interpreted as the distance from a screen to the projector.

Due to the rotational position of the rotor blades in time, it is more convenient to describe their location in a local cylindrical coordinate system (r, ϕ, x). As shown in Figure 10.9, the cylinder will be centered at the rotor hub and the z-direction aligned with the rotor axis in downstream direction. With matching point of origin with the local cartesian frame, the cylindrical coordinates can be rewritten to the cartesian system with Eq. 10.26.

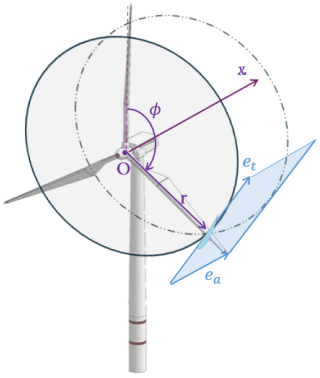

Figure 10.9: Local cylindrical coordinate system, with the origin at rotor's center. x streamwise, r radial and z azimuthal position.

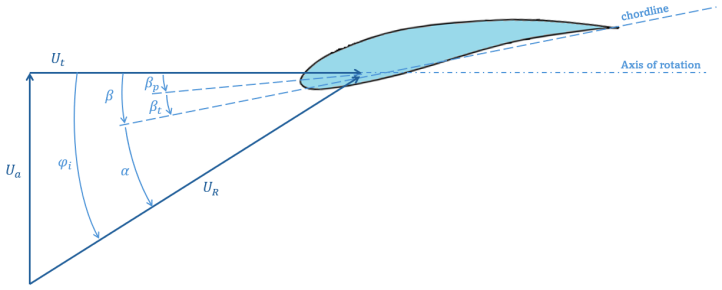

Figure 10.10: 2D local frame in a rotating reference system, defining the relative incoming velocity (U_R) and the blade angles (φ_i, α, β)

$$\begin{bmatrix} x \\ y \\ z \end{bmatrix}_{(x,y,z)} = \begin{bmatrix} x \\ -rcos(\phi) \\ rsin(\phi) \end{bmatrix}_{(r,\phi,x)} \tag{10.26}$$

In order to easily define the location of the leading edge and the trailing edge of the rotor blade sections, it is preferred to establish a blade-fixed reference frame. The coordinate system is defined to rotate with the blade, such that at each blade section, the velocity vectors lie in the a,t-plane and 2D aerodynamics can be applied. As visualized in Figure 10.10, the axial axis corresponds with the turbine's local x-axis and can be transformed directly. The tangential axis can be rewritten to the local cartesian frame with the use of the cylindrical frame of the rotor disk. This configuration of several local coordinate systems allows for efficient and compact expressions, from the sectional blade's chord all the way up to a single global reference system, where all the computation takes place.

10.2.2. Blade geometry and discretisation

In the lifting line FVW model, the geometry of each rotor blade is approximated by spanwise discretisation of blade segments. The model is programmed to allow six discretisation methods: uniform, cosine, sine, cubic, tangent and inversely tangent. These methods allow for different point distributions on the line, as visualized in Figure 10.11. In rotor wake aerodynamics, it is common to use a cosine function, since this increases the resolution at the blade ends where the largest variation of circulation is found [101]. The radial point of each blade section is then derived by Eq. 10.27, following equiangular increments. Here, the radial discretisation starts at the root (r_r) and ends at the tip radius (r_t), which is equivalent to the rotor radius R. As the blade geometry near the center of the rotor changes quickly, for structural stiffness and strength, and has a very low contribution to the lift production, it is common to have an effective root radius of around 20 to 30%.

The blade thickness is assumed to be infinitely small and its effect is neglected. The chord and local twist angle are assumed to vary linearly between the two endpoints of the rotor blade, described by Eq. 10.28 and 10.29. The radial distance is made non-dimensional with the rotor radius and A-D are constant input parameters.

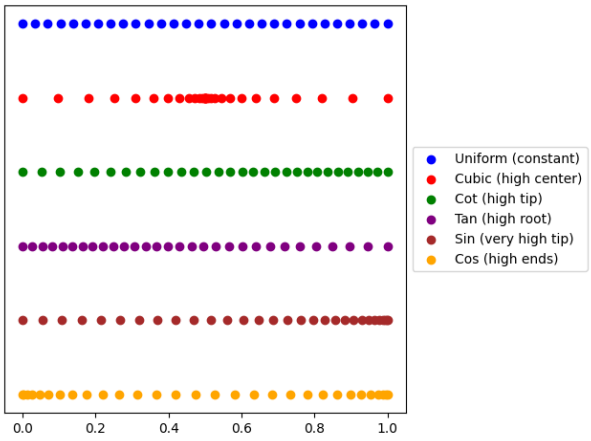

Figure 10.11: Different techniques for the spanwise discretisation of the blade

$$r_i = r_r + \frac{R - r_r}{2}\left[1 - cos\left(\frac{i\pi}{N}\right)\right] \qquad ; i = 0, 1, 2, \ldots, N \tag{10.27}$$

$$c(\hat{r}) = A + B \cdot (1 - \hat{r}) \tag{10.28}$$

$$\beta_t(\hat{r}) = C + D \cdot (1 - \hat{r}) \tag{10.29}$$

The aerodynamic coefficients are established from linear interpolation of the 2D-polar at the control point of each segment. These control points lie on the lifting-line at quarter chord and are distributed according to the corresponding spanwise discretisation technique. The 2D polar of the aerodynamic lift-, drag- and pitching moment coefficients is pre-established from the aerodynamic profile of the rotor blade. For simplicity is the design of the geometry equal throughout the full span of the blade.

10.2.3. Bound circulation

The forces of the blade on the flow are expressed into vortices, which are bounded to the blade. This form of external potential flow in the vorticity equation of Eq. 10.2 follows the motion of the blade in time. This movement does not follow the same dynamics as the Lagrangian markers of Eq. 10.16, but is linked to the generation of aerodynamic lift via the theory of Kutta-Joukowski from Eq. 6.3. In this model, two different approaches will be used to define the distribution of bound circulation on the blades. The vortex strength (Γ_B) can either be prescribed by a radial function or be established iteratively.

Prescribing a constant distribution allows for easy comparison with reference data or theory, like an elliptical loading for minimum induced drag. However, the distribution must be known in advance and equal for every timestep. There is an underlying assumption that the bound circulation is independent of time. This is a valid premise for steady- or full converged flow, but neglects the unsteady development of the aerodynamic lift.

To better capture this unsteadiness in the flow, a more complex nonlinear iteration can be used. In this approach, the lift force generated by the bound vortex is corrected using the nonlinear lift curve of the airfoil, corresponding to the control point of each blade section. The algorithm aligns the lift due to circulation from the Kutta-Joukowski theorem with the local lift force from the relative wind velocity. The numerical implementation is based upon ”The AWSM project” by van Garrel [101]. In Figure 10.12, the technique is illustrated in basic steps. For a more comprehensive and detailed description of the method, the reader is referred to the original publication.

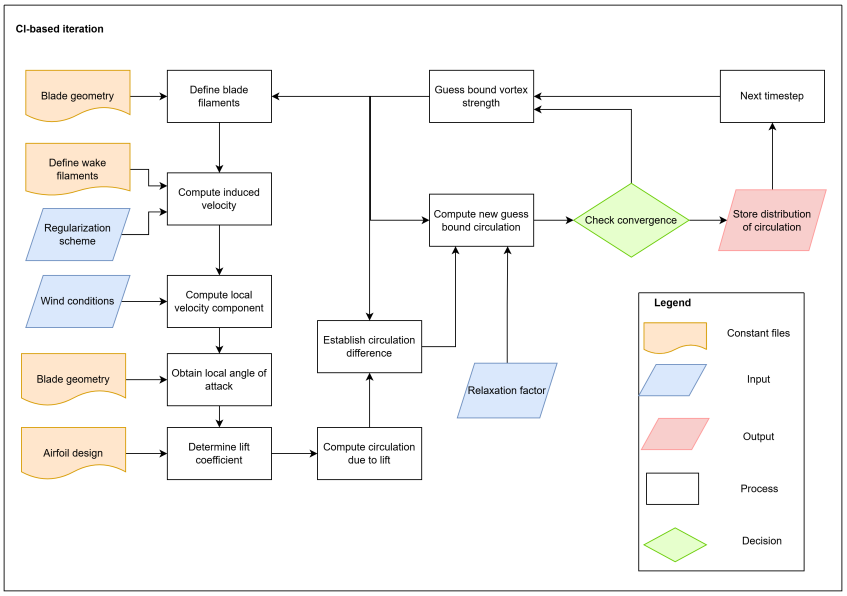

Figure 10.12: Simplified flow chart of the nonlinear CI-based iterative approach, modified from ”the AWSM module” [101]

10.2.4. Wake aerodynamics

Wake vortex system

According to the second theory of von Helmholtz (10.1.3), a vortex line must from a closed loop or extend to infinity. Therefore, any directional change in circulation must be accompanied by an equivalent vorticity component in the opposing direction. In other words, the vortex line does not terminate at the end points, but changes direction. In classical lifting line theory, the single bound vortex line bends at both ends in the downstream direction, creating a pair of trailing vortices that extend to infinity. Together with the bound vortex, these form a so-called ’horseshoe vortex’, which is theoretically enclosed by the starting vortex. Ludwig Prandtl further expanded this concept by dividing the lifting line into several spanwise sections, allowing for a more refined distribution of aerodynamic loading on the blade. As this initiates a spanwise variation of bound circulation, smaller trailing vortices will appear at each intersection of blade segments.

In a time-marching FW method, the aerodynamic loading on the blade may vary with time. This creates an unsteady component of the bound circulation, which is captured at the end of the airfoil into discrete step changes. These vortex lines, identified as shed vortices, effectively represent the time-wise variation of bound vortex strength. At the initial time step, $t = 0$, the aerodynamic loading on the blade is introduced, resulting in an abrupt change in circulation. In order to comply with Kelvin’s circulation theorem (Eq. 11.1), conserving total vorticity, a vortex of equal strength and opposite direction must be shed in the wake. This shed vortex line is placed at the trailing edge and represents the starting vortex. For the case of predetermined distribution of circulation, there will not be any variation of circulation in time. Due to this time-independency, all shed vortices beyond the starting vortex will be equal to zero.

At each timestep, newly generated vortices on the blade are shed from the trailing edge into the wake downstream. Looking at a single blade section, the combination of bound vortex with the two trailing vortices and the shed vortex forms a closed loop. This torus-shaped vortex of constant circulation is known as a *vortex ring element*, visualized in Figure 10.13. It’s strength Γ_O is equal to the bound circulation at the corresponding blade section and time step when it was generated. As these shed wake rings are convected over time, together they create the total free wake, modeled as a vortex sheet.

To satisfy the Kutta condition of vortex flow, which states that ”the flow leaves the sharp trailing edge of an airfoil smoothly at a finite velocity”, the total vortex strength at the trailing edge must be zero. By placing the lifting line at the quart-chord line and shedding the vortices from the trailing edge of the blade, this condition is automatically satisfied.

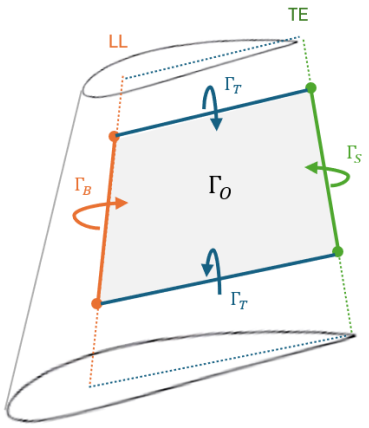

Figure 10.13: Definition of the vortex ring element, an enclosed structure of constant vorticity

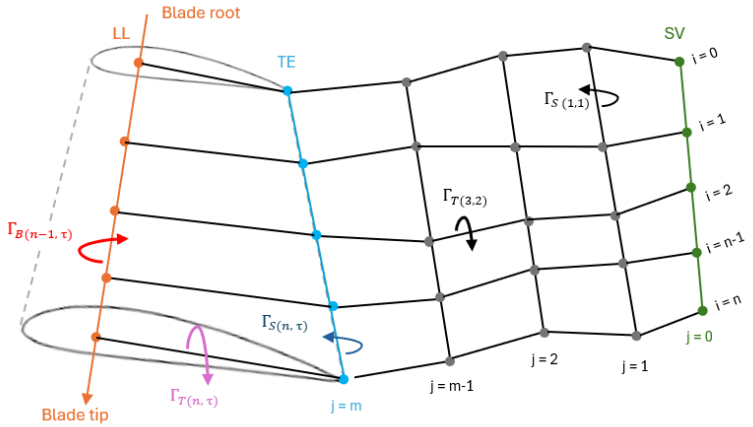

Figure 10.14: Geometry of the wake vortex system: Combined vortex sheets in a dual indexing scheme

As shown in Figure 10.14, the wake vortex system is modeled as a network of straight vortex filaments, interconnected between *wake nodes*. Each wake node is uniquely defined by a pair of indices (i, j). The first number i represents the spanwise position on the blade, in line with the index of the corresponding blade node. It ranges from zero to the total number of spanwise blade segments n. The second number j denotes the time index, indicating the number of elapsed time steps. At $j = 0$, representing the initial time, the location of the starting vortex can be obtained. The index increases with each successive time step, where the highest value corresponds to the current time point in index notation m.

The wake vortex filaments follow a similar dual indexing system. Since trailing vortices denote spanwise differences, the number of vortex lines is equal to the number of blade nodes. They are bounded by two wake nodes of the same spanwise index i and succeeding time indices j and $j + 1$. In contrast, shed vortices represent time-wise variation and they are stretched between two consecutive time steps. They level the number of blade sections and are defined between wake nodes with the same time index j, but with adjacent spanwise position i and $i + 1$. The strength of the trailing- (Γ_T) and shed vortices (Γ_S) are computed with Eq. 10.30 and Eq. 10.31, respectively. A visual overview of the complete wake vortex structure is presented Figure 10.14.

$$\Gamma_{T_{(i,j)}} = \Gamma_{B_{(i,\tau)}} - \Gamma_{B_{(i+1,\tau)}} \quad ; i = 0, 1, \ldots, n \;\&\; j = 1, 2, \ldots, m \tag{10.30}$$

$$\Gamma_{S_{(i,j)}} = \Gamma_{B_{(i,\tau)}} - \Gamma_{B_{(i,\tau-1)}} \quad ; i = 1, 2, \ldots, n \;\&\; j = 0, 1, \ldots, m \tag{10.31}$$

Numerically, the wake structure is created by convecting the wake nodes, rather than convecting the vortex filaments themselves. Since adjacent filaments share nodes, convecting filaments would result in duplicated effort, leading to higher computational time. By individually convecting the wake nodes, the computation is not only simplified, but it inherently deals with aspects of the ”vortex stretching”, as discussed in Section 10.1.4. Each wake node is convected with its local velocity vector, which is a combination of the free-stream velocity and the vortex-induced velocity. The induced velocity is the outcome of all bound-, trailing- and shed vortices, combined from each section and rotor blade.

Viscous-splitting

As previously described in Section 10.1.4, the effects due to viscosity in the vorticity equation will be resolved separately. The motion of the vortices will be driven by simple convection of Lagrangian markers. The position vector of the marker in the governing equation of Eq. 10.16 can be written as a function of the azimuthal angle (ϕ) and the wake age (ξ_ϕ). Using the angular velocity of the rotor, simulation time can be converted into an angle, following Eq. 10.32. The wake age, representing the elapsed time, is defined as the angle between the current azimuthal position and the position when it was shed at the trailing

edge (Eq. 10.32). Using the chain-rule, the Lagrangian convection can be expressed in a blade-fixed coordinate system with Eq. 10.34. The velocity term in the RHS of Eq. 10.34 is severely non-linear and will be solved numerically using recurrent implementation of the Biot-Savart law, for each vortex filament respectively. The combined set of equations from each Lagrangian marker, effectively spatial and time discretisation, can be seen as a system of ordinary differential equations. These can be solved using numerical time-marching integration methods, like the Forward-Euler, the Runge-Kutta and other higher order methods.

$$\phi = \Omega t \tag{10.32}$$

$$\xi_\phi \equiv \phi - \phi_0 \tag{10.33}$$

$$\frac{\partial \vec{r}}{d\phi} + \frac{\partial \vec{r}}{d\xi} = \frac{\vec{q}(\vec{r}, t)}{\Omega} \tag{10.34}$$

The principle of the viscous-splitting algorithm is described as a time-marching operation, where three consecutive steps are handled sequentially. From the schematic diagram of Figure 10.15, we observe that the first sub-step is the convection. This inviscid process will be conducted according to the movement of a Lagrangian fluid marker in the local velocity field. The second sub-action is applied to account for the effects due to viscous diffusion of the vortex filaments in time, while the third step accounts for the viscous-coupled effects due to stretching of the vortex elements. These last two viscous processes appropriately correct the initial vorticity field due to convection alone, which is equivalent to setting the convection term to zero.

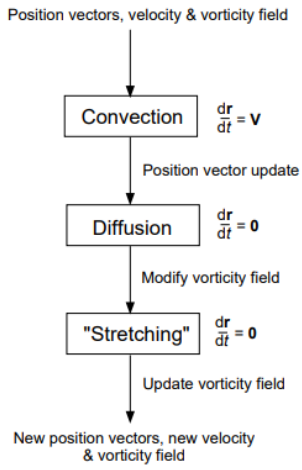

Figure 10.15: Viscous splitting algorithm for FVW methods [102]

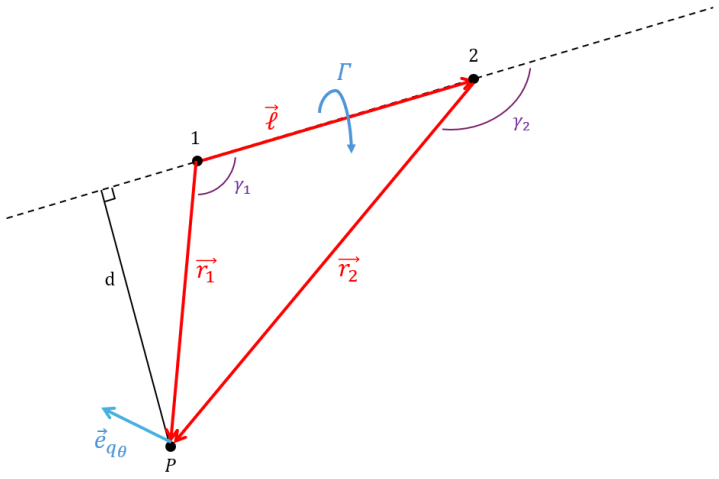

Figure 10.16: Nomenclature used for induced velocity calculations by three-dimensional straight vortex, adapted from [105]

The numerical implementation of the Biot-Savart law for the calculation of vortex-induced velocity at the Lagrangian markers can be described using Figure 10.16. The straight vortex filament of strength Γ, between point 1 and 2, induces a velocity at an arbitrary point P, which is at an orthogonal distance of d from the filament. The individual components of Eq. 10.15 can then be filled in to calculate the absolute value of the induced-velocity vector. The vector direction is normal to the plane span by the vortex filament and the evaluation point, which can be expressed in mathematical terms using Eq. 10.35. Using vector calculus, the vortex-induced velocity calculation can be rewritten to Eq. 10.36. Here, the additional term K_v is the regularization parameter that accounts for the effects in the close vicinity of the viscous core.

$$\vec{e_{q_i}} = \frac{\vec{r_1} \times \vec{r_2}}{|\vec{r_1} \times \vec{r_2}|} \tag{10.35}$$

$$\vec{q_i} = K_v \frac{\Gamma}{4\pi} \frac{\vec{r_1} \times \vec{r_2}}{|\vec{r_1} \times \vec{r_2}|^2} \left(\frac{\vec{\ell} \cdot \vec{r_1}}{r_1} - \frac{\vec{\ell} \cdot \vec{r_2}}{r_2} \right) \tag{10.36}$$

$$\vec{q}_{i,co} = \frac{\Gamma}{4\pi} \frac{(r_1 + r_2)(\vec{r_1} \times \vec{r_2})}{r_1 r_2 (r_1 r_2 + \vec{r_1} \cdot \vec{r_2}) + (r_c \ell)^2} \tag{10.37}$$

$$K_{v,\,vas} = \frac{d^2}{(d^{2n} + r_c^{2n})^{1/n}} \tag{10.38}$$

$$K_{v,\,lo} = 1 - \exp\left[-a_{lo} \cdot \frac{d^2}{r_c^2} \right] \tag{10.39}$$

Since the Biot-Savart law describes vortex flow, it has a singularity when the evaluation point coincides with the axis of the vortex filament. As the point approaches the line, the induced-velocity becomes un-physically large due to assumption of concentrated vorticity. The most straightforward solution is to use a numerical cut-off scheme, where the solution smoothly decays to zero in close proximity. For this approach, the regularization parameter of Eq. 10.36 is dropped and the induced velocity is modified to Eq. 10.37, with an offset in the denominator indicated in blue. In literature, various other methods can be found to de-singularize this swirl-velocity field and prevent numerical problems. The simplest model is based on the observation that the vortex' core in a viscous fluid behaves like a solid body rotation of constant speed, known as the Rankine vortex. This method, however, has a discontinuity at the intersection of the "viscous" core inner- and the free vortex outer flow. Other alternative methods, like the Kaufmann vortex, use an algebraic profile of the swirl velocity, which removes the cusp. Both the Rankine- and the Kaufmann model, or Scully model, are part of the overlapping family of equations proposed by Vatistas, shown in Eq. 10.38, with $n \to 1$ and $n = 1$ respectively. These methods are purely mathematical and no longer represent the physical flow field around a lifting device, as it is not a solution to the Navier-Stokes equation. Despite their reasonably approximations to the solution, their assumption of inviscid flow is often incorrect and a more precise representation should including the viscous effects. Therefore, introduced by Lamb and Oseen, viscous diffusion is taken into consideration. This has been reflected into a time-evaluation of the viscous core radius, known as core spreading methods, as described in Section 10.1.4. Using the definition of the core radius from the Lamb-Oseen model, of Eq. 10.17, the regularization parameter can be expressed with Eq. 10.39. The effects in the close vicinity of the different vortex core models are shown in Figure 10.17, where the swirl velocity is normalized by the value at the core radius. As the Lamb-Oseen model is a physical solution to the one-dimensional Navier-Stokes equation and it is the foundation of the viscous splitting algorithm, it will be implemented as the default option in the current model.

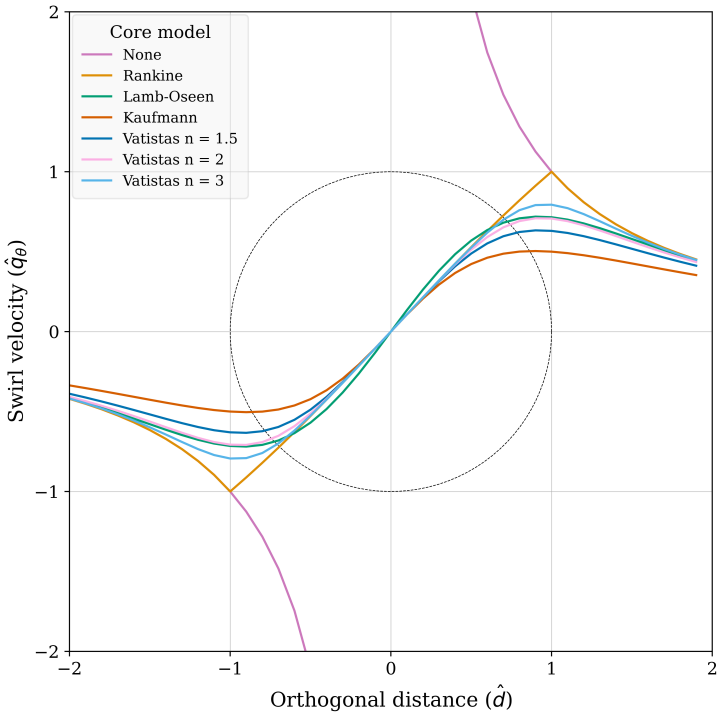

Figure 10.17: Normalized swirl velocity distribution around a vortex' center for different core models, including Rankine, Lamb-Oseen, Kaufmann and the Vatistas family. The vortex core is indicated as the Grey circle of radius one.

Initial viscous core radius

As described in Section 10.1.4, the viscous core radius is used to approximate the viscous behavior close to the origin of the vortex flow. At this point, the swirl velocity is maximum, and the flow characteristics deviate from a *free vortex*. This is one of the most critical parameters of a FVW model, due to its impact, partly on the regularization of the Biot-Savart law. The value is influenced by, inter alia, the chord length, the boundary layer thickness and the volume package that is being lumped into the vortex filament.

Empirical studies have found that the initial value of the viscous core radius of trailing tip vortices is in line with the blade tips' airfoil thickness [102], [107]. For most airfoil shapes this is on average about 10% of the local chord length. This value will be used as a fixed parameter throughout the study for all vortex types: bound, shed and trailing.

Time integration method

The system of differential equations that governs the convection of the Lagrangian marker of Eq. 10.16 can be solved using numerical techniques. While the RHS of the equation is tackled by repeated application of the Biot-Savart law, the LHS can be solved with time-marching integration schemes. The discretisation in time can be conducted with implicit or explicit practices. Explicit methods use only the information from current and previous time-steps to compute the next time value, while the implicit schemes require knowledge from future time-steps. As the value of the next time step depends on itself, they need additional computation. In some occasions, where the differential equation is very stiff, unreachable small time steps are needed for numerical stability, and it is more efficient to take an implicit approach.

In the current model, the standard integration scheme is the explicit Forward-Euler (FE). This simplistic method is based on the left rectangle rule to approximate the integral. Using only information at the current time point, the solution can be computed with Eq. 10.40. Although the FE method is very simplistic and cost-efficient, it requires a sufficiently small time step (Δt) for numerical stability. This optimal point will be further examined during the sensitivity study of the verification analysis in Section 11.1.3.

It should be noted that in the current design of K-TWIST, the timescale is defined in seconds, in line with the standard SI unit system. This all for direct integration of the time integration methods from

reference sources. Specifically for rotor simulations, however, this is not common. In most studies, time is rather expressed in rotation angle. Due to the circular motion of the rotor, periodic behavior may occur in aerodynamic quantities, which are harder to detect on standard SI time scales. Additionally, this temporal discretisation technique is also independent of rotational speed. In the standard approach, a simulation with higher rotor speed and equivalent time-step size contains fewer time increments for one revolution. Nonetheless, the standard SI system has been chosen, in order to provide a clear scale for the non-rotating, translating kite as well.

$$\vec{x}_{t+1_{FE}} = \vec{x}_t + [\vec{u}_\infty + \vec{q}_i(\vec{x}_t)]\Delta t \tag{10.40}$$

10.2.5. Computational environment

The K-TWIST model is coded in python script that allows for parallel computation by utilizing Numba, an open source just-in-time compiler [103]. Performing numerical calculations in parallel significantly decreases computational time for loops of matrix operations. This is particularly effective for time-marching FW models, where the number of nodes increases with every time step. For computations like the Biot-Savart law, the array sizes can get out of hand very quickly. Standard approaches in which only one entry is calculated can therefore take hours, for just a single timestep. In parallel computation, these independent jobs are distributed across multiple CPU cores and may lead to higher computational efficiency. However, the speed-up does not scale linearly with the number of processors due to overhead cost or memory limits. This is further explored in a CPU sensitivity analysis, presented in Section 11.1.3.

Due to the large scale, the simulation will be conducted on a high-performance computing (HPC) cluster, *the HPC12*. The ”supercomputer” is located on a dedicated Linux server, exclusively shared within the faculty aerospace engineering at Delft University of Technology. This cluster opens up the availability of significantly larger CPU numbers and available random-access memory (RAM), compared to standard laptops with corresponding capacities of six-core, 16GB RAM. More information on the HPC cluster, such as the operating system and the CPU-types, can be found on the *HPC12 Wiki* [104].

10.3. Post-processing

To convert the outcome of the numerical model into visible and meaningful aerodynamic properties, several post-processing techniques are applied to the computed flow-field data. This section briefly describes the main simulation outputs and the methods to extract them from the velocity field. Due to the discrete approximation of unsteady flow behavior in the numerical model, particular attention is brought to the utilization of averaging techniques, in order to produce useful results.

10.3.1. Output quantities

Since this study focuses on the impact of kite-deployment on the wake flow recovery of wind turbines, both rotor performance and flow behavior in the wake are of high interest. These features can be characterized by a wide variety of aerodynamic parameters. Given that the K-TWIST model is based on a lifting-line vortex method, it is opted to evaluate the rotor performance through distribution of circulation and global turbine performance characteristics, specifically the axial induction factor and the power coefficient. By visualizing spanwise distribution of bound circulation for multiple points in time, transient aerodynamic behavior of the flow can be identified. The time-averaged axial induction factor of blade segments can be computed directly from the resulting velocity field. Using discrete approximation, these local quantities sum up to an equivalent average induction factor, as shown in Eq. 10.41. On the contrary, the power coefficient cannot be calculated from the results straightaway. First, the spanwise lift distribution along the blade is computed from the bound circulation and the local velocity factor using the Kutta-Joukowski theorem of Eq. 6.3. These lifting segments contribute to the total power extracted by the rotor via torque and can be normalized with the available kinetic power in the wind, expressing the power coefficient. Numerically, these parameters are achieved from Eq. 10.42 and Eq. 10.43.

$$\bar{a} \approx 1 - \frac{1}{N} \sum_{i=1}^{N} \frac{U_{x,i}}{U_{x,\infty}} \tag{10.41}$$

$$P = \rho \, \Omega \sum_{i=1}^{N} [\Gamma_i \cdot U_{R,i} \cdot r_i \cdot \Delta r_i] \tag{10.42}$$

$$C_P = \frac{P}{\frac{1}{2}\rho A U_{\infty}^3} \tag{10.43}$$

Regarding the wake flow, both qualitative and quantitative representations are presented. The wake geometry and tip vortex trajectories provide visuals of the flow structure, including tip vortex roll-up and wake expansion. Concurrently, quantitative measures are extracted, in the form of axial velocity deficit and vertical momentum flux of the mean flow. Both parameters can be computed directly from the velocity field that results from the K-TWIST model, following Eq. 4.1 and Eq. 4.3 respectively.

10.3.2. Data averaging

Given the discrete and unsteady nature of the LL-FW solver, raw data from the simulation may contain nonphysical oscillations or asymmetry. In key velocity-related drivers of this study, like the velocity deficit along the rotor axis, noise can appear from blade passage or abrupt vortex influence. Therefore, several smoothing techniques are applied, to obtain clear, representative trends from the produced data.

When the velocity deficit is plotted against the azimuthal angle, for a given radial position and a fixed downstream location, the signal shows a periodic pattern. The number of peaks corresponds with the blade count of the rotor, highlighting the strong effect of blade passage. Assuming perfectly symmetrical wake geometry, azimuthal averaging can be applied to the simulation data. For each downstream evaluation point, data is collected at discrete azimuthal angles with equal radial position. Subsequently, these results are averaged for one full revolution to obtain the mean value. The azimuthal averaging filters out the blade-passage effect, producing a smooth representative velocity field. It should be noted that this approach can only be used in cases where there is no significant wake meandering or where the wake deforms asymmetrically, such as in yaw.

Sampling the velocity at a given downstream location while varying the radial location, reveals strong fluctuations around the edges of the blade. The axial velocity near the root and tip even increases, as a result of strong influence from the tip vortices. Given that most simulations exclude the inner portion of the blade, the resulting raw velocity field may appear to speed up near the center of the wake region. As this does not represent physical reality, analysis along the rotor axis needs additional processing. To obtain the rotor-averaged velocity on the axis of rotation, the data needs to be integrated across the rotor disk. Numerically, this is handled through weighted averaging based on the annular area, to ensure proportional contribution from each radial blade section. This technique is used in a similar manner to compute global rotor metrics, like axial induction factor and power coefficient, where a representative value is required for the effect of the entire rotor. These annular-averaged quantities better reflect the real turbine performance characteristics that can be used for comparison with reference data.

In post-processing studies of experimental data, the point-fixed flow field is often averaged in time over several rotor revolutions to filter out temporal noise. In this study, the wake is only simulated for a limited number or revolutions, due to its impact on the computational time. As such, time-based averaging is not suitable. However, azimuthal averaging at given time points implicitly assumes quasi-steady flow for one rotor cycle. Since the average value is computed at multiple downstream evaluation points, the result can be interpreted as a representative time average, provided that the wake geometry remains symmetric.

Part IV

Research Results

11

Verification & validation

Verification and validation are crucial steps to evaluate the accuracy and reliability of a numerical model. This credibility assessment provides the basis to ensure that the simulation results are plausible and reliable approximations of the modeled physics. Before applying the model to complex scenarios or drawing conclusions from its results, it is important to assess whether the numerical implementation is mathematically correct, as well as physically representative of the simulation case.

The first part, focusing on the numerical accuracy of the governing mathematical equations, is covered by the verification analysis in Section 11.1. This process focuses purely on the fidelity of the numerical implementation and the mathematical framework, with no involvement of physical modeling. It helps to detect programming errors, assess numerical convergence and ensures the alignment of the model with analytical solutions and benchmark cases. In other words, the verification seeks to answer a central equation: *"Are the equations being solved correctly?"*

Validation, on the other hand, determines to what extent the numerical model can provide an accurate representation of the physical reality. Here, the guiding questions is: *"Are the right equations being solved?"*, emphasizing the adequateness of the theoretical model itself. It often involves comparison of the simulation results with high-fidelity data or experimental measurements from reference studies. This evaluates whether the dominant physical phenomena are captured by the model, ensuring its applicability within a defined range of conditions. How to validation process is employed for the current K-TWIST model will be further discussed in Section 11.2.

11.1. Verification

The verification procedure of this work is divided into three series of tests: consistency checks (11.1.1), configuration trials (11.1.2) and sensitivity studies (11.1.3). These steps involve: evaluation of the numerical model with respect to fundamental conservation laws, reproducibility of analytical solutions in simplified conditions, and analyze convergence behavior under variation of key discretisation parameters. The sensitivity analysis, most importantly, examines how the model reacts to changes in design parameters. These variables, including time step size, wake length and total number of blade segments, effectively define the spatial-time mesh of the simulation. It provides insight into the robustness and numerical stability of the model, which are essential for identifying an optimum of model accuracy to computational efficiency. Since FW-based models show a quadratic relation with the number of elements, tuning the simulation parameters is very important to ensure valid results with minimal energy consumption. This section outlines the steps employed in the verification of the K-TWIST model, as well as the key results.

11.1.1. Consistency checks

The first set of unity checks are conducted statically, only once for the initial setup. These essentially test whether the geometry and core physics are correctly implemented in the numerical setup. To verify the vortex orientation, a single line element is inspected to align the induced-flow direction with the right-hand rule from the Biot-Savart law. Similarly, the implementation of a vortex ring element is tested by isolating the four components of the closed loop. They should sum up to net zero circulation and generate a downstream downwash effect, for a positive vortex strength. Here, both visual and numerical checks will be performed on a single blade with two nodes. The implementation of the Biot-Savart law is examined by

plotting the swirl velocity from an isolated vortex filament against the orthogonal distance. In principle, the induced-velocity must start from zero and approach the analytical solution of a semi-infinite vortex line (Eq. 6.2). Lastly, the geometry of the simulation setup is checked by plotting the wind turbine blades in a fixed three-dimensional reference system over a few time steps. With this figure, the direction of rotation, relative inflow velocity vector, airfoil chord direction, and node placement can be confirmed.

Additional consistency checks are applied for every timestep in the numerical simulation, to ensure concurrence with the fundamental theorems of Kelvin and von Helmholtz, as described in Section 10.1.3. In the K-TWIST model, Kelvin's conservation of circulation is checked by calculating the total circulation over the whole domain, effectively summing every filament contribution (Eq. 11.1). The first theory of von Helmholtz, asserting vortex filament time invariance, can be monitored by time evaluation of a single vortex filament in the wake. However, since the strength of a filament is only allocated at creation, this notion is automatically fulfilled with Eq. 11.2. With the definition of shed vortices as the temporal variation of bound circulation, Helmholtz's second law is met unconditionally as well. Any remaining delta is caused by accumulation of numerical errors.

$$\Gamma_B + \sum_{i=1}^{I} \sum_{j=1}^{J} \left[\Gamma_{T_{i,j}} + \Gamma_{S_{i,j}} \right] = 0 \tag{11.1}$$

$$\Gamma(t) = \Gamma(t + \Delta t) = const. \tag{11.2}$$

These tests primarily serve as a checklist to identify potential coding errors or other inconsistencies, including geometric configuration and theoretical limits. Therefore, the corresponding results are summarized in Section A.1

11.1.2. Configuration trials

To further verify proper implementation of key aerodynamic phenomena, a selection of configuration trials is performed using the numerical model. These simplified test cases serve as a benchmark for direct comparison with analytical solutions. Here, the models' ability to reproduce fundamental flow behavior, such as lift generation, downwash, vortex roll-up, wake expansion and tip vortex patterns can be checked systematically. In this study, three distinct configuration trials are carried out under idealized, steady flow conditions using a symmetric airfoil, specifically the *NACA0012*. The corresponding two-dimensional airfoil data, including the Cl, α-curve, is obtained from XFoil simulations at a Reynolds number of six million. An overview of the operating conditions is presented in Table 11.1

Table 11.1: Simulation conditions for the verification analysis of the K-TWIST model

Case variable	Symbol	Setting	SI Unit
Free-stream velocity	$U_{x,\infty}$	10	m/s
Flow density	ρ	1.225	kg/m^3
Kinematic viscosity	ν	1.48E-5	m^2/s

The first series of simulations are conducted for the test case of a single, untwisted, elliptical wing of finite span. The wing's geometry is defined by an elliptical chord distribution, a constant geometric pitch angle and a straight quarter chord line, as shown in Figure 11.1. Since the wing translates axially without rotation, the pitch angle is equal to the aerodynamic angle of attack. At first, a quick check is performed for a zero angle of attack to check the condition of no lift generation. More importantly, a non-zero constant angle should generate an elliptical lift distribution. Given that the inflow conditions are steady, this is equivalent to a distribution of circulation of the same shape. This can be verified by comparing the variation of bound circulation with the analytical solution of Eq. 11.3. More conveniently, a verification is conducted by plotting the spanwise- and temporal variation of induced downwash for a prescribed distribution of bound circulation. By definition, both the downwash and the induced angle of attack must be constant along the wingspan, at the three-quarter chord line. This follows from the no flow boundary condition of modeling a lifting surface [105]. Defined by Eq. 11.4, it is a function of the maximum circulation Γ_{max} and the wing

span b. The simulation will run for small time steps of $0.05s$ for several diameters of traveled distance in the downstream direction, to obtain a smooth and evident wake definition. At last, anti-symmetry across the centerline is tested by mirroring the wing on the y-axis. Since the sign of the angle of attack is now flipped, the aerodynamic response of the wing should be of equal magnitude and opposite direction (Eq. 11.5).

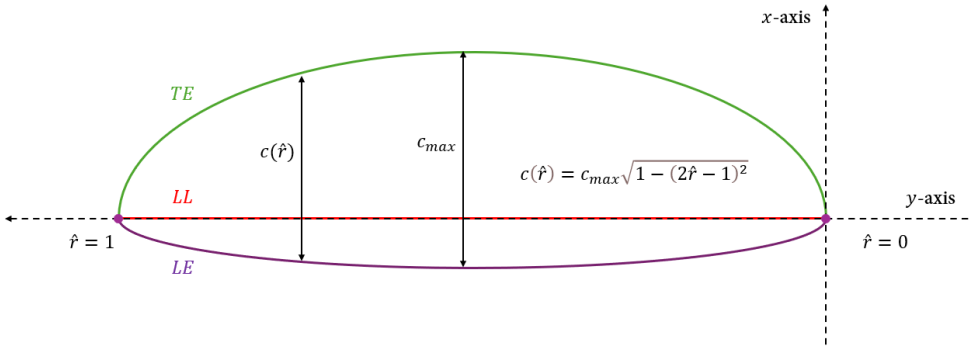

Figure 11.1: Geometry definition of untwisted elliptical wing, with straight quarter chord line

$$\Gamma(y) = \Gamma_{max}\sqrt{1-\left(\frac{y}{b/2}\right)^2} \tag{11.3}$$

$$w_i = -\frac{\Gamma_{B_{max}}}{2b} \tag{11.4}$$

$$\Gamma(r) = -\Gamma(-r) \tag{11.5}$$

For a complete overview of this chain of simulations, the reader is referred to Section A.2. Here in this subsection, only the key findings related to the induced downwash for the non-zero constant angle of attack are presented. In Figure 11.2, the time evolution of the downwash is plotted for different spanwise positions. Since the bound circulation is a prescribed function, it is constant in time. All shed vortex filaments will be zero, except the starting vortex. In the simulation, the sudden change in motion at constant speed causes a fast increase of downwards airflow, as seen in Figure 11.2. This disruption, due to shedding of the initial shed vortex downstream, will slowly move away from the wing. The downwash will converge to a steady value after approximately $1.5s$. From the graph, it can be observed that the downwash is moderately constant for the large part of the span. Towards the end points of the wing, the downwash is significantly larger. The differences between the simulation and the analytical solution are related to the assumption of flat wake. However, due to wake self-induction, a phenomenon called wake roll-up appears and the assumptions does not hold. At the wing tips, the spanwise differences of bound circulation are very large, causing peak trailing vortices that folds inwards in a cylindrical pattern. In Figure 11.3, the wake behind the lifting surface is plotted, where this phenomena can be spotted easily. It should be noted that the effect of the downwash on the wing loading is not accounted for in these results, which slightly over-predicts the bound circulation and, consequently, the induced downwash.

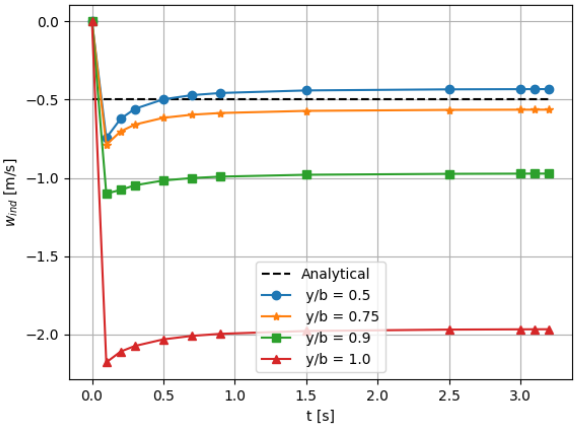

Figure 11.2: Induced downwash at three-quarter chord, for different spanwise locations of an untwisted elliptical wing

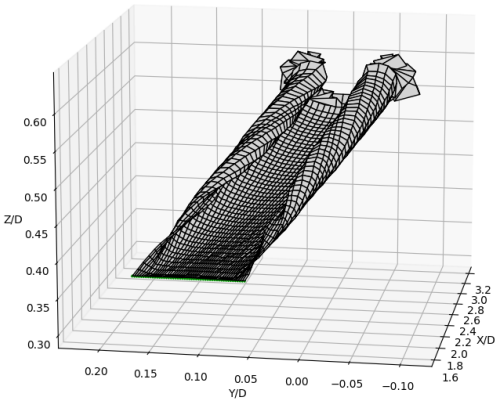

Figure 11.3: Wake geometry of an elliptical wing, showing tip vortex roll-up

Table 11.2: Geometric parameters for the verification analysis of an untwisted, elliptical wing

Case variable	Symbol	Setting	SI Unit
Number of blades	N_B	1	
Number of segments	N_S	50	
Non-dimensional radial distance	$\hat{r}$	0 – 1	
Blade span	b	10	m
Maximum chord length	c_{max}	3.18	m
Blade pitch angle	β_p	0 / 0.12	rad
Prescribed max. bound circulation	$\Gamma_{B_{max}}$	10	m^2/s

For the second configuration trial, the wake dynamics of a three-bladed rotor at constant angular velocity is simulated. For this part of the verification study, a tip speed ratio of 8 is defined, which relates the rotational speed to the wind speed following Eq. 11.6. The blade's geometry is designed to ensure that the rotor operates in a force-free state. In other words, the rotor is positioned in such a way that no aerodynamic lift is produced over the entire blade. This can be reproduced by aligning the local pitch angle with the inflow angle, for each blade segment. From Figure 10.10, this geometric condition ensures zero angle of attack. Defining the global rotor pitch angle to be zero, the twist distribution is a simple function of the tip speed ratio (λ). The function is presented in Eq. 11.7, where the radial position is normalized by the rotor radius. Given that the airfoil is symmetrical, the spanwise distribution of lift coefficient should therefore remain constant at zero. As there is no aerodynamic blade loading, there is no generation of circulation. The generated wake nodes should move downstream with the local velocity vector, creating a perfect helical wake pattern. This helix shape can be used as a baseline for all plots of the wake geometry, showing the deviation from the rotational effects of the rotor.

Decreasing the rotational speed slightly by 10%, while keeping the wind speed constant, the rotor should move into a turbine configuration. As the inflow angle increases and the geometry is fixed, the angle of attack increases as well. Positive lift is generated and the flow will be decelerated. Likewise, the rotor should simulate a propeller if the rotational speed is increased. For clarity, the results of this part have been moved to Section A.2

$$\lambda = \frac{\Omega R}{|\vec{U}|} \tag{11.6}$$

$$\beta_t(r) = arctan(\frac{1}{\lambda r}) \tag{11.7}$$

Table 11.3: Geometric parameters for the verification analysis of a three-bladed rotor at constant angular velocity

Case variable	Symbol	Setting	SI Unit
Number of blades	N_B	3	
Number of segments	N_S	25	
Non-dimensional radial distance	$\bar{r}$	0.2 – 1	
Rotational speed	Ω	1.6 $\pm$ 0.16	rad/s
Blade radius	R	50	m
Blade pitch angle	β_p	0	rad

For the third and final test case, a second simulation is performed for the three-bladed rotor. The geometry of the blade will be defined to create a constant loading on the rotor. This means that the spanwise distribution of thrust force is uniform. On the condition that the rotor is lightly loaded ($C_T \leq 0.2$), the inflow angle is small and the local axial force can be approximated by the lift per unit span. From the Kutta-Joukowski theorem of Eq. 6.3 and the thin airfoil theory, the local lift force can be expressed by Eq. 11.8. Still, the rotational speed of the rotor is constant and stems from the defined tip speed ratio. Using the same twist distribution as for the force-free rotor, a small constant angle of attack can be achieved by defining a global pitch angle. In order to achieve a constant lift force, the chord distribution is specified to be inversely proportional to the relative velocity, following Eq. 11.9. The results from this test configuration trials, like the wake geometry and the turbine performance quantities can be compared with semi-analytical expressions from BEM and Goldstein's theory. A summary of the results of this trial can be found in Section A.2.

$$L'(r) = \frac{1}{2}\rho\, V_R^2\, c\, C_L \tag{11.8}$$

$$c(r) \propto \frac{1}{V_R^2} \tag{11.9}$$

Table 11.4: Geometric parameters for the verification analysis of a three-bladed rotor with constant loading

Case variable	Symbol	Setting	SI Unit
Number of blades	N_B	3	
Number of segments	N_S	20	
Non-dimensional radial distance	$\hat{r}$	0.2 – 1	
Rotational speed	Ω	1.6	rad/s
Blade radius	R	50	m
Blade pitch angle	β_p	1.5	$^\circ$
Thrust coefficient	C_T	0.1	

11.1.3. Sensitivity analysis

To conclude the verification study on the K-TWIST model, a detailed analysis is conducted on the computational efficiency and numerical convergence behavior of critical simulation parameters. The

three-bladed rotor is defined to operate in turbine mode at a constant angular velocity. The geometry of the blade is described by a cosine spacing and linear functions for the twist and chord distribution, as discussed in Section 10.2.2. The flow conditions are assumed steady, similar to the configuration trials of Table 11.1. For this analysis, the *DU 95W-180* airfoil will be used for full blade span [109]. All geometric input parameters for the wind turbine blade are kept constant throughout the sensitivity study and are summarized in Table 11.5 on the left. On the right hand side of Table 11.5 are the baseline simulation settings. For each part of the analysis, only one of the variables is varied, while the others remain fixed. In this manner, the effect of the input parameter on the numerical results can be isolated.

Table 11.5: Input parameters for the sensitivity analysis of a three-bladed rotor

Geometric variable	Symbol	Setting
Number of blades	N_B	3
Radial distance	$\hat{r}$	0.2 – 1
Blade radius	R	50 m
Blade pitch angle	β_p	-2 $^\circ$
Chord constants	A, B	3, 1
Twist constants	C, D	14, 1

Simulation parameter	Symbol	Setting
CPU core count	N_{CPU}	10
Number of segments	N_S	15
Time step	Δt	0.05 s
Simulation time	T_{tot}	40 s
Rotational speed	Ω	1.6 rad/s

Numerical models based on the FW method tend to have a correlation between the number of wake nodes and the computational efficiency. At each timestep, the total nodes count increases with the number of trailing edge nodes. The number of wake filaments grows twice as fast, due to the creating of both trailing- and shed filaments. Since the nodes are individually convected, the induced velocity needs to be computed for each node. The total number of elements that need to be computed for a particular timestep can be approximated by Eq. 11.10. It is a function of the time step count (N_T) and the amount of blade nodes (N_{BN}). The latter is in itself a function of the number of aerodynamic devices (N_D), blades (N_B) and segments (N_S). With the continuously rising line, the maximum can be found at the last time step. At this point, the proportionality with respect to the input parameters is given by Eq. 11.12. However, these variables are also influential for numerical stability and modeling the physics, such as aerodynamic blade loading and wake flow behavior. It is therefore essential to find an optimal balance between computational cost and numerical accuracy. To achieve this, sensitivity analysis are carried out for the K-TWIST model, for both input variables and CPU performance.

$$N_{tot} = \underbrace{(N_{BN} \cdot N_T)}_{\text{wake nodes}} \cdot \left[\underbrace{(2 \cdot N_{BN})}_{\text{blade filaments}} + \underbrace{(2 \cdot N_{BN} \cdot N_T)}_{\text{wake filaments}} \right] \tag{11.10}$$

$$N_{BN} = N_R \cdot N_B \cdot N_S \tag{11.11}$$

$$N_{tot} \propto N_R^2 \cdot N_B^2 \cdot N_S^2 \cdot \underbrace{(T_{tot}/\Delta t)}_{N_T}{}^2 \tag{11.12}$$

Spatial resolution

Each rotor blade is modeled by a discrete number of spanwise segments N_S, which are defined with a cosine spacing method. Since the aerodynamic forces are lumped onto the lifting-line, it is the main parameter that defines the spatial resolution of the simulation mesh. Larger values of N_S contribute to a finer discretisation, in particular the twist and chord distribution across the blade span, which result in a more accurate representation of the blade geometry. This translates to a better approximation of the aerodynamic behavior, which is reflected in the spanwise variation of bound circulation.

The influence of the number of segments along the blade span on the aerodynamic loading is first illustrated in Figure 11.4, presenting the distribution of bound circulation for increasing spatial resolution.

As expected, a very coarse mesh ($N_S = 5$) fails to accurately track the spanwise variation of blade loading. The deviation is particularly evident at the blade root and tip, where the strongest gradients can be found. Increasing the number of sections, the blade can be represented more precisely, which leads to improved accuracy of the aerodynamic modeling. For an even higher number of elements ($N_S \geq 15$), a further refinement yields negligible improvement, which indicates that the solution converges.

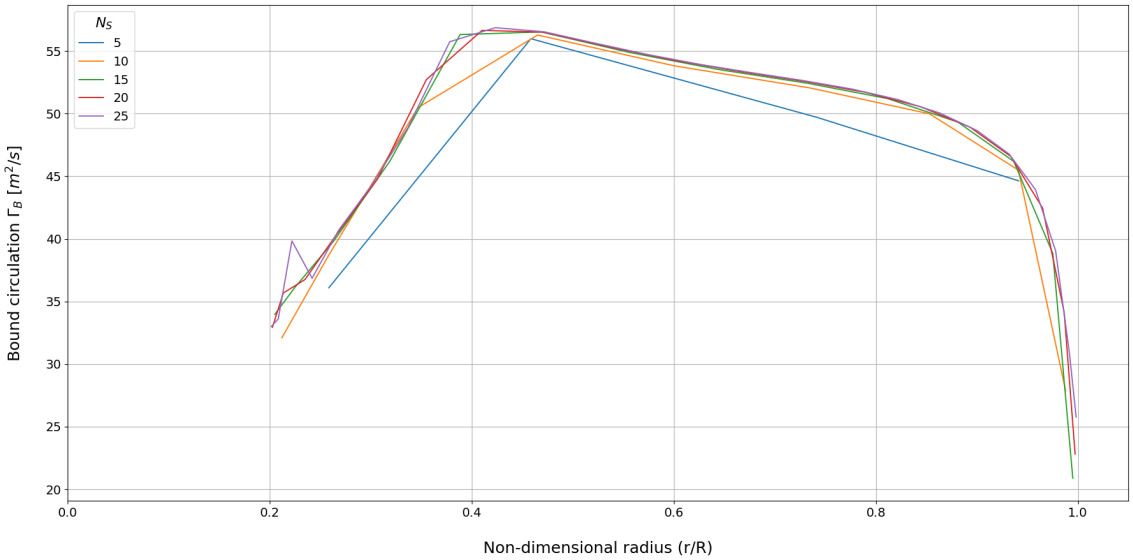

Figure 11.4: Distribution of bound circulation for different values of spanwise blade elements. Where the coarse grid is defined by $N_S = 5$ and the finest grid by $N_S = 25$

A second important indicator of the sensitivity is the trajectory of the tip vortex. As the tip vortex represents the strongest change of bound circulation, it is directly linked to the spatial resolution. For low number of blade segments, the trailing vortices are further apart and of higher magnitude. This effects the numerical accuracy of modeling the tip vortex roll-up behavior, as well as the wake shape. With a more refined mesh, this phenomenon can be simulated in a smoother way, contributing to improved numerical stability. The effect is illustrated in Figure 11.5, which represents the wake topology of the coarse ($N_S = 5$) and fine ($N_S = 25$) resolution. The vortices of the coarse grid remain more coherent over longer distances, resulting in a less distorted wake flow in the far field. In contrast, the finer discretisation produces a denser system of smaller vortices that roll-up earlier in the domain.

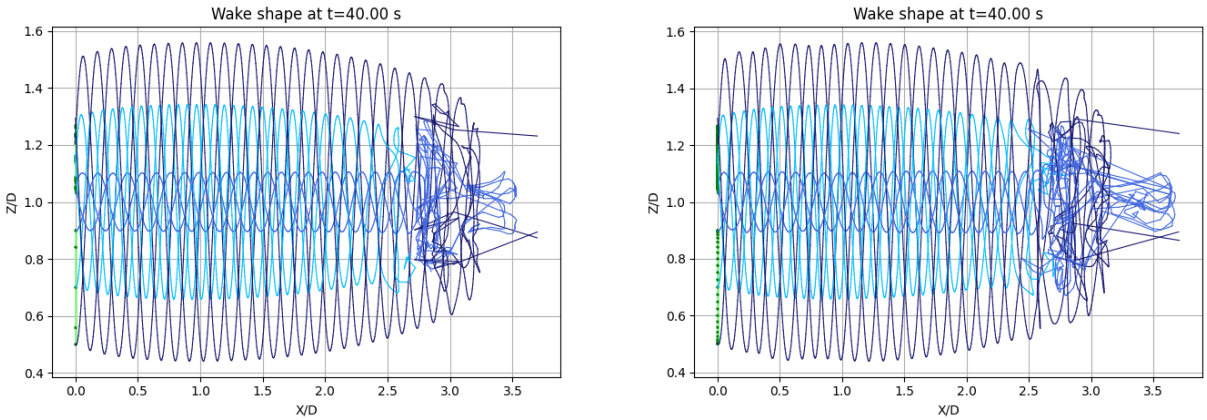

Figure 11.5: Side view of the wake shape for the sensitivity analysis on spatial resolution. Where the left figure shows the coarse grid ($N_S = 5$) and the right figure shows the finest mesh ($N_S = 25$)

The effect of the spatial resolution on the wake field is further demonstrated in Figure 11.6, showing the axial velocity distribution along the rotor's centerline. For a very low number of blade elements ($N_S = 5$), the wake is insufficiently represented. The velocity deficit is smoother and less pronounced than for a more refined mesh. This leads to an underestimation of the minimum axial velocity as well as an overall delayed flow recovery. Physically, this behavior is mainly caused by an inaccurate representation of the trailing vortices at the tip. As previously mentioned, these are the strongest vortices and drive flow phenomena such as vortex roll-up. As the segment count increases, the model is able to capture the flow behavior more accurately. The velocity deficit is larger and the point at which flow recovery occurs shifts towards the rotor. For values above $N_S = 15$, the axial velocity distribution appears to remain unchanged. This indicates the simulation is converging, in line with previous findings in the distribution of bound circulation. From this point onwards, the flow properties and key entrainment mechanism are accurately represented by the model.

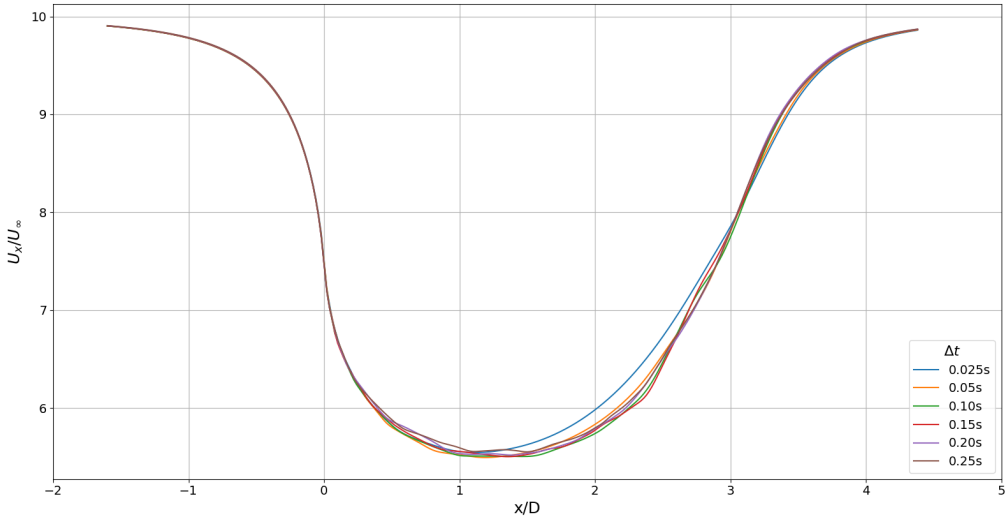

Figure 11.6: Rotor-averaged, axial velocity on the rotor-axis for different spatial resolutions, reflected by the number of spanwise blade elements (N_S)

To quantify the relationship between numerical accuracy and computational efficiency, the relative metrics are presented in Table 11.6. The first row shows the relative decrease in computational time, while the other rows present the corresponding accuracy at different radial positions. Here, all values are measured with respect to the finest discretisation ($N_S = 25$). It should be noted that the optimum is highly dependent on the blade design, as more complex shapes require a finer mesh. For this sensitivity analysis, the blade is modeled with a constant airfoil type and linear relations of the chord and twist angle with respect to the radial position. Therefore, a spanwise blade discretisation of 15 segments shows acceptable runtime, for only a minor loss in accuracy.

Table 11.6: Summary of the sensitivity analysis of the number spanwise blade segments (N_S). Metrics are relative to the finest discretisation ($N_S = 25$).

Result	N_S=5	N_S=10	N_S=15	N_S=20	N_S=25
Total runtime [h]	0.47	2.6	5.5	10.9	35.4
% Relative runtime	1.3	7.3	15.5	30.8	100
% Relative error Γ_B ($\hat{r}$=0.2)	12	-1.8	2.7	-0.9	0.0
% Relative error Γ_B ($\hat{r}$=0.4)	-2.3	-4.9	-0.5	0.3	0.0
% Relative error Γ_B ($\hat{r}$=0.8	-4.6	-1.3	-0.7	-0.4	0.0
% Relative error Γ_B ($\hat{r}$=1.0)	73	5.8	-19	-9.6	0.0

Temporal resolution

The model relies on a time-marching integration method to approximate vortex movement, via convection of Lagrangian makers (Eq. 10.16). This numerical technique is used to solve unsteady functions through iteratively computing the solution at discrete points in time. Here, the time step size controls the temporal resolution of the simulation. The smaller the step size, the better the modeling accuracy of the dynamic motion of the flow. Conversely, large time steps can lead to aliasing, whereby the physical evolution of the flow cannot be represented anymore by the model. For most time integration methods, like the FE-method, it can improve numerical stability as well. However, very small time steps may worsen the stability, as a result of accumulation of numerical errors, in particular regarding round-off.

The influence of the temporal resolution on the aerodynamic blade loading is first illustrated in Figure 11.7, showing the distribution of bound circulation for different time steps. At a very coarse resolution, large Δt, the blade aerodynamics appears to be insufficiently resolved, which results in an inaccurate representation of the spanwise variation. While the effect is most evident at the root, it is observable across the entire distribution. As the time step size decreases, the rotational motion of the blade is better captured, leading to a more realistic spanwise variation. Starting from $\Delta t = 0.15s$, the sensitivity tends to decrease at smaller time steps, which suggests a possible convergence.

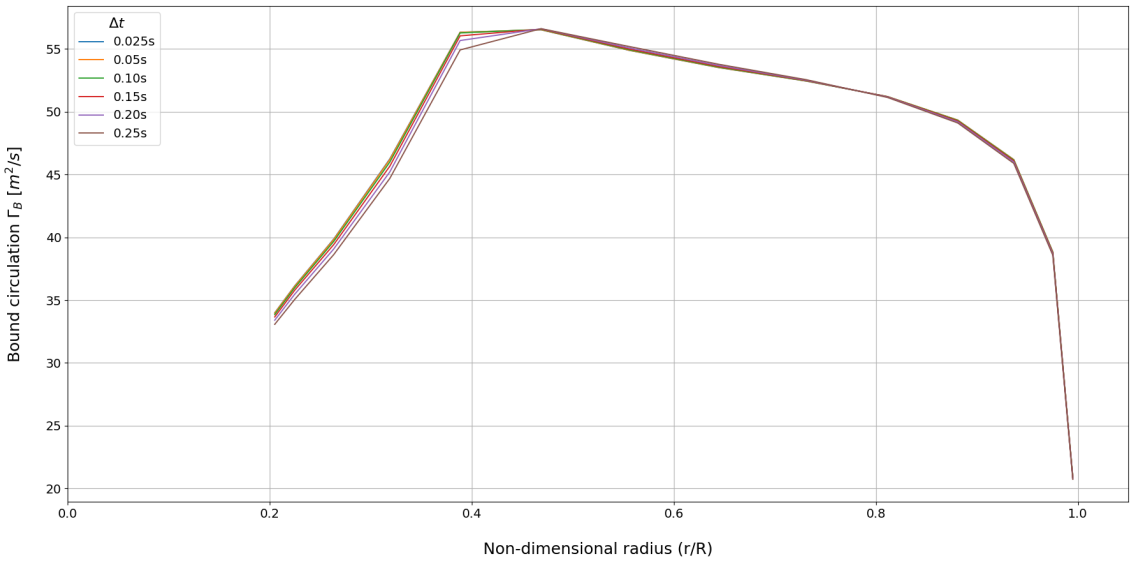

Figure 11.7: Distribution of bound circulation for different values of time step sizes. Where the coarse temporal mesh is defined by $\Delta t = 0.25s$ / $\Delta\phi = 23°$ and the finest by $\Delta t = 0.025s$ / $\Delta\phi = 2.3°$

A more detailed look of the impact of the temporal resolution on the wake flow field is provided in Figure 11.8, where the axial velocity distribution is shown along the centerline of the rotor. For large

time steps, the wake flow field appears to be unstable, already rather quickly behind the rotor. Here, the rotor model makes relatively large azimuthal jumps of $23°$ between consecutive time steps. As the helical pattern cannot be tracked, it results in an irregular separation of vortex elements. The resulting velocity field is ill-structured and the induced velocities fluctuate considerably. At smaller time steps, or equivalent smaller azimuthal jumps, the wake geometry becomes smoother and more consistent vortex trajectory. The improved resolution decreases the vortex spacing, resulting in a higher numerical stability as well as an acceleration of the flow recovery process driven by vortex roll-up. It can be observed that the induced velocity field appears to converge towards a stable configuration at $\Delta t = 0.05s$. An even smaller time step from this point shows to deviate significantly from all other simulations. This is possibly a result of accumulation of the numerical round-off errors from the induced velocity calculations.

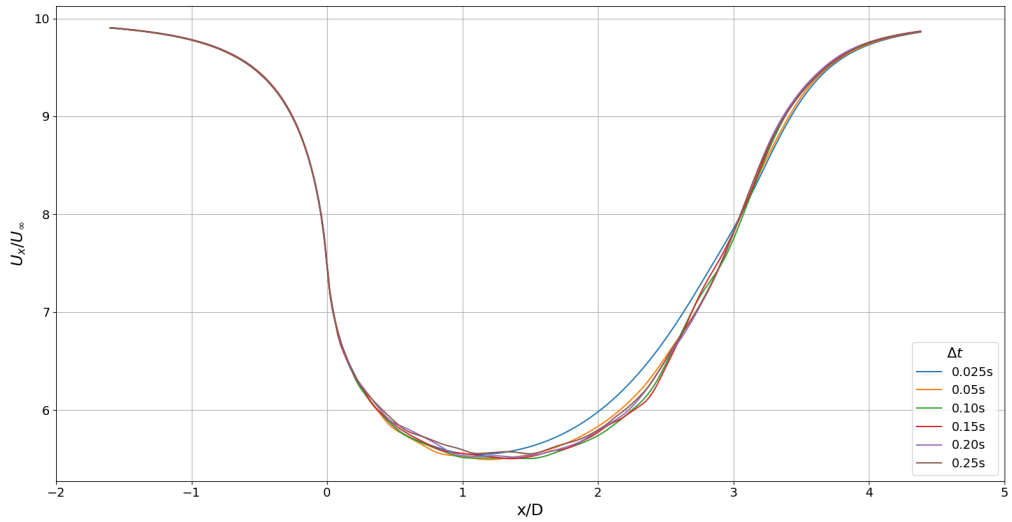

Figure 11.8: Rotor-averaged, axial velocity on the rotor-axis for different temporal resolutions, reflected by time step size

Lastly, in Figure 11.9, the resulting wake geometry is compared for the crudest ($\Delta t = 0.25s$) and finest ($\Delta t = 0.025s$) temporal resolutions. As mentioned, the step size is directly related to the azimuthal discretisation of the rotor revolution. For large time steps, the rotor makes quick angular jumps. This results in strong shed vortices, especially at initialization. The modeled wake is sparse and not completely represented. The wake roll-up behavior is noticeable, but the trajectory is inaccurate as the rate is off. As the wake convects downstream, the vortices start to fade out and the errors are less prominent. However, as the induced-velocity effects are most significant in the near wake, a coarse temporal resolution also affects the flow field. In order to quantify this hypothesis, the effect of the step size on the axial velocity deficit is illustrated in Figure 11.8. It should be noted that this quantity is rotor-averaged, as previously explained in Section 10.3. Here it is apparent that the smaller, accelerated tip vortex roll-up at short time steps provide a better approximation of the wake flow recovery.

To find the optimum balance between computational cost and numerical accuracy, a quantitative comparison is provided in Table 11.7. The costs are indicated by the relative runtime, while the accuracy is measured by the respective error of the velocity deficit. Both quantities are taken relative to the finest discretisation, $\Delta t = 0.025s$. From the resulting data, the strong effect of the time step size on the computational time can be obtained. For increasingly smaller time steps, the numerical results become more accurate. However, at some point, the modeling improvements no longer outweigh the extreme up-shift in simulation time. From this, it can be concluded that a moderate time step of $\Delta t = 0.05s$ is sufficient for this application, maintaining the efficiency-accuracy balance.

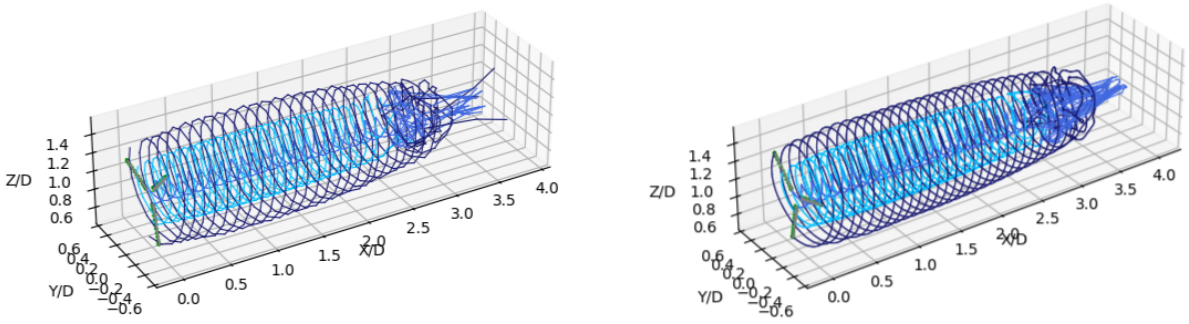

Figure 11.9: 3D wake geometry for the sensitivity analysis on temporal resolution. Where the left figure shows the largest step size ($\Delta t = 0.25s$ / $\Delta\phi = 23°$) and the right figure shows the smallest ($\Delta t = 0.025s$ / $\Delta\phi = 2.3°$)

Table 11.7: Summary of the sensitivity analysis of the time step size in seconds (Δt). Metrics are relative to the finest discretisation ($\Delta t = 0.05$).

Result	Δt=0.25	Δt=0.20	Δt=0.15	Δt=0.10	Δt=0.05	Δt=0.025
Total runtime [h]	0.04	0.11	0.27	0.86	5.5	94.5
% Relative runtime	0.04	0.12	0.29	0.9	5.8	100
% Relative error δ_U ($\hat{x}_R$=0)	-0.51	-0.42	-0.35	-0.25	0.11	0.0
% Relative error δ_U ($\hat{x}_R$=2)	1.0	-0.5	0.1	-0.8	-0.6	0.0
% Relative error δ_U ($\hat{x}_R$=4)	-2.9	-3.3	-3.5	-4.1	-2.3	0.0

For all time step values, the simulation results exhibited instability towards the end of the domain. This effect was further investigated, to find out whether this can be solved with an even small time step. In a numerical stability analysis of Gupta and Leishman, the FE scheme showed unstable behavior independent of the step size [110]. Therefore, future work should use a modified version of the FE: the predictor-corrector scheme (PC). This implicit approach computes the time integral by a combination of guessed value and revision, as shown in Eq. 11.13. First, the solution will be guessed using an explicit approach, which is in this case the FE. The velocity at this new evaluation point will be computed for the following timestep and averaged out with the current timestep, to obtain the corrected solution. This results in a more precise and stable approximation of the time integral, with only a slight increase of the computational cost.

$$\vec{x}_{t+1_{PC}} = \vec{x}_t + [2\vec{u}_\infty + \vec{q}_i(\vec{x}_t) + \vec{q}_i(\vec{x}_{t+1_{FE}})]\,\frac{\Delta t}{2} \tag{11.13}$$

Wake length

To specify the time domain of the simulation environment, an additional setting is required for the temporal domain, one that provides the total time of the simulation. This time period can be interpreted as the downstream distance of the starting vortex from the current rotor position, equivalent to the length of the wake. The total simulation time (T_{tot}), defined in seconds, can be converted in rotation angles or rotor revolutions. The wake length setting effectively controls the area over which the induced velocity field is captured. For a longer distance, the downstream wake can be represented more completely. Not only has the wake more time to develop, there are more wake points describing the flow behavior.

The influence of the wake length on the modeling accuracy of the blade aerodynamics can be analyzed from the spanwise distribution of bound circulation, shown in Figure 11.10. Most interestingly, no significant differences can be found for an increasing simulation time. This indicates that the spanwise variation is essentially insensitive to the wake length. Such behavior is consistent with theory, since the induced velocity on the rotor plane is dominated by the vortices in the direct vicinity of the blades. As the contribution

of distant vortices decrease quickly with distance, they have only a negligible effect on the local flow field. Given that the near-wake field converges to quasi-steady state as first, the aerodynamic loading on the blade stabilizes consequently.

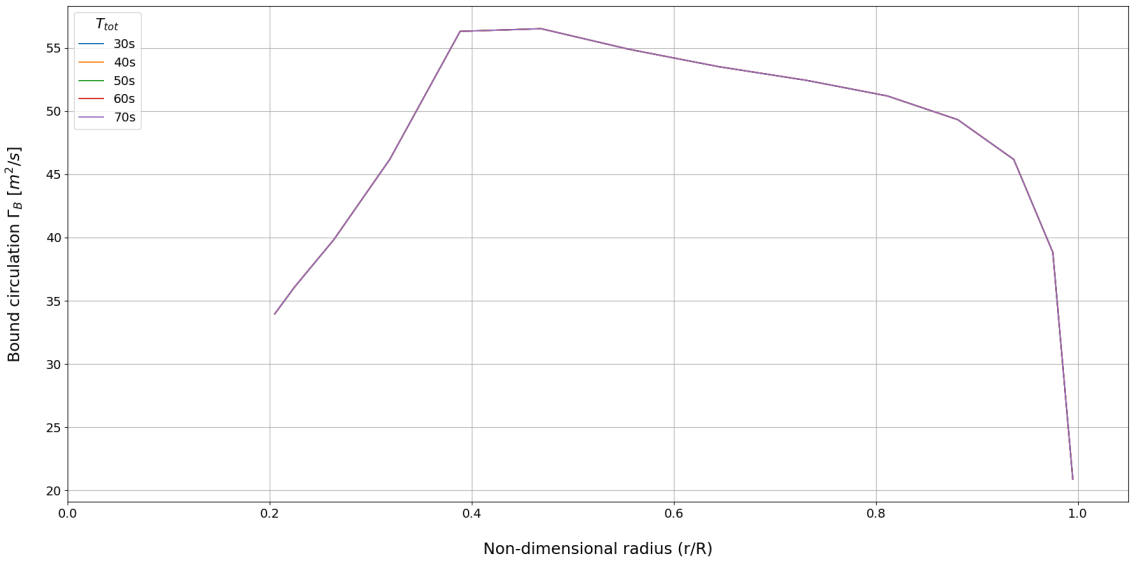

Figure 11.10: Distribution of bound circulation for different values of wake length, reflected by total simulated time

The qualitative influence of the wake length on the flow field can be studied by comparing the wake geometry for the different simulation time periods. In very short simulations, start-up effects like the starting vortex remain close to the rotor plane. This creates an un-physical distortion of severe size on the local velocity field. As the wake is simulated for a longer time period, these initiation effects are propagated downstream and a larger portion of the flow in the wake is represented by the modeled vortex system. The geometry in the near-wake slowly stabilizes and shows a more coherent, gradual roll-up pattern. At the longest simulation time, the near-wake is largely converged, while the flow close to the end of the domain shows to be irregular and chaotic behavior. This indicates that the modeled near wake approaches a stable geometry, while the far-wake is still in evolution.

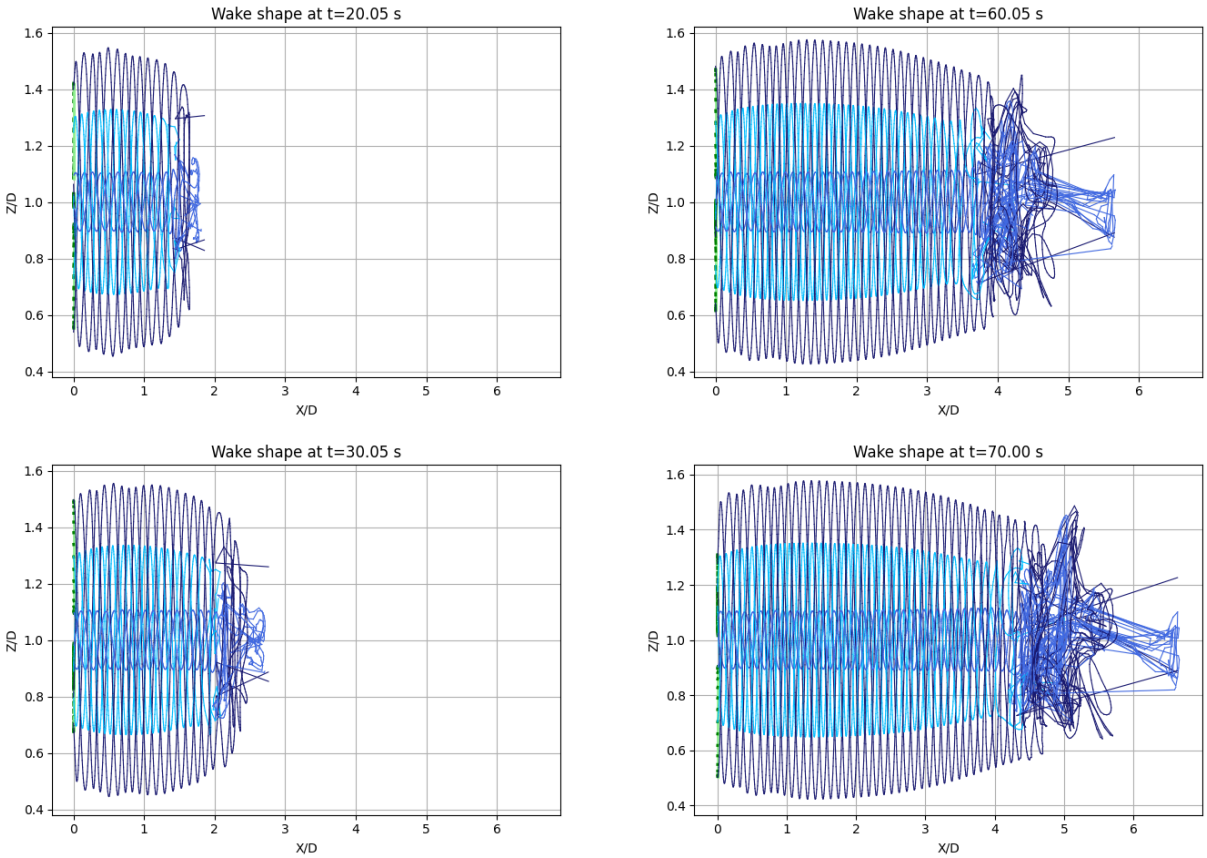

Figure 11.11: Side view of the wake shape for the sensitivity analysis on wake length. Total simulation time is shown for $t = 20, 30, 60, 70s$

With Figure 11.12, the effect on the wake flow field can be reasoned quantitatively in terms of the axial velocity deficit along the rotor axis of rotation. For a low simulation time, only a short portion of the wake is modeled. This results in an unrealistically quick recovery of the axial velocity, due to a lack of contributions. As the wake length increases, a larger share of the physical wake is captured by the model. The location of the flow instability shifts further downstream, as the initial flow disturbances gradually move with the simulation boundary. Concurrently, the flow region close to the rotor disk continues to develop as the simulation time increases. The maximum velocity deficit intensifies and occurs further downstream, mirroring a more realistic build-up of the locally induced flow field. Strikingly, while the minimum axial velocity and its position change substantially, the rate of flow recovery appears to remain fairly consistent in all cases. This observation suggests that the near-wake field is close to its quasi-steady state. On the contrary, the flow field in the far-wake shows no convergence yet, within the current maximum simulated time of $t = 70s$. As a result, the flow field in the far-wake continues to evolve and a longer duration is required to simulate a converged solution at this region.

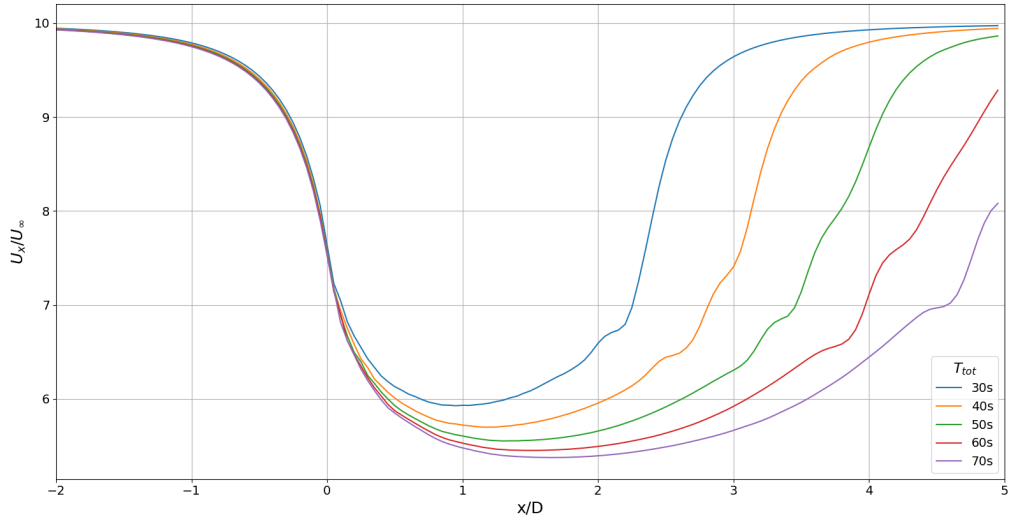

Figure 11.12: Rotor-averaged, axial velocity deficit on the rotor-axis for the different wake lengths, reflected by simulated time

Table 11.8: Summary of the sensitivity analysis of the total simulation time in seconds (T_{tot}). Metrics are relative to the longest wake ($T_{tot} = 70$).

Result	T_{tot}=30	T_{tot}=40	T_{tot}=50	T_{tot}=60	T_{tot}=70
Rotor revolutions ($nRev$)	7.6	10	12.7	15.3	17.8
Total runtime [h]	2.4	5.5	13.4	28.7	41.1
% Relative runtime	5.84	13.4	32.6	69.8	100
% Relative error δ_U ($\hat{x}_R$=0)	2.0	1.1	0.8	0.5	0.0
% Relative error δ_U ($\hat{x}_R$=2)	8.3	4.4	2.3	1.0	0.0
% Relative error δ_U ($\hat{x}_R$=4)	22.4	10.4	4.9	1.8	0.0

Aerodynamic loading

In practice, wind turbine rarely operate under the perfect flow conditions for which they were designed. Here, one can think of intentional axial induction control, turbulence in the ambient flow, or delays in the response of control systems. These can cause the rotor to operate in sub-optimal aerodynamic conditions. In order to profile these conditional effects, a sensitivity analysis will be conducted on turbine loading. Within the K-TWIST framework, this can be implemented as a global pitch angle on all rotor blades. The offset on the blade pitch angle effectively alters the local angle of attack, which changes the lift generation and spanwise distribution of aerodynamic loads. With the conventions defined in Figure 10.10, a positive pitch angle leads to a blade rotation out of the flow, known as *pitch to feather*. The effect of a negative pitch angle is the exact opposite and is commonly referred as *pitch to stall*. Although this setting is not a direct control input parameter, it provides a useful indication of the model's capability to reproduce rotor performance characteristics under sub-optimal conditions.

The effect of the blade pitch setting on the aerodynamic loading is analyzed with Figure 11.13, presenting the spanwise variation of bound circulation. Here, the benchmark case corresponds to a blade pitch setting of $-2°$. It shows a nearly constant distribution along the most of the blade span, with a magnitude of approximately $55\,m^2/s$. The shape indicates a well-balanced spanwise variation of the aerodynamic forces with strong tip vortices, as expected for a rotor operating around the conditions it is designed in. When the global pitch angle is increased with a $5°$ *pitch to stall* setting, the shape of the circulation curve clearly

transforms into an elliptical-like form. The peak in vortex strength shifts towards the tip region and hits a notably higher maximum value at $65\ m^2/s$. This effect can be explained with the relation between blade pitch angle and inflow angle in Figure 10.10. As the tangential velocity increases with radius, the inflow becomes more aligned with the chord line due to rotational speed. Given that the pitch setting is globally applied and the blade is represented with a constant airfoil type, it creates a constant offset of the effective angle of attack. Whereas the mid- and outer part of the blade show to move towards the stall angle, the inboard region was already near this optimum and has now move past it, reducing the contribution towards the lift generation. While an elliptical distribution of bound circulation is known for minimum induced losses, it is in this case the result of partial unloading of the inner blade section rather than an optimized design configuration. Conversely, when the rotor blades are pitched in the opposite direction with a $5°$ *pitch to feather*, the distribution becomes more bell-shapes. The magnitude of circulation is reduced across the entire span and the maximum value of $40\ m^2/s$ is now located close to the blade root. The larger pitch angle reduces the effective angle of attack, which decreases lift on all blade sections. As the airfoil moves away from its optimal point, the resulting distribution corresponds to a lower thrust and induction factor. The overall shape is very similar to the distribution of Figure A.8, which suggests the pitch setting approaches the behavior of a constant loading rotor.

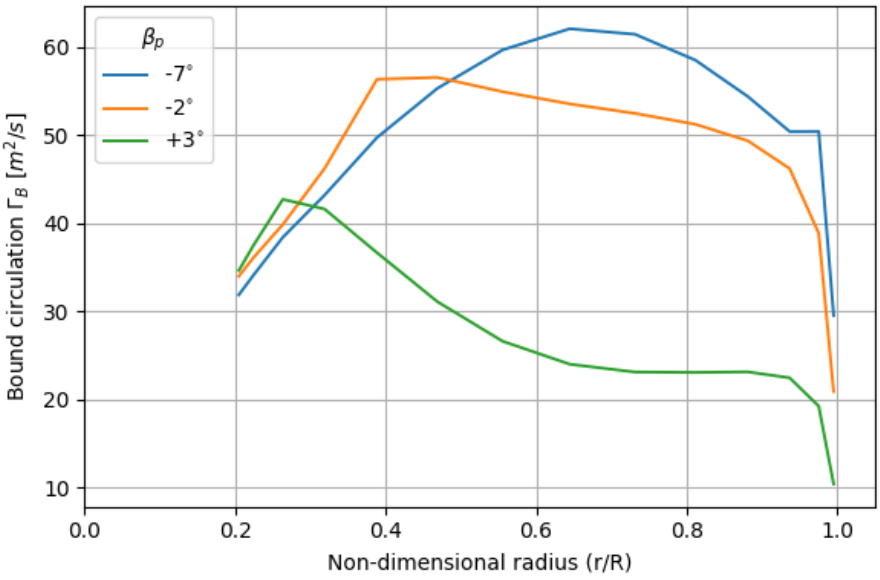

Figure 11.13: Distribution of bound circulation for different aerodynamic conditions, reflected by blade pitch angle (β_p)

Complementary effects can be observed in the wake velocity field. To illustrate this, the axial velocity distribution along the rotor's centerline is presented in Figure 11.14. Proceeding from the reference case of $\beta_p = -2°$, a decrease in pitch angle causes a slight increase in the velocity deficit around the rotor. This corresponds to the additional induced velocities and greater extraction of momentum from a higher thrust setting. The stronger induction also causes the deficit to sustain further downstream before recovering. This can be observed in the figure from the lagging velocity increase, while the recovery speed itself remains similar to the initial setting. However, an increase in the pitch angle does not have the exact opposite effect. The axial velocity throughout the entire domain is significantly higher, reflecting a weaker turbine. In addition, the relative recovery rate appears to be smaller than in the other cases. This makes sense, since the lower momentum extraction creates a weaker system of wake vortices. In the K-TWIST model, these vortices are the main driver of the induced velocity field. As the weaker wake creates less self-induction, there is less interaction between the vortices and thereby less recovery.

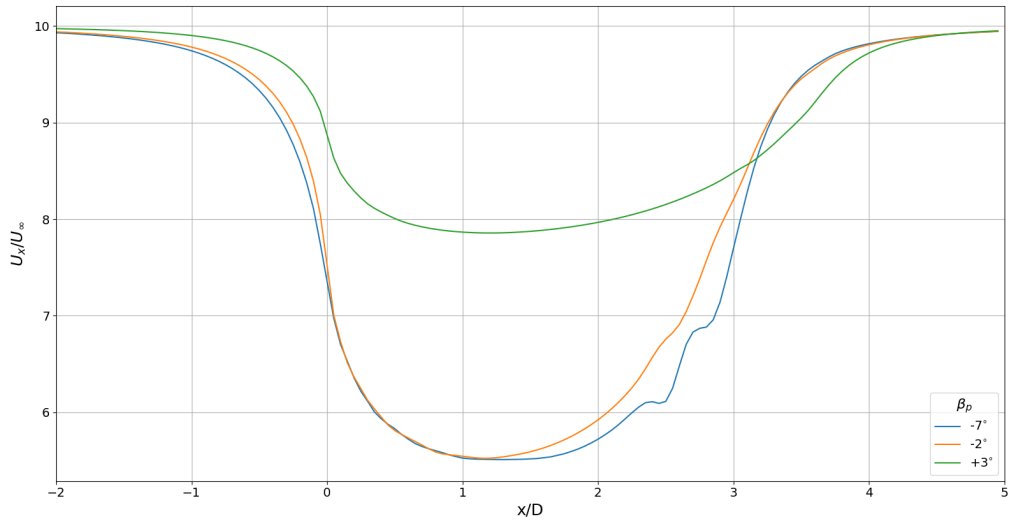

Figure 11.14: Rotor-averaged, axial velocity deficit on the rotor-axis for different aerodynamic conditions, reflected by blade pitch angle (β_p)

Hardware conditions

As previously discussed in Section 10.2.5, the model is programmed to run on multiple CPU cores in parallel. The number of cores does not change the numerical accuracy, but is does affect the computational efficiency. To chart the relationship between the number of processors and the computational time, the exact same simulation will be executed with different core numbers. This allows for the identification of an efficient hardware setup, minimizing computational time while maintaining low energy cost.

The simulation is performed five times, with the number of CPU cores increased in increments of four. Given the scope of the simulation conditions, it was decided to start the study with four cores. Since there is a non-linear correlation between the core count and the numerical time, simulating on a single core will take substantially longer to run. The maximum number of cores is capped at twenty due to the restrictions of the HPC12 cluster.

In Figure 11.15, the evolution of the delta time per simulation step is plotted. As expected, the lower number of CPU cores drastically extends the overall runtime. For the case of 20 cores, the simulation was completed after approximately 3 hours, while the 4 cores required almost 19 hours. This corresponds to more than a sixfold difference, highlighting the significant benefits of parallel computation. From the graph, a few trends can be obtained for all core numbers. At the start of the simulation, the delta time is low as a consequence of low workloads. As the simulation advances, the workload of the FVW model increases leading to a upward slope of the incremental delta time. Additionally, both small and large fluctuations are found, which are most pronounced in the lowest core number. The small oscillations are mainly caused by the un parallelized parts of the K-TWIST model, such as the iterative procedure of the distribution of bound circulation. The larger fluctuations, on the other hand, are rather caused by the hardware than the model itself. Parallel computation with Numba JIT-compiler [103] effectively converts python code into machine code to run at faster speed. However, this parallel computation required managing cost like thread startup cost, task splitting and scheduling. In addition, due to the higher workload per core, other phenomena start to play a role, such as cache fitting, memory bandwidth and SIMD utilization [111].

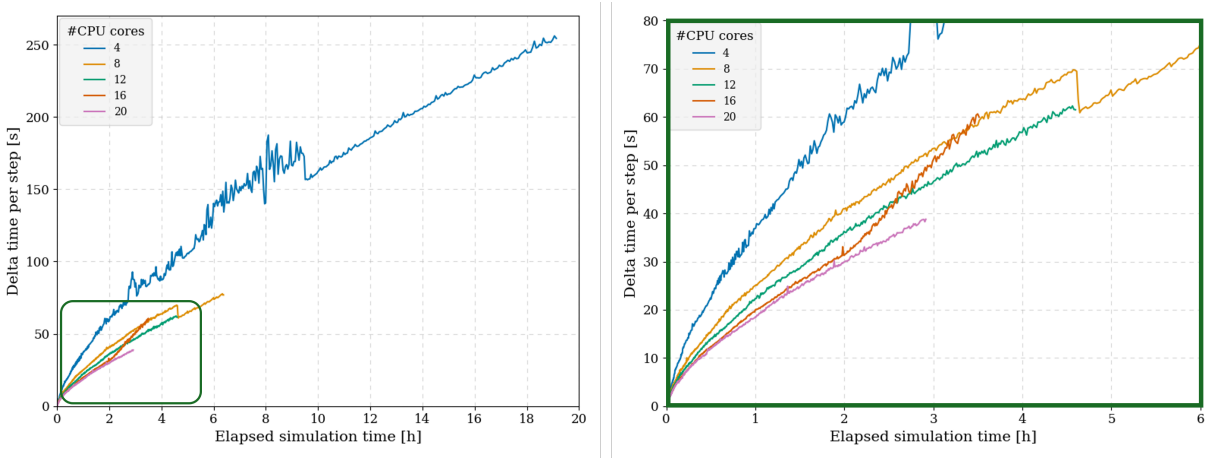

Figure 11.15: Execution time required for each numerical time step. Left: full time series. Right: detailed-view of the marked region in green.

Focusing on the individual trends of the number of CPU cores reveal supplementary behavior. In Figure 11.15, the 4-core trend showed particularly large oscillations between a time-window of 3 to 10 hours. Given that the simulation is run on a shared HPC node of 20 cores, it it likely that there was an additional large-scale consumer on the same node during this time frame. As the FVW-based model is not only influenced by the computational power but by the memory capacity as well, this can significantly alter the simulation time. For the higher number of cores, the trends are better visible in the zoomed-in green box on the right-hand-side of the figure. For the 8-core case, a noticeable drop can be obtained around 4.5 hours, exactly when the 12-core trend ends. This suggests that the 8-core and 12-core runs were allocated on the same HPC node, resulting in resource availability effects. While the 20-core simulation was relatively consistent, a rapid climb can be seen in the 16-core trend, again probably linked to memory limitations of the shared-node system of the HPC12. Since this cannot be disabled, the effect can only be investigated further by repeated execution in future work.

Since the number of elements grows with every time step for the K-TWIST model, the time evolution of the workload is dependent on the core count. As seen in Figure A.10, these create the different slopes in the delta time plot of Figure 11.15. In order to better compare the impact of the number of cores, both axis should be normalized. For the horizontal axis, the elapsed time, can be converted into time step count. On the other hand, the vertical axis, the delta time can be divided by the workload to achieve a per-element step time. The normalized curves on the left of Figure 11.16 reveal new insights. Extreme initial spikes, caused by simulation startup costs for all core numbers. At a step count of 50, all trends show a huge drop, caused by the algorithm build in the K-TWIST model. Where the simulation first runs on a single core and only starts parallel computation when it hits a certain workload cap, which appears to be at 50 time steps deep. As it is expected that all simulations have the same behavior in this region, it is interesting to see that the 4-CPU case significantly deviates from the others. For all core numbers, the trends seems to converge to a constant value of *0.101, 0.031, 0.025, 0.018*, and *0.016*, from low-to-high core count.

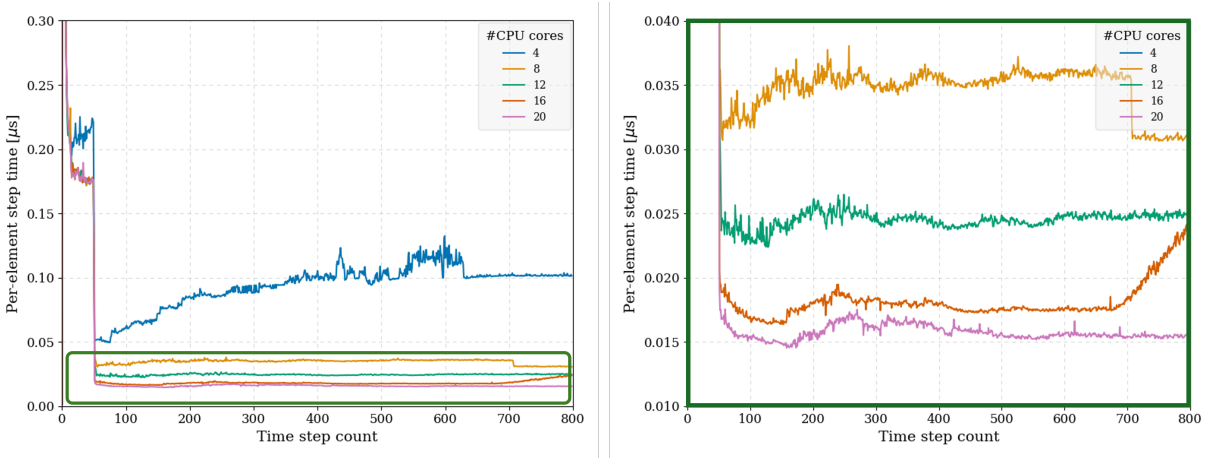

Figure 11.16: Computational cost per element as a function of the time step count. Left: Full cost scale (y-axis). Right: Detailed-view of the marker region in green

For the lowest core number, the 4CPU, the normalized plot shows an upwards trends that gradually reaches an asymptote around $0.1\mu s$, while the others appear consistent from the start. However, this behavior can be obtained for all other core number as well, by zooming in on the lower part of the graph, presented on the right of Figure 11.16. Here again, the drop of 8CPU and the rapid climbs of 16CPU around a step count of 700 are clearly visible. In addition, there appears to be another effect of the core count on the per-element step time. The normalized trend of the higher core numbers goes down at first, then goes up to a maximum and decreases again to hit a constant value at the end of simulation time. Given that the workload is a continuous rise, as shown in Figure A.10, there has to be another factor of influence. As both the minimum and the maximum are later on in the simulation for higher core numbers, it is likely that this is the result of overhead costs. For a high number of parallel threads, the same information needs to be managed across more workers. At the lowest value point, there is an optimal balance between workload and overhead costs. Due to the non-linear evolution of the workload, the impact of the task size starts to take over. After reaching a maximum where all factors align, the impact of overhead costs are masked by the workload and the parallel computation reaches its peak efficiency. The convergence behavior indicates that the workload of this sensitivity analysis has not reached the memory limit of the HPC node, as this would show as a decline in the delta time per-element.

The individual plots of Figure 11.15 can be combined into one single graph of the core count vs the simulation time (Figure 11.17). It seems that the improvement in total clock-time for an increased number of cores fall off, which points to a possible optimal computational efficiency. To further map out this hypothesis, the core count is plotted against the relative speed-up. In figure Figure 11.18, the speed-up is taken with respect to the 4-CPU case. The Grey line indicates linear correlation, which means that doubling core number leads to halving the simulation time. The relative speed-up shows superlinear behavior, where the acceleration is higher than the number of added processors. This phenomenon is commonly found in both parallel computation and virtual HPC environments, as a consequence of resource allocation, specifically cache and memory [112]. When the relative speed-up is plotted with respect to a higher core number, like in Figure A.11 for the 8-CPU case, the more expected, correlation can be obtained. The linear relation is, however, sublinear due to the theoretical limit of the model's serial portion, known in computer science as *Amdhal's law*. At a certain point, the additional overhead cost from added cores eventually exceed the advanced processing power and the total simulation time increases. This phenomenon of *parallel slowdown* is not visible in the relative speed-up curve in Figure A.11, which means that the optimal point cannot yet be determined. Solely based on this sensitivity analysis, the highest computational efficiency can be obtained at the maximum number of cores. A summary of all the results from the sensitivity analysis on the number of CPU cores is presented in Table 11.9.

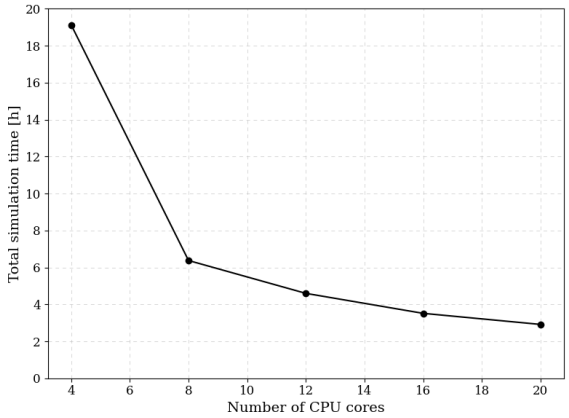

Figure 11.17: Total simulation runtime as a function of the number of CPU cores in parallel computing

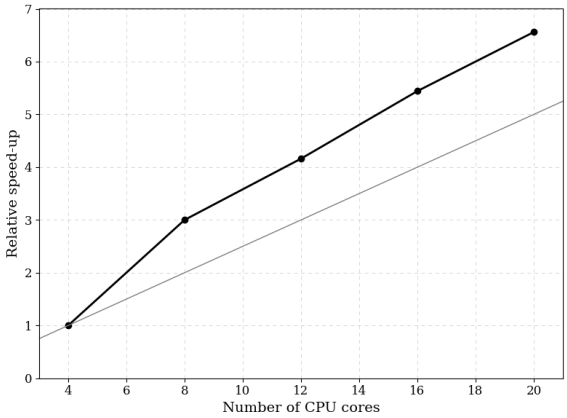

Figure 11.18: Parallel efficiency expressed as relative speedup versus number of CPU cores, with respect to the 4-CPU runtime

Table 11.9: Summary of the sensitivity analysis of the number of parallel computing cores (N_{CPU})

Result	4 CPU	8 CPU	12 CPU	16 CPU	20 CPU	Figure
Per-element step time [μs]	0.101	0.031	0.025	0.018	0.016	11.16
Total simulation time [h]	19.1	6.4	4.6	3.5	2.9	11.17
Relative speed-up (4 CPU)	1.0	3.0	4.2	5.4	6.5	11.18
Relative speed-up (8 CPU)	0.3	1.0	1.4	1.8	2.2	A.11

11.2. Validation

For this study, no extensive validation procedure of the LL-FW method will be conducted. The theoretical framework and physical accuracy have already been validated thoroughly in literature [113]–[115]. For the specific nonlinear lift correction, van Garrel demonstrated the method's capability to predict unsteady dynamics of wake flow, with reasonable matches against experimental data for a wide range of configurations [116]. Of his highly extensive validation research, the rotor aerodynamic characteristics and the three-dimensional flow field in the wake are of particular interest for the current study. With regard to the first one, the turbine performance of the *NREL Phase VI* was simulated for below stall conditions. The result of Figure A.12 demonstrate that the model corresponds very well with the experiments from the wind tunnel. Regarding the validation of the wake flow field, the induced velocity in the external field was computed from the simulation results and compared with PIV measurements from the *EU FP5 project MEXICO*. The results show that both the radial distribution behind the rotor (Figure A.13) and on the rotor axis (Figure A.14) closely match with the measured axial velocity profiles.

As a result, the emphasis of this research is not on re-validation, but rather on verifying the numerical behavior of the specific implementation developed in the K-TWIST model. These practices serve as a foundation for the model's application in the subsequent case studies of the kite-turbine interaction.

12

Kite-Turbine Wake Interaction

For this research, a qualitative case study is conducted using the K-TWIST model to study the effect of kite placement in between two consecutive wind turbines on the overall wind farm efficiency. The case study is performed in three separate steps, using the unsteady C_L-based iteration technique for the bound circulation. All simulations are conducted under idealized, steady flow conditions, as presented in Table 12.1. This operating environment is based on a CFD reference study on the atmospheric boundary layer of a wind turbine array [9]. At first, the wind turbine is simulated in a stand-alone environment. The resulting wake development in the operating flow conditions can be used as a reference benchmark. Subsequently, a kite will be added to the simulation domain above the downstream wake of the wind turbine. Since the aerodynamic loads are computed for each timestep, introducing the kite into the turbine's vicinity alters the lift distribution across the rotor blade and may cause asymmetry. Furthermore, a comparison between the kite- and the baseline scenarios can be utilized to identify the kite-induced effects on key characteristics of the wake flow, such as its structure, strength and recovery rate. In other words, the case study reflects the feasibility to analyze the kite's influence on both the turbine loading and the wake dynamics. At last, a simplified analysis will be performed on the influence of the kite's wing span on wake recovery. This will demonstrate the capability of the model to parametric studies, in order to find a potential optimal configuration.

Table 12.1: Simulation conditions for the qualitative study on kite-turbine wake interaction, using the K-TWIST model

Case variable	Symbol	Setting	Unit
Free-stream velocity	$U_{x,\infty}$	8.5	m/s
Turbulence intensity	TI_∞	0.0	%
Flow density	ρ	1.225	kg/m^3
Kinematic viscosity	ν	1.48E-5	m^2/s

12.1. Simulation of 2MW wind turbine

In order to study the impact of kites on the wake recovery of a wind turbine, the rotor needs to be simulated in isolation at first. The simulated wake field will be used as a baseline for comparison of the kite-turbine interaction in the second part (Section 12.2). The simulation will be performed under steady, uniform inflow conditions for a scaled version of the *NREL-5MW* wind turbine [117]. This turbine was chosen because of the detailed and readily available data, in contrast to commercial 2 MW wind turbines such as the *Vestas V80-2MW* used in the CFD reference studies.

12.1.1. Turbine set-up

The NREL wind turbine is down sized to a comparable 2 MW version using scaling laws, to remain consistent with previous work on the topic. The scaling laws are derived from dimensional analysis and the principle of similarity. Specifically for wind turbine modeling, it is important to keep the geometry, kinematics and dynamics analogous to the reference turbine. The scaling factor (Λ) is based on the relative

rated power, as shown in Eq. 12.1. Given that the coefficient of power is constant, to ensure dynamic similarity, the rotor swept area needs to be adjusted. In the same way, geometric similarity causes the chord length distribution to scale accordingly. For kinematic resemblance, the rotor speed is tuned to match a consistent tip speed ratio (Eq. 11.6). Both the twist distribution and global pitch angle of the blade remain constant. A complete overview of the applied turbine parameter scaling is presented in Table 12.2

$$\Lambda = \frac{P}{P_{ref}} \tag{12.1}$$

Table 12.2: Parameter scaling of 5MW wind turbine to 2MW

Turbine parameter	Symbol	Scaling	Value
Turbine rated power	P_R	Λ	0.40
Rotor radius	R	$\sqrt{\Lambda}$	0.63
Rated rotor speed	Ω_R	$1/\sqrt{\Lambda}$	1.58
Chord length	c	$\sqrt{\Lambda}$	0.63
Section twist angle	β_t	–	1.00
Blade pitch angle	β_p	–	1.00

The rotor blades of the three-bladed *NREL-2MW* wind turbine are modeled from a radial fraction of 0.2 towards the end of the tip, in the positive y-direction. For numerical reasons, the inboard part of the blade is not included in the geometry. Since these blade sections create little to no lift, it will not have a significant effect on the modeled flow dynamics. The lift-generating zone is divided into six portions, each with a different airfoil type in terms of shape and thickness. The blade geometry is visualized in Figure 12.1 as a function of the non-dimensional distance ($\hat{r}_R$) from the root of the blade. The ”DU-” airfoils were developed by the Delft University, specifically for the design of wind turbine blades. The 2D aerodynamic data was corrected for three-dimensional effects by the NREL and the resulting coefficients are presented in Section B.1.2. For the spanwise chord- and twist distribution, the data has been scaled to a 2MW wind turbine, and the corresponding tables can be found in Section B.1.1.

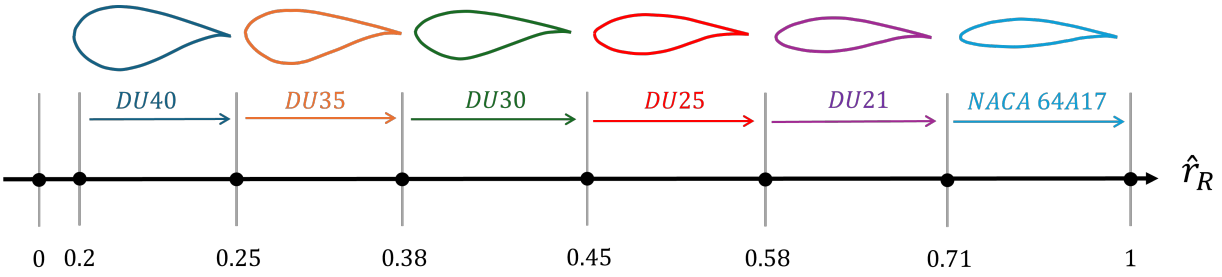

Figure 12.1: Schematic representation of the scaled NREL-5MW model, indicating the blade sections and airfoil types

The performance characteristics of the 2MW wind turbine model are taken directly from the NREL-5MW reference data [117]. These include key design parameters, such as operational wind speed range, optimal tip-speed ratio, rotor orientation and hub location. Given that the inflow conditions are independent of height, the location of the rotor’s center is not scaled from reference data. All numerical simulation settings, including timestep size (Δt), total simulation time (T_{tot}), spanwise blade segments (N_S) and number of CPU cores (N_{CPU}), are selected based on the sensitivity analysis of the verification procedure, as described in Section 11.1.3. The geometric- and simulation parameters that are used as input for the

K-TWIST model are summarized in Table 12.3. The main turbine properties of the scaled NREL-2MW wind turbine model are presented in Table B.1.

Table 12.3: Input parameters for the simulation of the NREL-2MW wind turbine

Geometric variable	Symbol	Setting
Hub location	$(X,Y,Z)_{wt}$	(0,0,90) m
Number of blades	N_B	3
Radial distance	$\hat{r}$	0.2 – 1
Blade radius	R	39.7 m
Blade pitch angle	β_p	0 °

Simulation parameter	Symbol	Setting
CPU core count	N_{CPU}	20
Number of segments	N_S	15
Time step	Δt	0.05 s
Simulation time	T_{tot}	70 s
Rotational speed	Ω	1.5 rad/s

12.1.2. Results of wind turbine simulation

The isolated wind turbine simulation serves as a reference point for evaluating the kite-induced effects on key metrics of wake recovery. In Figure 12.3, the three-dimensional wake geometry is visualized. As expected, the wake vortices follow an helical pattern and the tip vortices start to roll-up around $x/D = 2.5$ downstream. The wake is contracted in the near-wake region and starts to expand again in the far-wake region. These observations become more clear when looking at the side-view of the wake in Figure 12.6. The wake system preserves strong symmetry about the rotor axis of rotation.

At larger downstream distances, towards the end of the computational domain, the vortex filaments become progressively more distorted and loses its helical pattern. The vortex points appear to convect in a more chaotic manner. This behavior is a well-known characteristic of free-wake vortex methods, originating from the numerical challenge to model complex vortex structures with straight filaments over long convection distances. As the wake flow causes an induced effect on itself, small numerical errors start to accumulate to larger deviations and the vortex pattern becomes more unstable. Despite the fact that some of the viscous diffusion is modeled in the time evolution of the core radius, it is only a simple approximation of the natural smoothening that occurs in real turbulent wake. Consequently, the far-wake region in FVM simulations should be for only qualitative measures, while the near- and mid-wake regions provide physically representative approximations of real case scenarios. Therefore, the distant wake is often removed from the filament-based FWM and modeled using other methods, such as the ring vortex. In a subsequent version of the K-TWIST model, a coupled method should be taken into account. This would reduce the number of wake elements in the computationally heavy induced velocity calculation, for a relatively acceptable small loss in numerical accuracy [118].

The distribution of bound circulation along the blade span, Figure 12.8, follows the typical elliptical-like shape, with a maximum point around mid-span and strong dips towards the end points of the blade. At these boundaries, the induced effects are largest, which result in strong trailing vortices close to the tip. This distribution shows that the iterative lift-based solver converges to a pattern that is concurring with wind turbine physics and the induced velocities from the wake flow are reflected in the aerodynamic blade loading. According to the Kutta-Joukowski theorem of Eq. 6.3, this spanwise distribution is directly related to the lift force. As presented in Figure 12.2, the lift distribution follows a shape that is commonly found in wind turbine analysis. The lift per unit span increases gradually along the blade and a falls of quickly near the tip, in line with CFD analysis of the *NREL-5MW* [119].

In the post-processing of the simulation data from the K-TWIST model, the three-dimensional velocity field can be calculated from the combined effects of the wake vortex system. As previously mentioned in Section 10.3, the raw velocity data is applied to several averaging techniques to obtain a smoother, more representative flow field. These are necessary to filter out numerical errors due to blade passing and discretisation techniques. The resulting wake velocity field is plotted in both spanwise and time wise variation. To start off, looking at the radial distribution of the axial velocity deficit at different downstream positions reveal the axisymmetric profile. As seen in Figure 12.10, the velocity profile starts uniform far upstream of the rotor. When the flow approaches the rotor, the flow slows down and quickly reaches a double U-shaped profile. As the center of the rotor ($\hat{r} < 0.2$) is not modeled, the velocity deficit in this region would be nonphysical and is therefore omitted from the plot. Behind the rotor, the velocity deficit

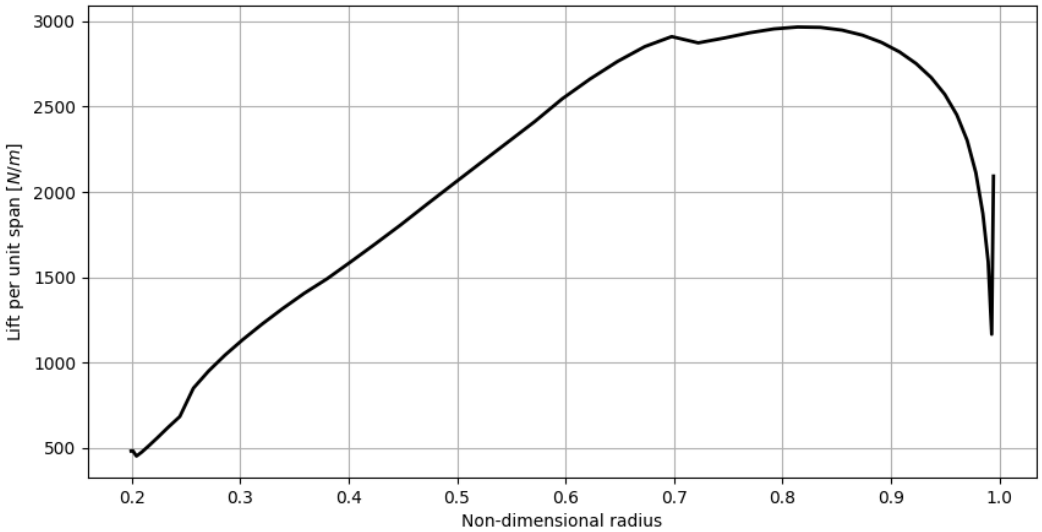

Figure 12.2: Spanwise lift distribution of the NREL-2MW wind turbine in isolation

increases and the flow starts to speeds up at the tips. As the flow moves further downstream, the fluid structures interact with each other and the velocity deficit reduces.

The behavior of the flow in these wake regions are confirmed by the streamwise evolution of the rotor-averaged axial velocity deficit on the centerline. At the rotor plane, an axial velocity of 5.2 m/s can be observed, corresponding to a deficit of 38%. As the flow moves through the rotor downstream, it is slowed down further until it reaches a minimum velocity of 2.8 m/s. This maximum velocity deficit of 67% is reached at approximately 1.5 rotor diameter distance, after which the flow gradually starts to speed up again. It should be noted that the flow behavior from $x/D = 2$ onwards is non-physical. This is the furthest point at which the flow is fully converged to a quasi-steady solution, which indicates that the flow is too close to the simulation boundaries. In order to make meaningful statements about the velocity field at these distances, the simulation must be run over a longer period of time. However, due to the quadratic relation between the simulation time and the number of wake nodes (Eq. 11.12), this will significantly increase the computational costs in the current version of the K-TWIST model.

This statement can be substantiated by examining the mean vertical momentum flux (VMF). Since the inflow conditions are uniform, the flow field is symmetrical with respect to the rotor plane. The upward and downward momentum transport are in equilibrium. Consequently, the vertical momentum flux, averaged over the entire rotor disc, is expected to remain close to constant at zero. It should be noted that this is only valid in the absence of external disturbances or flow asymmetries, such as yaw misalignment or wind shear. For the turbine in isolation case, this metric is presented in Figure 12.11. The VMF remains nearly zero up to approximately two rotor diameters downstream. Beyond this point, small oscillations appear in both VMF and the velocity deficit. This signals that the wake flow is not yet converged to a steady solution. These effects are directly related to the unsteady roll-up and the temporal convergence of the wake filaments. As the flow behavior remains physically consistent until $x/D = 2$ for the isolated turbine case, the resulting velocity field can be considered representative of the wake evolution in the near wake region ($x/D \leq 2$).

12.2. Simulation of kite-turbine interaction

To investigate the influence of an airborne kite system on the downstream wake of the wind turbine, a representative kite model is introduced into the domain of the simulation. This setup allows for direct comparison with the baseline case of the NREL-2MW wind turbine in isolation. The results will be presented side by side to provide insight into its effect on both the blade loading and the wake flow recovery.

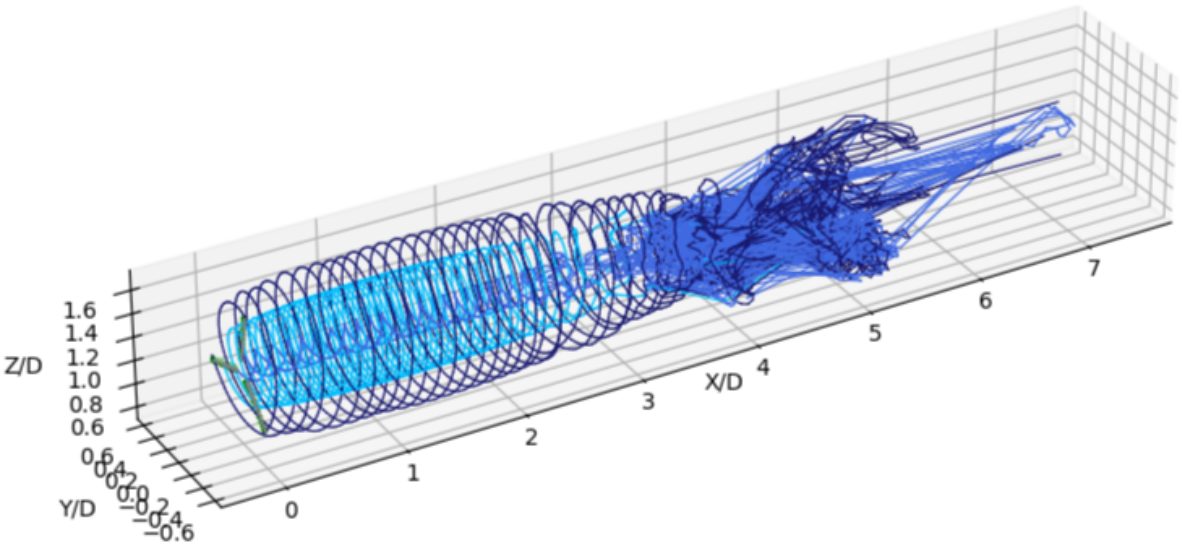

Figure 12.3: 3D Wake geometry of the NREL-2MW turbine in isolation

12.2.1. Kite set-up

The kite is positioned downstream of the rotor at a normalized distance of one rotor diameters, where the center is aligned with the axis of rotation ($Y = 0$). Vertically, the kite is located just above the rotor disk, at a height corresponding to one-quarter of the rotor diameter. This placement ensures that the kite interacts with vortices from the near-wake region, where the largest velocity deficit can be found. The extent to which this will affect the rotor itself will be considered at a later stage.

Aerodynamically, the kite is modeled as a single, untwisted wing in horizontal flight. Its aerodynamic characteristics are represented by a simple chambered airfoil shape of 12% thickness: the *NACA 2412*. This airfoil type is chosen to approximate the main features of ram-air AWE systems. The airfoil shape is assumed constant along the wingspan. The two-dimensional polar is computed with XFOIL for a chord Reynolds number of six million. The resulting lift curve, shown in Figure B.2, is corrected for three-dimensional effects using the Viterna method with an aspect ratio of two.

Regarding the geometry, the quantities are determined based on the reference projected surface area of $S_k = 470m^2$ and the target pressure jump of $\Delta p = 39Pa$ [9]. With a tip-to-tip span to $b = 32m$, the average chord length is around $\bar{c} = 14.7m$. The spanwise chord distribution is approximated by a semi-elliptical function to approach an elliptical lift distribution and constant downwash. To prevent infinitely small tip chord length, Eq. 12.2 includes an offset of $c_k = 1m$. The maximum chord length, $c_{max} \approx 18.45m$, follows from the required wing surface area. A schematic representation of the kite planform is shown in Figure 12.4, where the quarter-chord line is defined to be straight.

$$c(\hat{r}) = c_k + (c_{max} - c_k)\sqrt{1 - 4\hat{r}^2} \tag{12.2}$$

$$\Delta p = \frac{L}{S_k}, \qquad L = q_{w_\infty} C_L \int_{-1/2}^{1/2} c(\hat{r}) d\hat{r} \tag{12.3}$$

The kite is treated as a rigid lifting device with a constant angle of attack and zero slip angle. Assuming inviscid, incompressible flow, the pressure jump is related to the generated lift force, according to Bernoulli's

Table 12.4: Geometric input parameters for kite model in the kite-turbine configuration

Geometric variable	Symbol	Setting
Kite's center point	$(X, Y, Z)_k$	(20,0,160) m
Radial distance	$\hat{r}$	0 – 1
Projected surface area	S_k	470 m
Wing span	b	32 m
Chord distribution	$c(\hat{r})$	semi-elliptical
Average chord length	$\bar{c}$	14.7 m
Angle of attack	α	7.5 °

principle. Since the angle of attack is uniform along the span, the lift coefficient is constant at a given value of $C_L = 1.05$. This value, calculated using Eq. 12.3, is set to mimic the pressure jump from the reference study. For the kite's airfoil, *NACA 2412*, this corresponds to a global angle of attack of approximately $7.5°$. All geometric input parameters of the kite model are summarized in Table 12.4, while the numerical simulation settings match those used for the isolated wind turbine case of Table 12.3.

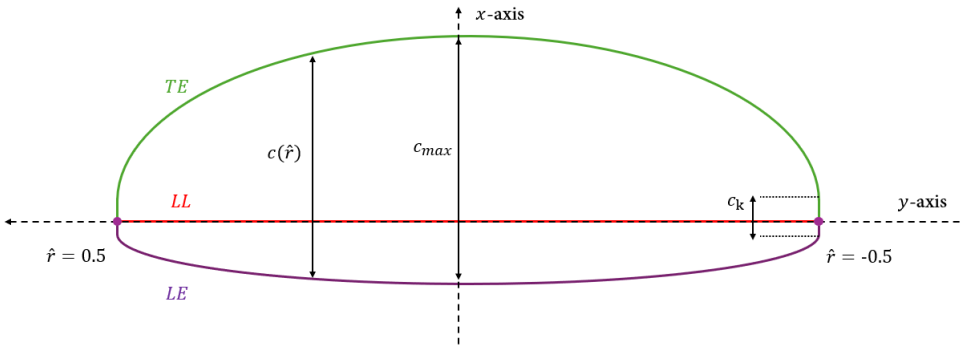

Figure 12.4: Planform geometry of the kite model: an untwisted semi-elliptical wing, with straight quarter-chord line.

12.2.2. Results of kite-turbine simulation

The introduction of the kite in the simulation domain fundamentally changes the dynamics of the flow and the wake recovery process. As seen in Figure 12.5 The three-dimensional wake geometry becomes more complex and irregular. The kite generates its own vortex system, parallel to that of the wind turbine. Both vortex systems interact with each other and the kite vortices distort the helical structures that are shed from the rotor blades. Since the kite is located at a certain distance above the rotor area, the kite-induced effect on the wake shape is most visible in the top part of the disc. It even appears that the kite causes the wake to be squeezed downwards from the top. This suggests that the wake shape is no longer symmetrical across the rotor axis of rotation and that the shape is changing.

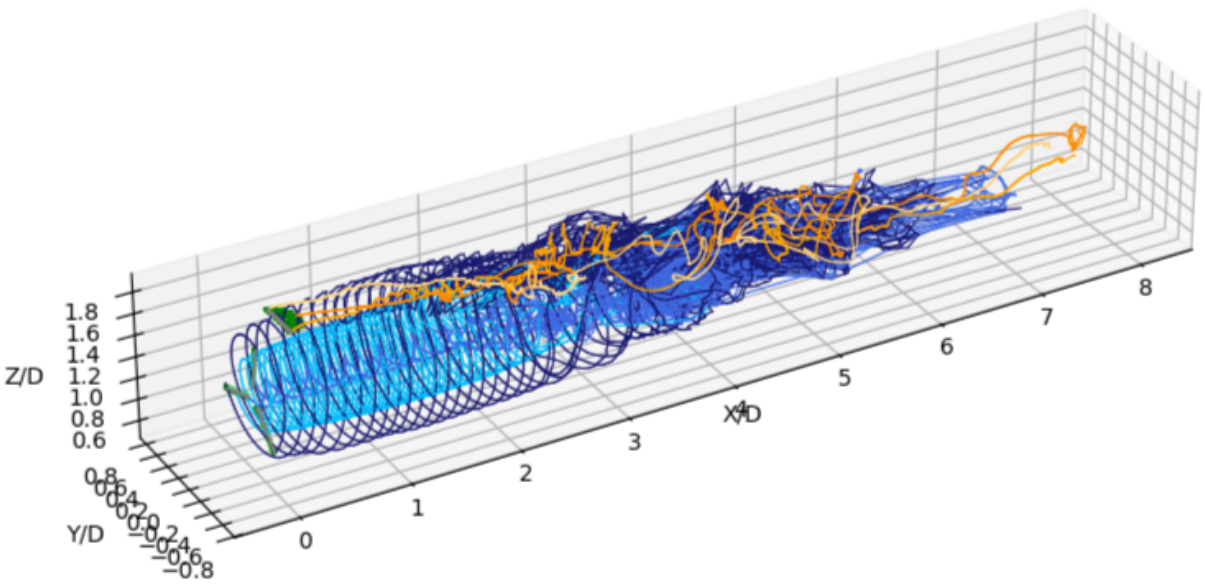

Figure 12.5: 3D Wake geometry of Kite-Turbine setup

In the side-view visualization of Figure 12.7, the kite-turbine interaction becomes more apparent. The wake is broader and extends more in the vertical direction, with noticeable deflection and dispersion of the vortices, in particular the tip vortices. The clear pattern which was seen in the isolated turbine case in Figure 12.6, is much less evident in the combination with the kite. This implies that the kite disrupts the organized roll-up motion of the turbine wake flow, which increases turbulence mixing and accelerates the wake recovery process. Another striking phenomenon can be found in the movement of the centerline of the wind turbine wake. Whereas in the isolated case it clearly remained constant at the rotor axis, in the current setup the centerline shifts in the vertical direction. Looking specifically at the blue vortex line, which describes the root vortices, it can be seen that the center of the helix deflects downward near two diameters downstream ($x/D = 2$). After that, the wake appears to start meandering in the vertical direction, with the centerline shifted accordingly. This indicates that the kite not only compresses the turbine's wake from above, but also directs the entire wake downward.

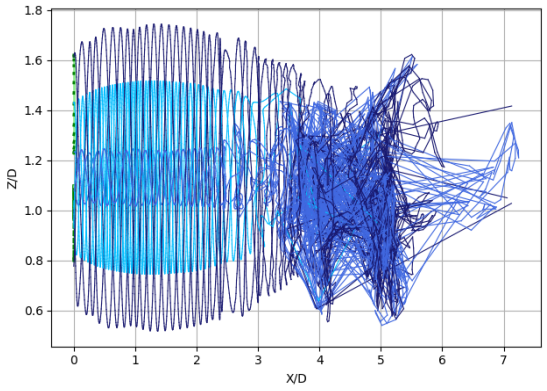

Figure 12.6: Side-view of the wake geometry in the isolation turbine setup

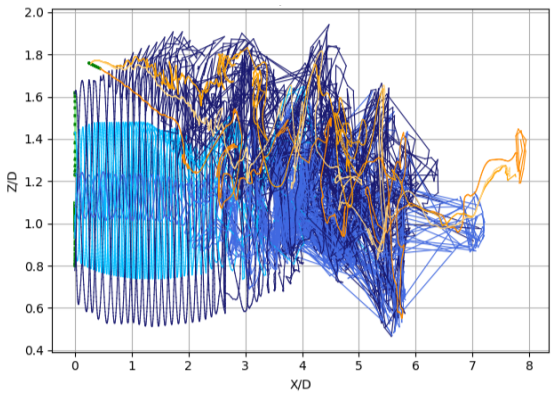

Figure 12.7: Side-view of the wake geometry in the kite-turbine configuration

In order to make a better statement about the potential changes in the wake geometry, the velocity deficit could be plotted in the *Z,Y-plane* at various axial positions downstream. To eliminate the periodic

blade-passage effects from the instantaneous induced velocity field, temporal averaging of several time snapshots would be required. Since the information from the entire plane is now relevant, no azimuthal averaging techniques can be conducted here. However, this analysis is not included within the thesis scope and is therefore recommended for future research.

The aerodynamic coupling between the two lifting devices can be investigated by the spanwise distribution of bound circulation. Given that the kite is in a relatively close proximity of the rotor disc in the current simulation setup, it is to be expected that the kite-turbine interaction will be reflected in both the circulation of the kite and that of the turbine blades. As the vortices of the kite create an induced velocity on the turbine blades, the effective AoA changes and therefore the circulation strength. These vortices will in return influence the kite's aerodynamics and so on. However, as can be seen in Figure 12.8, the distribution of bound circulation of the rotor blades remains unchanged when compared to the isolated turbine case. While this effect would logically make sense at large distances between the two systems, it is remarkable that hardly any effect is visible at the current distance. This would suggest that the current version of the K-TWIST solver may not be capturing the mutual influence between the kite and the turbine correctly in the aerodynamic loading. This will need to be investigated further by reducing the distance to the kite. If the impact remains invisible even at shorter distances, the solver will most likely have a coupling error.

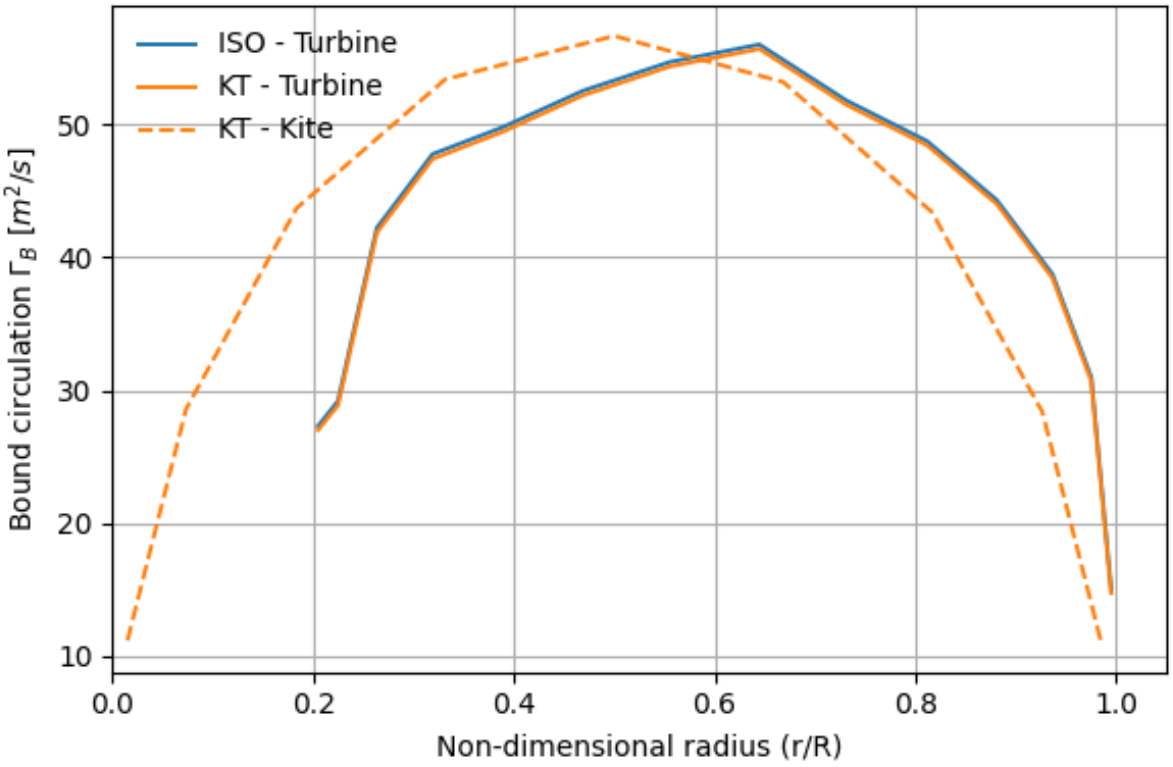

Figure 12.8: Distribution of bound circulation of the NREL-2MW wind turbine and the kite model

The effect of the altered flow dynamics is highly visible, when looking at the axial velocity profile in Figure 12.9. While the velocity deficit is fairly consistent exactly at the rotor disc, rather shortly behind the rotor, the axial velocity is slightly lower than in the isolated case. This suggests that the kite adds to the local momentum extraction from the wake flow. However, as the wakes moves downstream, the deficit recovers much sooner in the domain. The point of minimum velocity moves upstream and its value becomes significantly higher than in the baseline. In addition to the faster flow recovery, the rate at which the recovery is taking place also appears to have increased. This trend signifies a strong influence of the kite on the wake recovery of the wind turbine wake. The vertical profiles in Figure 12.10 confirm that the core of the wake is narrower and that the deficit decreases more steeply with the radius. This suggests

that the entrainment of the high-momentum ambient air occurs earlier. Zooming in on one of these profiles in the rear field shows that the profile is no longer symmetrical across the rotor axis. The upper part of the rotor disk appears to recover faster than the lower part, indicating that the extra entrainment happens in the vertical direction from the flow above the wind turbine. In other words, the kite draws the higher energy-carrying air into the wake of the turbine.

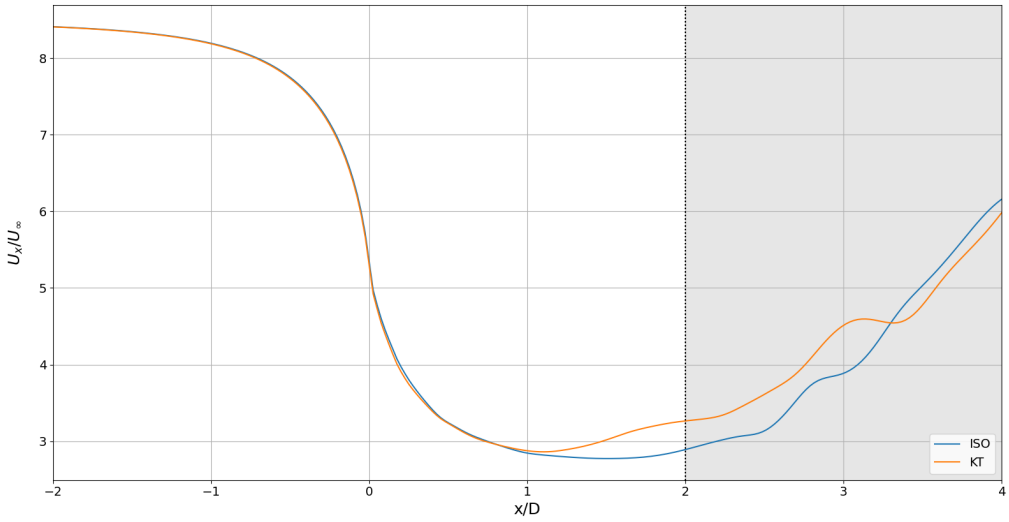

Figure 12.9: Rotor-averaged, axial velocity deficit on the rotor-axis for the Kite-Turbine setup (azimuthal averaged)

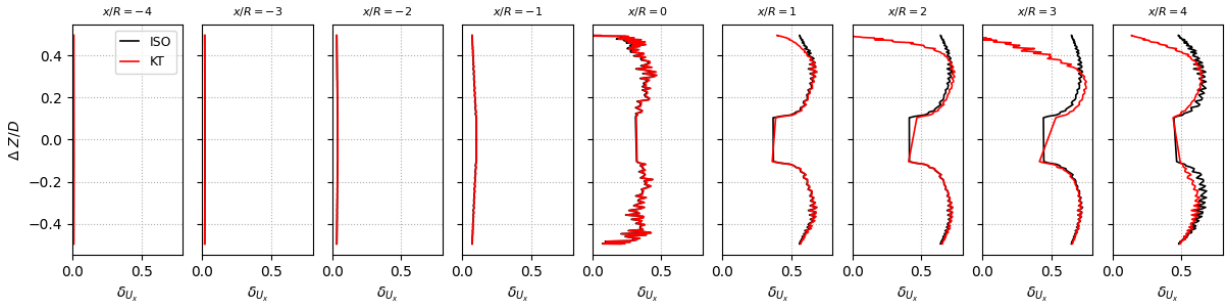

Figure 12.10: Variation of the velocity deficit with height for the Kite-Turbine setup

A more quantitative measure of the wake recovery, as suggested by the previous CFD studies on the topic, is the vertical momentum flux (VMF). As previously mentioned, this metric is defined in this work as a rotor-averaged parameter of a virtual turbine at downstream positions. The spatial variation of VMF is provided in Figure 12.11, with the isolated turbine case as a benchmark. In contrast to the near-zero value observer for the base-case, the coupled case shows a substantial increase in the VMF within the region of physical consistency ($x/D \leq 2$). Beyond this point, the downstream numerical effects become significant and the wake is not fully converged. The deviation is already noticeable in front of the rotor plane, indicating that the kite-induced effects extend upstream and alters the incoming velocity field of the turbine. Downstream of the rotor, the VMF appears to continue to elevate, proving that the kite generates additional vertical transport of momentum. This corresponds very well with the observed acceleration of velocity recovery. It should be noted that the oscillations, most obvious in the far-field, may also be caused by a wake shift. Since the VMF is calculated over a fixed virtual rotor disk at an axial distance, the wake displacement may cause part of the wake to be no longer captured. Taking vertical wake meandering

as an example, where the centerline undergoes slow displacements, this would appear as an oscillation in the computed VMF in the present method. As the wake moves up and down relative to the virtual sampling disk, alternating regions of induced velocities would contribute to the flux in a periodic manner. In theory, these fluctuations can be reduced by extending the window in the temporal averaging post-process. However, as wake meandering typically occurs at an order of magnitude slower than the rotor frequency, the averaging period needs to cover at least one meander cycle. Complete removal of the effect is not possible within a finite number of discrete time snapshots.

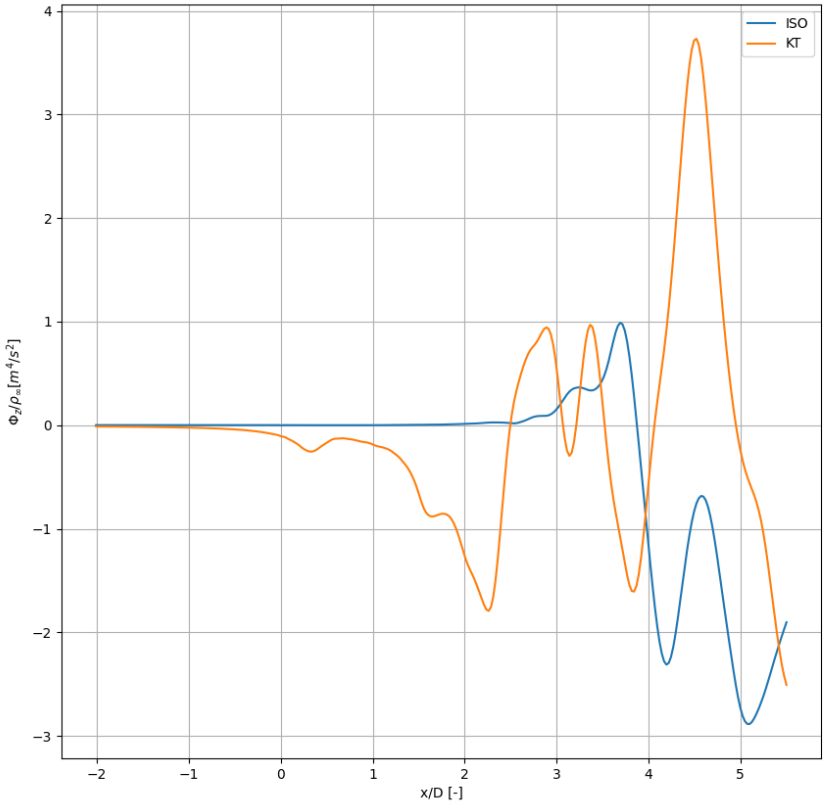

Figure 12.11: Mean kinematic vertical momentum flux on the rotor-axis for the Kite-Turbine setup

Overall, the kite-turbine interactions results in a shallower near-wake velocity deficit and a faster wake recovery downstream. While the recovery rate was approximately $0.5s^{-1}$ in the isolated turbine case, the kite's influence causes a significant gain to $0.6s^{-1}$. The increased vertical momentum flux and the more chaotic wake structure indicate that the kite can be used as an external flow-control device. By stimulating the turbulent mixing process, the re-energisation of the wake flow can be accelerated. Physically, it appears that the kite behaves both as a vortex generator as well as a flow deflector. The vortices shed by the kite break down the coherence of the turbine wake, while the it steers higher-momentum air into the wake region.

It should be noted that within the current simulation setup, the flow field is only physically reliable up to approximately two rotor diameters downstream ($x/D \leq 2$). Beyond this distance, the wake behavior becomes influenced by the domain boundaries and the numerical limitations. In addition, the current post-processing computes rotor-averaged quantities over a virtual downstream rotor disk. As the wake evolves and moves away from the centerline, parts of the wake may fall outside of the sampling area and are not included in the averaged metrics. This causes the computed quantities, such as the velocity deficit

or vertical momentum flux, to deviate from their true physical values. Since wind turbines in practical wind farms are typically spaced at least five rotor diameters apart, the present configuration does not allow for a realistic estimation of wind farm efficiency or inter-turbine wake recovery. The results should therefore be considered merely as an illustration of the potential analysis rather than as a quantitative assessment of performance at wind farm level. To obtain physically meaningful predictions of wind farm efficiency, the simulation duration would need to be extended accordingly.

12.2.3. Parametric study on the kite span

Provided that the distribution of bound circulation remains largely unchanged compared to the case of the isolated turbine, it seems more practical to prescribe the distribution in advance. This procedure significantly reduces the computational costs, as it removes the iterative coupling between the blade loading and the induced velocities on the lifting line. For the present study, this assumption is reasonably valid. The flow behavior close to the blade is mainly driven by the influence of local vortices, while the kite-turbine interactive effects show to be more present further downstream.

From the results of Figure 12.9, it is evident that the simulation duration of the coupled kite-turbine setup must be extended, in order to obtain meaningful results of the velocity field at greater distances downstream. In the current setup, the solution has not yet fully converged in the far-wake region, as the wake is still searching for its quasi-steady optimum. However, the extension of the the total time of the simulation has a direct relation with the total number of wake elements. As expressed in Eq. 11.12, this growth leads to a substantial rise in computational time due to the quadratic scaling of the induced velocity computation. This limitation is well-known in free-wake vortex methods, where the computational effort grows rapidly as the wake is lengthened [115]. In the absence of coupling with a more efficient model for the far-wake, the only way to mitigate the computational blow-up is by adjusting other simulation input parameters. As discussed in Section 11.1.3, these include the number of devices, number of blades, spatial resolution and the time step count. Only by making such a trade-off, the K-TWIST can be efficiently used to conduct a broader parametric study of key kite parameters, such as the angle of attack, relative position, wingspan and flight height.

To demonstrate the potential of a similar approach, a simplified case of the kite-turbine setup was conducted, in which both the aerodynamic devices were modeled using two blade segments of the lifting line. The distribution of bound circulation is prescribed as the mean value obtained from the previous case study. The simplification of a singular horseshoe element per blade allows for a significant reduction in computational costs, opening up parameter variation of the kite. For the present study, the interaction between the kite and the wind turbine is simulated for different kite spans, while all other parameters are kept constant. The major geometric and simulation input parameters of the setup are summarized in Table 12.5.

Table 12.5: Input parameters for the parametric study on the kite-turbine case with singular blade elements

Turbine variable	Symbol	Setting
Hub location	$(X,Y,Z)_{wt}$	(0,0,100) m
Number of blades	N_B	3
Radial distance	$\hat{r}$	0.2 – 1
Blade radius	R	40 m
Bound circulation	$\Gamma_{B_{wt}}$	50 m^2/s
Kite location	$(X,Y,Z)_{wt}$	(0,0,160) m
Radial distance	$\hat{r}$	0 – 1
Kite wingspan	R	16, 24, 32 m
Angle of attack	α_k	7.5 $^\circ$
Bound circulation	Γ_{B_k}	40 m^2/s

Simulation parameter	Symbol	Setting
CPU core count	N_{CPU}	20
Number of segments	N_S	2
Time step	Δt	0.05 s
Simulation time	T_{tot}	150 s
Rotational speed	Ω_{wt}	1.5 rad/s

From the results of the axial velocity along the center axis in Figure 12.12, relatively similar trends can be found as in the previous simulations with a higher-fidelity. This suggests that the reduced-order blade representation effectively captures the primary flow interaction between the turbine and the kite. Nevertheless, quantitative differences can be observed. While the complex case showed a pronounced shift and reduction in the maximum velocity deficit, in the simplified case this effect seems to have disappeared. However, the recovery rate remains enhanced, indicating that the kite-induced mixing effect still holds, even at lower blade resolution. Therefore, it can be assumed that the simplified approach can be used for a qualitative analysis of the more complex kite-turbine setup.

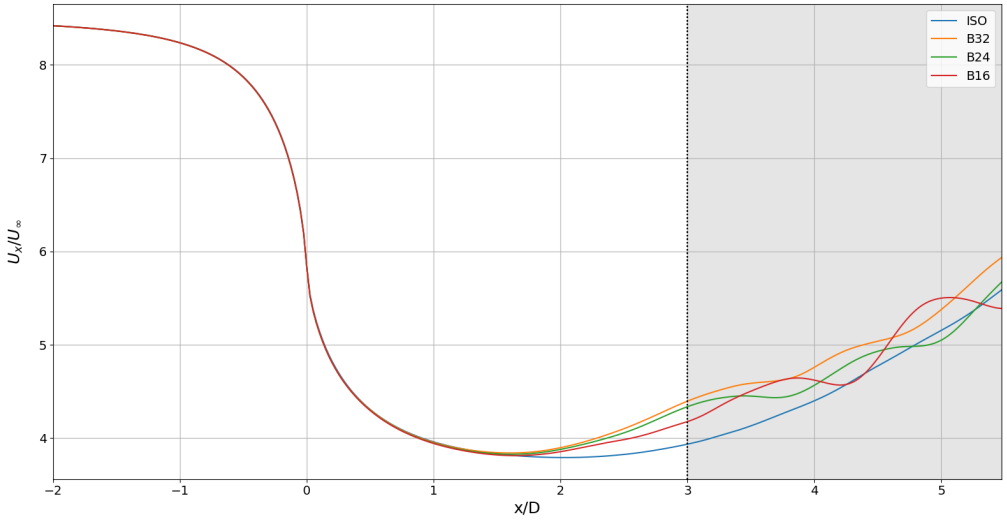

Figure 12.12: Rotor-averaged, axial velocity deficit on the rotor-axis for the kite parameter study with singular blade elements

The influence of the kite's span on the induced effect on wake recovery is particularly evident in the axial velocity deficit profiles, shown in Figure 12.13. From a qualitative perspective, the results show that there is in fact a connection between the kite's span and the induced effect. For a larger kite, the effect on the wake recovery becomes greater. This trend is consistent with the findings of the parametric study with CFD-RANS [10]. However, the effect of an increased span appears to shrink for large numbers. As seen in Table 12.6, the difference between the second ($b = 32$) and third case ($b = 24$) is less than that of the third and last case ($b = 16$). This suggests that there might exist a maximum value of the span, beyond which further increases have no additional return in terms of flow recovery. Physically, this could be attributed to the finite lateral extent of the wake geometry, whereby the vortices of a kite span that exceeds the effective wake width has a reduced interaction with the wake. Nevertheless, this observation should be interpreted with caution, given the rough spatial resolution of the aerodynamic elements and the assumption of temporal invariance of bound circulation. In order to confirm the statement quantitatively, a parametric study using the complete setup is required.

From the perspective of computational efficiency, the difference in simulation time between the methods is significant. The reference LES simulations typically required 8 days to complete [9], whereas the complex configuration of Section 12.2.2 was completed in approximately 1 day. By contrast, the simplified kite-turbine setup, with prescribed bound circulation and low spatial resolution, reduced the simulation time to just about 1 hour. This demonstrates the efficiency of the reduced-order approach for conducting parametric studies, while still capturing qualitative trends of the kite-assisted wake recovery. For a quantitative assessment of the impact of the kite's length, the parametric study should be repeated with a higher resolution.

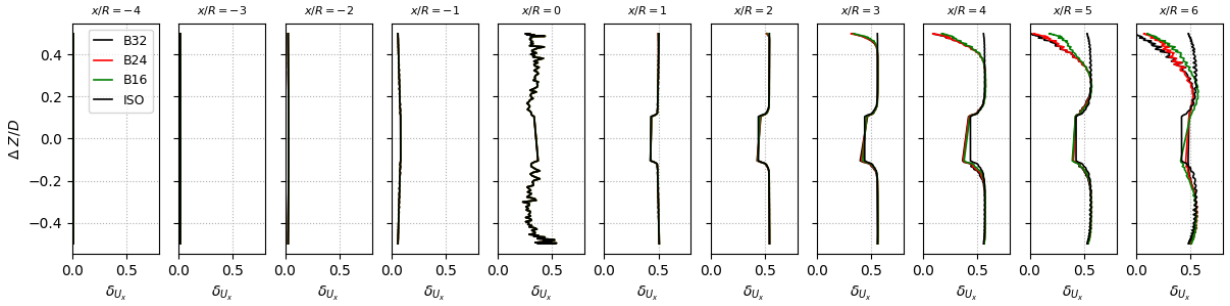

Figure 12.13: Axial velocity deficit profile for the kite parameter study with singular blade elements. The height (Z) is relative to the wind turbine hub in rotor diameters.

Table 12.6: Summary of the wake recovery characteristics at $x/D = 2$ for different kite-span configurations

Result	SOLO	B32	B24	B16
Axial velocity	3.9	4.45	4.35	4.2
Local slope	0.09	0.30	0.26	0.20
Relative recovery rate	1.0	3.3	2.9	2.2

Part V

Closure

13

Conclusion

This thesis work sought to explore the impact of kite systems on the wake recovery of wind turbines, and thereby the wind farm efficiency. In order to conduct this research, a novel simulation framework has been developed. The model can be used to simulate the dynamic flow interaction in the wake of coupled kite-turbine configurations. This **K**ite-**T**urbine **W**ake **I**nteraction **S**imulation **T**ool (K-TWIST) is verified and an initial case study has been performed, demonstrating the potential applications.

The very first step was to assess the numerical accuracy of the model in capturing key flow characteristics of wind turbine wakes. By means of a verification analysis, it was found that the model reproduced important aerodynamic phenomena, including blade loading, vortex roll-up and wake contraction with a sufficient accuracy. In an additional analysis of the kite in straight flight, it became apparent that the principle of downwash was captured well modeled as well. Although K-TWIST does not explicitly resolve the three-dimensional flow field, it represents the dominant flow behavior in the wake. The vortex-based method offers a mid-fidelity framework for parameter optimization at a reasonable computational efficiency. The numerical performance of the model has been increased by employing parallel computation techniques. The K-TWIST revealed high scalability, reducing the computational time substantially. With the increasing number of simultaneously operating CPU, large simulations can be conducted that would otherwise be extremely time-consuming.

With confidence in the model's capabilities, the research focus turned to its application in the study on kite-turbine wake interaction. From the simulation results of the comparative analysis, some noteworthy outcomes were revealed. The kite creates an additional downward flow component that increases the vertical entrainment with the outer wake region. This accelerates the turbulence mixing process that governs the re-energisation of the wake. The maximum velocity deficit is less and the flow recovers both quicker and faster than a turbine in isolation. The interaction between the vortices of the kite and those of the turbine also caused a change in the wake's shape. With the kite centrally located above the rotor, a deviation was obtained in the symmetry of the induced-velocity field. This can cause the wake to meander, which is hard to capture in the current post-processing.

To better understand the impact of the kite configuration on the wake recovery, a qualitative parametric study on the kite's wingspan was conducted. Both models of the aerodynamic devices were simplified to a singular blade element with a prescribed circulation, to speed up the computation. While the results showed that a larger kite span creates a stronger entrainment effect, it pointed towards a potential optimal length. However, as this analysis is performed with a very simplified representation, the results should be considered merely as a guideline for future optimization studies.

Despite the scope of the research is limited to a single turbine, the implications for a wind farm operation are significant. As the enhanced wake flow recovery increases the perceived inflow velocity at downstream turbines, the total power output at farm level would be higher. While the scale of the improvement in real-world applications is dependent on other operating conditions, including the environment and control strategies, the concept still offers a promising new way to reduce wake losses. Introducing kite systems to wind farms can serve as an active wake recovery strategy, while they may contribute towards the energy yield.

14

Recommendations for future work

The results from this work have opens up several promising directions for future research. To help a successor get started, recommendations have been drawn up for both the model development and the kite-turbine analysis. As a result, the suggestions have been divided into two categories. The first part focuses on the further enhancement of the K-TWIST model, by highlighting key limitations of the current version and potential points of improvement. In the second half of this chapter, the center of attention shifts towards the application of the K-TWIST model in the research of the kite-induced effect on wind turbine wake recovery. With this structure, a clear distinction can be made between the refinements of the computational framework itself and he use to expand the knowledge of the new wake recovery concept.

14.1. K-TWIST v.2

The current version of K-TWIST has proven capable of capturing key aerodynamic phenomena in a coupled kite-turbine configuration. The framework is built on a combination of lifting line and free wake methodology, where the wake is described by a system of straight vortex filaments with a time-dependent vortex core. However, from the results of both the verification and the case study it has been concluded that the model can be upgraded. Modifications and extensions to both the methodology and the implementation can significantly improve the numerical performance and physical accuracy of the K-TWIST model.

Enhancing numerical efficiency

- While the current framework purely based on a LL-FW method has a high physical fidelity, it is extremely expensive computationally for large simulations. A hybrid approach should be introduced instead, where the near-wake is still solved using the LL-FW method, but the far wake is addressed with a separate technique. One can think of a ring-vortex method or a filament order reduction. As these coupling strategies would drastically reduce the number of elements in the induced-velocity calculation, it reduces the computational costs while maintaining high-fidelity in the near wake region.
- The induced-velocity calculation via the Biot-Savart law currently considers every interaction between vortex filament and control point in the entire wake vortex system. Introducing a cutoff distance here, in which the contributions from filaments far away are approximated or even neglected. By introducing such a boundary, the number of contributions are limited and the computationally heavy induced-velocity calculation becomes more efficient. Caution is recommended, as the relation does not depend on the Euclidean distance, but on the orthogonal distance. If this particular distance is applied, it is advised to analyze the effect on physical consistency. Other techniques such as tree codes or fast multipole methods, which cluster vortices and approximate their combined effect, could also be considered.
- The system of differential equations that control the convection of the vortex filament endpoints is currently solved with the explicit Forward-Euler scheme. The results have demonstrated that the current version exhibits numerical instability, even at very small time steps. Therefore, in a refined version of K-TWIST it is recommended to implement a more advanced time-marching method. By using the implicit predictor-corrector scheme, extreme deviations are smoothed out. This creates a more accurate and more stable approximation of the temporal evolution of the vortex, with merely a small increase in computational cost.

Improving physical accuracy

- At present, the inflow velocity is assumed to be uniform with height. While this simplified approach can be very insightful, it ignores the vertical shear characteristic of the ABL. By implementing a vertical wind profile, either logarithmic or power, an additional effect of the kite can be analyzed. Since the kite is located above the wind turbine, it could exploit the higher momentum flow. As the relative incoming velocity is now increased, the aerodynamic loading increases and potentially the impact on wind turbine wake recovery as well.
- Additional, other additional flow phenomena should be included in the ambient flow to better mimic realistic wind conditions. A future version of K-TWIST may take into account irregular wind flows, ambient turbulence, ground effect, surface roughness or atmospheric stability. As these are proven to have a major influence on the flow recovery of wind turbines themselves, there is a considerable probability that is also affects the kite-induced effect.
- In the current version of K-TWIST, the kite is modeled is a very simplified manner. While the model assumes an untwisted, un-swept wing with an elliptical chord distribution and no spanwise curvature, it remains uncertain whether such an idealized configuration accurately represents modern kite designs. For a second version of the model, it is therefore recommended to upgrade from a LL to a lifting surface method in the aerodynamic modeling of the kite. This would be able to represent more complex geometry and increase the numerical accuracy of the three-dimensional flow behavior around the kite. Furthermore, the kinematic motion of the kite should be upgraded from a straight flight towards more realistic patterns, like figure-eight or circular trajectories. This dynamic movement may also alter the kite-induced effect on wake recovery. As this creates a time-dependent induced velocity field, it can have a pulsating wake effect, which has been proven to offer positive returns in previous research into dynamic pitch control.
- The main driver of the wake recovery is the turbulent momentum exchange between adjacent flow layers. In the current framework, the viscous diffusion is reflected by a single constant apparent viscosity parameter, which is included in the temporal evolution of the vortex core radius. While this simplification captures a general diffusion effect, it neglects any spatial variation of turbulence in the flow. Future development of the model should consider an apparent viscosity parameter that changes with downstream distance or local shear. This function can be linked to empirical wake growth studies or turbulence closure models.

14.2. Kite-turbine wake interaction research

Next to the recommended improvements of the K-TWIST framework, a number of suggestions on the application of the model towards a deeper understanding of the coupled aerodynamics between the wind turbine and the kite. The results from this study have, once again, highlighted the potential benefits of utilizing kites for enhancing wake recovery. However, many of the underlying physical phenomena are still insufficiently investigated. The subsequent directions have been proposed to explore the applicability of K-TWIST simulations and potentially fill in some gaps in the research topic.

- A first step could be to further examine the spatial alignment of the kite relative to the turbine. The present study was limited to a single downstream distance, where the effect on the appeared to be negligible. By reducing this distance in a follow-up study, the insensitivity of turbine aerodynamic loading to the kite deployment can be validated. This may reveal non-linear interaction effects that are dampened in the current simulation setup or uncover a potential transition point. In addition, a subsequent study could investigate the impact of the relative lateral position of the kite. In the current configuration, it is positioned exactly in the center of the rotor plane, creating a highly symmetric flow field. However, introducing a slight offset could lead to the deflected wake, which may have additional recovery benefits similar to that with yaw misalignment.
- The work of this thesis merely offers a showcase of the possibility to conduct a parametric study on the kite. It is therefore recommended to expand this study within future work on the topic. This could include, for example, flight altitude, angle of attack, flight pattern and geometric parameters (shape, aspect ratio, sweep angle, curvature). Although they all have a direct influence on the flow field, the flight pattern requires specific attention as it is creates a dynamic effect on the system. With the results from individual parametric kite studies, the kite-turbine configuration can be optimized to minimize the effect wake losses or maximize the energy yield at wind farm level.
- While the current case study concentrates primarily on the kite-induced effect on the near-wake, the wake recovery occurs for the most part further into the field. The simulation domain should be extended to create a velocity field to at least five rotor diameters of distance. This allows for a comparison of the results with previous work that used high-fidelity CFD simulations. With the increased distance, it is possible to simulate the effect on a downstream wind turbine with greater accuracy. However, within the current K-TWIST framework this computation is not efficient and requires an upgraded version beforehand.
- At last, it is recommended to investigate the effect of additional flow characteristics such that the simulation better represents wind conditions in real-world applications. An increased turbulent intensity may contribute to the kite-induced entrainment, while a more stable ABL may suppress the turbulence mixing. Other factors that should be considered are gusts, wind shear and terrain effects.

References

[1] International Renewable Energy Agency (IRENA), *World Energy Transitions Outlook 2024: 1.5°C Pathway*. Abu Dhabi: International Renewable Energy Agency, 2024.

[2] R. J. Barthelmie, K. Hansen, S. T. Frandsen, *et al.*, "Modelling and measuring flow and wind turbine wakes in large wind farms offshore," *Wind Energy: An International Journal for Progress and Applications in Wind Power Conversion Technology*, vol. 12, no. 5, pp. 431–444, 2009.

[3] P. Jha, E. Duque, J. Bashioum, *et al.*, "Unraveling the mysteries of turbulence transport in a wind farm," *Energies*, vol. 2015, pp. 6468–6496, Jun. 2015. DOI: 10.3390/en8076468.

[4] B. S. Akin Ilhan and M. Bilgili, "A review: Diffuser augmented wind turbine technologies," *International Journal of Green Energy*, vol. 19, no. 1, pp. 1–27, 2022. DOI: 10.1080/15435075.2021.1914628.

[5] D. van den Berg, D. de Tavernier, and J.-W. van Wingerden, "The dynamic coupling between the pulse wake mixing strategy and floating wind turbines," *Wind Energy Science*, vol. 8, no. 5, pp. 849–864, 2023. DOI: 10.5194/wes-8-849-2023.

[6] C. L. Archer, A. Vasel-Be-Hagh, and R. Nouri, "The coriolis force and the direction of rotation of the blades significantly affect the wake of wind turbines," *Applied Energy*, vol. 277, pp. 115–511, 2020.

[7] S. Watson, A. Moro, V. Reis, *et al.*, "Future emerging technologies in the wind power sector: A european perspective," *Renewable and Sustainable Energy Reviews*, vol. 113, 109270, 2019. DOI: https://doi.org/10.1016/j.rser.2019.109270.

[8] D. Boonman, C. Broich, R. Deerenberg, *et al.*, "Wind farm energy," Wind Energy & Propulsion Group, Faculty of Aerospace Engineering, TU Delft, Jun. 2011. [Online]. Available: https://resolver.tudelft.nl/uuid:9ec5078c-c02a-43db-99b9-00bde8871b58.

[9] E. Ploumakis, "Improving the Wind Farm efficiency by simple means," Wind Energy Group, Faculty of Aerospace Engineering, TU Delft, Sep. 2016. [Online]. Available: https://resolver.tudelft.nl/uuid:a273b26a-b4bd-4388-8eee-193c6d22626b.

[10] J. Kokkedee, "Wind farm wake flow recovery with the use of kites," Wind Energy Group, Faculty of Aerospace Engineering, TU Delft, Jun. 2022. [Online]. Available: https://resolver.tudelft.nl/uuid:79bb9fd7-6646-4e85-b562-c93a38189b98.

[11] T. Kuhlman and J. Farrington, "What is Sustainability?" *Sustainability*, vol. 2, no. 11, pp. 3436–3448, Nov. 2010. DOI: 10.3390/su2113436.

[12] N. A. Robinson, Ed., *Agenda 21: Earth's action plan.* English. New York: Oceana Publications, Inc., Aug. 1993.

[13] U. Nations, "Transforming our world, the 2030 agenda for sustainable development.," *General Assembly Resolution*, no. A/RES/70/1, Oct. 2015.

[14] U. Nations, "Paris agreement," *Framework Convention on Climate Change*, no. FCCC/CP/2015/L.9/Rev.1, Dec. 2015. [Online]. Available: https://unfccc.int/sites/default/files/english_paris_agreement.pdf.

[15] IEA, *Net zero by 2050: A roadmap for the global energy sector*, Licence: CC BY 4.0, 2021. [Online]. Available: https://www.iea.org/reports/net-zero-by-2050.

[16] H. Ritchie, P. Rosado, and M. Roser, "Breakdown of carbon dioxide, methane and nitrous oxide emissions by sector," *Our World in Data*, 2020. [Online]. Available: https://ourworldindata.org/emissions-by-sector.

[17] Climate Watch, *Electricity and heat [dataset]*, 2021. [Online]. Available: https://www.climatewatchdata.org/.

[18] NASA - Intergovernmental Panel on Climate Change, *The effects of climate change*. [Online]. Available: https://science.nasa.gov/climate-change/effects/.

[19] D. M. Gilford, J. Giguere, and A. J. Pershing, "Human-caused ocean warming has intensified recent hurricanes," *Environmental Research: Climate*, vol. 3, no. 4, 045019, Nov. 2024. DOI: 10.1088/2752-5295/ad8d02.

[20] R. van de Wal, A. Melet, D. Bellafiore, *et al.*, "Sea level rise in europe: Impacts and consequences," *State of the Planet*, vol. 3-slre1, no. 5, 2024. DOI: 10.5194/sp-3-slre1-5-2024.

[21] J.-C. Espinoza, J. C. Jimenez, J. A. Marengo, *et al.*, "The new record of drought and warmth in the Amazon in 2023 related to regional and global climatic features," *Scientific Reports*, vol. 14, no. 1, Apr. 2024. DOI: 10.1038/s41598-024-58782-5.

[22] E. Bevacqua, O. Rakovec, D. L. Schumacher, *et al.*, "Direct and lagged climate change effects intensified the 2022 European drought," *Nature Geoscience*, Oct. 2022. DOI: 10.1038/s41561-024-01559-2.

[23] N. Sagar, K. Suresh, Y. Naveesh, *et al.*, "Forest fire dynamics in india (2005–2022): Unveiling climatic impacts, spatial patterns, and interface with anthrax incidence," *Ecological Indicators*, vol. 166, 112454, 2022. DOI: https://doi.org/10.1016/j.ecolind.2024.112454.

[24] International Disaster Database (EM-DAT), *Recorded natural disaster events, 1900-2013 [dataset]*, 2023. [Online]. Available: https://www.emdat.be/.

[25] T. E. Institute, KPMG, and Kearney, *Statistical Review of World Energy analyses data on world energy markets [dataset]*, 2024. [Online]. Available: https://www.energyinst.org/__data/assets/pdf_file/0006/1542714/684_EI_Stat_Review_V16_DIGITAL.pdf.

[26] E. energy, *Yearly Electricity Data [dataset]*, 2024. [Online]. Available: https://storage.googleapis.com/emb-prod-bkt-publicdata/public-downloads/yearly_full_release_long_format.csv.

[27] J. Lee and F. Zhao, "Global Wind Energy Report 2024," Global Wind Energy Council, Tech. Rep., Apr. 2024.

[28] N. Bento and M. Fontes, "Emergence of floating offshore wind energy: Technology and industry," *Renewable and Sustainable Energy Reviews*, vol. 99, pp. 66–82, 2019. DOI: https://doi.org/10.1016/j.rser.2018.09.035.

[29] M. Weipao, L. Chun, Y. Jun, *et al.*, "Numerical investigation of wake control strategies for maximizing the power generation of wind farm," *Journal of Solar Energy Engineering*, vol. 138, no. 3, 034501, Apr. 2016. DOI: 10.1115/1.4033110.

[30] J.-P. Françoise, G. Naber, and T. S. Tsun, Eds., *Encyclopedia of Mathematical Physics*, 1st ed. Elsevier, 2006.

[31] T. Uchida, T. Yoshida, M. Inui, *et al.*, "Doppler lidar investigations of wind turbine near-wakes and les modeling with new porous disc approach," *Energies*, vol. 14, 2101, Apr. 2021. DOI: 10.3390/en14082101.

[32] A. Crespo and J. Herna´ndez, "Turbulence characteristics in wind-turbine wakes," *Journal of Wind Engineering and Industrial Aerodynamics*, vol. 61, no. 1, pp. 71–85, Jun. 1996. DOI: 10.1016/0167-6105(95)00033-x.

[33] S. Lee, M. J. Churchfield, P. J. Moriarty, *et al.*, "A numerical study of atmospheric and wake turbulence impacts on wind turbine fatigue loadings," *Journal of Solar Energy Engineering*, vol. 135, no. 3, 031001, 2013.

[34] J. Pacheco, F. Pimenta, S. Guimarães, *et al.*, "Experimental evaluation of fatigue in wind turbine blades with wake effects," *Engineering Structures*, vol. 300, 117140, 2024. DOI: https://doi.org/10.1016/j.engstruct.2023.117140.

[35] D. Foti, X. Yang, F. Campagnolo, *et al.*, “Wake meandering of a model wind turbine operating in two different regimes,” *Phys. Rev. Fluids*, vol. 3, 054607, 5 May 2018. DOI: 10.1103/PhysRevFluids.3.054607.

[36] J. Curry, “Thermodynamics | saturated adiabatic processes,” in *Encyclopedia of Atmospheric Sciences (Second Edition)*, G. R. North, J. Pyle, and F. Zhang, Eds., 2nd ed., Oxford: Academic Press, 2015, pp. 398–401. DOI: https://doi.org/10.1016/B978-0-12-382225-3.00406-0.

[37] J. Bleeg, M. Purcell, R. Ruisi, *et al.*, “Wind farm blockage and the consequences of neglecting its impact on energy production,” *Energies*, vol. 11, no. 6, 1609, 2018.

[38] P. B. Lissaman, “Energy effectiveness of arbitrary arrays of wind turbines,” *Journal of energy*, vol. 3, no. 6, pp. 323–328, 1979.

[39] I. Katic, J. Højstrup, and N. O. Jensen, “A simple model for cluster efficiency,” in *European wind energy association conference and exhibition*, A. Raguzzi, 1987, pp. 407–410.

[40] M. Bastankhah, B. L. Welch, L. A. Martínez-Tossas, *et al.*, “Analytical solution for the cumulative wake of wind turbines in wind farms,” *Journal of Fluid Mechanics*, vol. 911, 2021. DOI: 10.1017/jfm.2020.1037.

[41] G. Pechlivanoglou, *Passive and active flow control solutions for wind turbine blades*, 2013.

[42] L. Liu and R. Stevens, “Enhanced wind-farm performance using windbreaks,” *Physical Review Fluids*, vol. 6, 074611, Jul. 2021. DOI: 10.1103/PhysRevFluids.6.074611.

[43] R. Nash, R. Nouri, and A. Vasel-Be-Hagh, “Wind turbine wake control strategies: A review and concept proposal,” *Energy Conversion and Management*, vol. 245, 114581, 2021. DOI: https://doi.org/10.1016/j.enconman.2021.114581.

[44] D. Van Der Hoek, B. Van Den Abbeele, C. S. Ferreira, *et al.*, “Maximizing wind farm power output with the helix approach: Experimental validation and wake analysis using tomographic particle image velocimetry,” *Wind Energy*, vol. 27, no. 5, pp. 463–482, Feb. 2024. DOI: 10.1002/we.2896.

[45] M. Nakhchi, S. Win Naung, and M. Rahmati, “A novel hybrid control strategy of wind turbine wakes in tandem configuration to improve power production,” *Energy Conversion and Management*, vol. 260, 115575, 2022. DOI: https://doi.org/10.1016/j.enconman.2022.115575.

[46] M. Samorani, *The wind farm layout optimization problem*. Springer, 2013.

[47] P. Malisani, T. Bartement, and P. Bozonnet, “Wind farm layout optimization with alignment constraints,” *Wind Energy Science Discussions*, vol. 2024, pp. 1–25, 2024. DOI: 10.5194/wes-2024-118.

[48] DTU Wind and Energy Systems, *Wind atlas analysis and application program (wasp)*, version 12.9.44, Technical University of Denmark, 2024. [Online]. Available: https://www.wasp.dk.

[49] G. M. Heisler and D. R. Dewalle, “2. effects of windbreak structure on wind flow,” *Agriculture, Ecosystems Environment*, vol. 22-23, pp. 41–69, 1988, Proceedings of an International Symposium on Windbreak Technology. DOI: https://doi.org/10.1016/0167-8809(88)90007-2.

[50] A. H. Rajpar, I. Ali, A. E. Eladwi, *et al.*, “Recent Development in the Design of Wind Deflectors for Vertical Axis Wind Turbine: A Review,” *Energies*, vol. 14, no. 16, 5140, Aug. 2021. DOI: 10.3390/en14165140.

[51] M. Elgendi, M. AlMallahi, A. Abdelkhalig, *et al.*, “A review of wind turbines in complex terrain,” *International Journal of Thermofluids*, vol. 17, 100289, 2023. DOI: https://doi.org/10.1016/j.ijft.2023.100289.

[52] H. Sun, H. Yang, and X. Gao, “Investigation into wind turbine wake effect on complex terrain,” *Energy*, vol. 269, 126767, 2023. DOI: https://doi.org/10.1016/j.energy.2023.126767.

[53] S. Porchetta, D. Muñoz-Esparza, W. Munters, *et al.*, “Impact of ocean waves on offshore wind farm power production,” *Renewable Energy*, vol. 180, pp. 1179–1193, 2021. DOI: https://doi.org/10.1016/j.renene.2021.08.111.

[54] U. Ahrens, M. Diehl, and R. Schmehl, *Airborne wind energy*. Springer Science & Business Media, 2013.

[55] G. Webster, "The invention of the kite," *The Kiteflyer*, vol. 98, pp. 9–14, 2004.

[56] J. D. Anderson, *Inventing Flight: the Wright brothers & their predecessors*. JHU Press, 2004.

[57] A. van Gries, *Durch Drachen getragene Windkraftmaschine zur Nutzbarmachung von Höhenwinden*, Jan. 1938.

[58] M. L. Loyd, "Crosswind kite power for large-scale wind power production," *Journal of Energy*, vol. 4, no. 3, pp. 106–111, May 1980. DOI: 10.2514/3.48021.

[59] L. Fagiano, M. Quack, F. Bauer, *et al.*, "Autonomous airborne wind energy systems: Accomplishments and challenges," *Annual Review of Control, Robotics, and Autonomous Systems*, vol. 5, no. Volume 5, 2022, pp. 603–631, 2022. DOI: https://doi.org/10.1146/annurev-control-042820-124658.

[60] J. Weber, M. Marquis, A. Cooperman, *et al.*, "Airborne wind energy," National Renewable Energy Lab.(NREL), Golden, CO (United States), Tech. Rep., 2021.

[61] J. De Schutter, J. Harzer, and M. Diehl, "Vertical airborne wind energy farms with high power density per ground area based on multi-aircraft systems," *European Journal of Control*, vol. 74, 100867, 2023, 2023 European Control Conference Special Issue. DOI: https://doi.org/10.1016/j.ejcon.2023.100867.

[62] S. Van Der Burg, M. F. M. Jurg, F. M. Tadema, *et al.*, "Dominant Designs for Wings of Airborne Wind Energy Systems," *Energies*, vol. 15, no. 19, 7291, Oct. 2022. DOI: 10.3390/en15197291.

[63] J. D. Anderson, *Fundamentals of Aerodynamics*, 6th ed. McGraw-Hill Education, 2017.

[64] B. Cantwell, *AA200 Applied Aerodynamics*, Chapter 12. Stanford University - Department of Aeronautics and Astronautics, Apr. 2015. [Online]. Available: http://web.stanford.edu/~cantwell/.

[65] L. Wang, M. Dong, J. Yang, *et al.*, "Wind turbine wakes modeling and applications: Past, present, and future," *Ocean Engineering*, vol. 309, 118508, 2024. DOI: https://doi.org/10.1016/j.oceaneng.2024.118508.

[66] N. Jensen, *A note on wind generator interaction* (Risø-M 2411), English. Risø National Laboratory, 1983.

[67] G. C. Larsen, *A simple wake calculation procedure*. Risø National Laboratory, 1988.

[68] M. Bastankhah and F. Porté-Agel, "A new analytical model for wind-turbine wakes," *Renewable Energy*, vol. 70, pp. 116–123, 2014, Special issue on aerodynamics of offshore wind energy systems and wakes. DOI: https://doi.org/10.1016/j.renene.2014.01.002.

[69] S. Frandsen, R. Barthelmie, S. Pryor, *et al.*, "Analytical modelling of wind speed deficit in large offshore wind farms," *Wind Energy*, vol. 9, no. 1-2, pp. 39–53, Jan. 2006. DOI: 10.1002/we.189.

[70] S. Xie and C. Archer, "Self-similarity and turbulence characteristics of wind turbine wakes via large-eddy simulation," *Wind Energy*, vol. 18, no. 10, pp. 1815–1838, 2015.

[71] C. L. Archer, A. Vasel-Be-Hagh, C. Yan, *et al.*, "Review and evaluation of wake loss models for wind energy applications," *Applied Energy*, vol. 226, pp. 1187–1207, 2018. DOI: https://doi.org/10.1016/j.apenergy.2018.05.085.

[72] S. Ashwin Renganathan, R. Maulik, S. Letizia, *et al.*, "Data-driven wind turbine wake modeling via probabilistic machine learning," *Neural Computing and Applications*, pp. 1–16, 2022.

[73] H. Lee, B. Sengupta, M. S. Araghizadeh, *et al.*, "Review of vortex methods for rotor aerodynamics and wake dynamics," *Advances in Aerodynamics*, vol. 4, no. 1, May 2022. DOI: 10.1186/s42774-022-00111-3.

[74] J. Dong, A. Viré, C. S. Ferreira, *et al.*, "A Modified Free Wake Vortex Ring Method for Horizontal-Axis Wind Turbines," *Energies*, vol. 12, no. 20, 3900, Oct. 2019. DOI: 10.3390/en12203900.

[75] E. Branlard, *Wind Turbine Aerodynamics and Vorticity-Based Methods*. Springer, Jan. 2017. DOI: 10.1007/978-3-319-55164-7.

[76] N. Premalatha, K. R. Srilatha, and V. Y. Mudkavi, *Analysis of Propeller by Panel Method for Transport Aircraft*. Springer Singapore, Jan. 2021, pp. 457–469. DOI: 10.1007/978-981-15-9601-8\{_}34.

[77] C. Mimeau and I. Mortazavi, "A review of vortex methods and their applications: From creation to recent advances," *Fluids*, vol. 6, no. 2, 68, 2021. DOI: 10.3390/fluids6020068.

[78] J. Aird, E. Gaertner, and M. Lackner, "Dynamic prescribed-wake vortex method for aerodynamic analysis of offshore floating wind turbines," *Wind Engineering*, vol. 43, no. 1, pp. 47–63, Dec. 2018. DOI: 10.1177/0309524x18819897.

[79] K. Shaler, E. Branlard, A. Platt, *et al.*, "Preliminary Introduction of a Free Vortex Wake Method Into OpenFAST," *Journal of Physics Conference Series*, vol. 1452, no. 1, 012064, Jan. 2020. DOI: 10.1088/1742-6596/1452/1/012064.

[80] W. Huang, R. Tang, and H. Ma, "The review of vortex lattice method for offshore wind turbines," *Renewable Energy*, vol. 236, 121450, 2024. DOI: https://doi.org/10.1016/j.renene.2024.121450.

[81] C. Dos Santos, A. Rezaei, and H. Taha, "Viscous extension of vortex methods for unsteady aerodynamics," *Physics of Fluids*, vol. 33, no. 10, 2021.

[82] Y. Tian, Y. Zhong, H. Liu, *et al.*, "A new fast simulation method of wind turbine wake based on annular vortex element," *Renewable Energy*, vol. 229, 120765, 2024. DOI: https://doi.org/10.1016/j.renene.2024.120765.

[83] D. Marten, *QBlade: a modern tool for the aeroelastic simulation of wind turbines*, Jan. 2020. DOI: 10.14279/depositonce-10646.

[84] K. Shaler, E. Branlard, and A. Platt, "Olaf user's guide and theory manual," National Renewable Energy Lab.(NREL), Golden, CO (United States), Tech. Rep., 2020.

[85] J. Murray and M. Barone, "The Development of CACTUS, a Wind and Marine Turbine Performance Simulation Code," *50th AIAA Aerospace Sciences Meeting including the New Horizons Forum and Aerospace Exposition*, Jan. 2011. DOI: 10.2514/6.2011-147.

[86] K. Shaler, B. Anderson, L. A. Martínez-Tossas, *et al.*, "Comparison of free vortex wake and blade element momentum results against large-eddy simulation results for highly flexible turbines under challenging inflow conditions," *Wind energy science*, vol. 8, no. 3, pp. 383–399, Mar. 2023. DOI: 10.5194/wes-8-383-2023.

[87] E. Branlard, I. Brownstein, B. Strom, *et al.*, "A multipurpose lifting-line flow solver for arbitrary wind energy concepts," *Wind energy science*, vol. 7, no. 2, pp. 455–467, Mar. 2022. DOI: 10.5194/wes-7-455-2022.

[88] D. R. Houck, N. deVelder, and C. L. Kelley, "Comparison of a mid-fidelity free vortex wake method to a high-fidelity actuator line model large eddy simulation for wind turbine wake simulations," *Journal of Physics Conference Series*, vol. 2265, no. 4, 042044, May 2022. DOI: 10.1088/1742-6596/2265/4/042044.

[89] A. G. Ajay, L. Morgan, Y. Wu, *et al.*, "Aerodynamic model comparison for an X-shaped vertical-axis wind turbine," *Wind energy science*, vol. 9, no. 2, pp. 453–470, Feb. 2024. DOI: 10.5194/wes-9-453-2024.

[90] T. Haas and J. Meyers, "Comparison study between wind turbine and power kite wakes," *Journal of Physics Conference Series*, vol. 854, 012019, May 2017. DOI: 10.1088/1742-6596/854/1/012019.

[91] I. Castro□Fernández, R. Cavallaro, R. Schmehl, *et al.*, "Unsteady Aerodynamics of Delta Kites for Airborne Wind Energy Under Dynamic Stall Conditions," *Wind Energy*, vol. 27, no. 9, pp. 936–952, Jul. 2024. DOI: 10.1002/we.2932.

[92] R. Damiani, F. F. Wendt, J. M. Jonkman, *et al.*, "A vortex step method for nonlinear airfoil polar data as implemented in kiteaerodyn," in *AIAA Scitech 2019 Forum*, 2019, p. 0804.

[93] D. Filkovic, “APAME 3D Panel Method,” Faculty of Mechanical Engineering and Naval Architecture, University of Zagreb, 2008. [Online]. Available: http://www.3dpanelmethod.com/home.html.

[94] J. Mehr, E. J. Alvarez, and A. Ning, “Interactional Aerodynamics Analysis of a Multirotor Energy Kite,” *Wind Energy*, Nov. 2024. DOI: 10.1002/we.2957.

[95] J. M. Jonkman and K. Shaler, *Fast.FARM user’s guide and theory manual*. National Renewable Energy Laboratory Golden, CO, USA, 2021.

[96] D. Crane and A. E. Team, *Dictionary of Aeronautical Terms*. Aviation Supplies Academics, Nov. 2020.

[97] J. Tu, G.-H. Yeoh, and C. Liu, “Chapter 6 - cfd solution analysis: Essentials,” in *Computational Fluid Dynamics (Third Edition)*, J. Tu, G.-H. Yeoh, and C. Liu, Eds., Third Edition, Butterworth-Heinemann, 2018, pp. 211–253. DOI: https://doi.org/10.1016/B978-0-08-101127-0.00006-4.

[98] P. J. Mason and D. J. Thomson, “Stochastic backscatter in large-eddy simulations of boundary layers,” *Journal of Fluid Mechanics*, vol. 242, pp. 51–78, 1992. DOI: 10.1017/S0022112092002271.

[99] D. Medici and P.-H. Alfredsson, “Measurements on a wind turbine wake: 3d effects and bluff body vortex shedding,” *Wind Energy*, vol. 9, pp. 219–236, May 2006. DOI: 10.1002/we.156.

[100] J. Finnigan, “Turbulence in plant canopies. ann rev fluid mech,” *Annual Review of Fluid Mechanics*, vol. 32, pp. 519–571, Jan. 2000. DOI: 10.1146/annurev.fluid.32.1.519.

[101] A. Van Garrel, “Development of a wind turbine aerodynamics simulation module,” *Energy research Centre of the Netherlands ECN Petten, The Netherlands*, Jan. 2003. DOI: http://dx.doi.org/10.13140/RG.2.1.2773.8000.

[102] S. Ananthan and J. G. Leishman, “Role of Filament Strain in the Free-Vortex Modeling of Rotor Wakes,” *Journal of the American Helicopter Society*, vol. 49, no. 2, pp. 176–191, Apr. 2004. DOI: 10.4050/jahs.49.176.

[103] S. K. Lam, A. Pitrou, and S. Seibert, “Numba: A llvm-based python jit compiler,” in *Proceedings of the Second Workshop on the LLVM Compiler Infrastructure in HPC*, 2015. [Online]. Available: https://numba.readthedocs.io/en/stable/user/5minguide.html.

[104] B. Giovanardi and A. van Zuijlen, *Hpc12 wiki*, /https://gitlab.tudelft.nl/hpc12/training, Access restricted to TU Delft students and employees, Jun. 2022.

[105] J. Katz and A. Plotkin, *Low-Speed Aerodynamics* (Cambridge Aerospace Series), 2nd ed. Cambridge University Press, 2001.

[106] M. Bhagwat and J. Leishman, “Technical note: Accuracy of straight-line segmentation applied to curvilinear vortex filaments,” *Journal of The American Helicopter Society - J AMER HELICOPTER SOC*, vol. 46, Apr. 2001. DOI: 10.4050/JAHS.46.166.

[107] M. Bhagwat and J. Leishman, “Generalized viscous vortex model for application to free-vortex wake and aeroacoustic calculations,” *58th Annual Forum and Technology Display of the American Helicopter Society International*, Jan. 2002.

[108] D. C. Lay, *Linear Algebra and Its Applications*. Addison Wesley Longman, Jan. 2012, ch. 2.7.

[109] W. Timmer and R. Rooij, “Summary of the delft university wind turbine dedicated airfoils,” *Journal of Solar Energy Engineering-transactions of The Asme - J SOL ENERGY ENG*, vol. 125, Jan. 2003. DOI: 10.1115/1.1626129.

[110] S. Gupta and J. Leishman, “Stability of Methods in the Free-Vortex Wake Analysis of Wind Turbines,” *42nd AIAA Aerospace Sciences Meeting and Exhibit*, Jan. 2004. DOI: 10.2514/6.2004-827.

[111] I. Turner-Trauring, *Understanding CPUs can help speed up Numba and NumPy code*, Jun. 2023. [Online]. Available: https://pythonspeed.com/articles/speeding-up-numba/.

[112] S. Ristov, R. Prodan, M. Gusev, *et al.*, “Superlinear speedup in hpc systems: Why and when?” In *2016 Federated conference on computer science and information systems (FEDCIS)*, IEEE, 2016.

[113] R. Martín-San-Román, P. Benito-Cia, J. Azcona-Armendáriz, *et al.*, "Validation of a free vortex filament wake module for the integrated simulation of multi-rotor wind turbines," *Renewable Energy*, vol. 179, pp. 1706–1718, 2021. DOI: https://doi.org/10.1016/j.renene.2021.07.147.

[114] F. Grasso, A. Van Garrel, and G. Schepers, "Development and Validation of Generalized Lifting Line Based Code for Wind Turbine Aerodynamics," *50th AIAA Aerospace Sciences Meeting including the New Horizons Forum and Aerospace Exposition*, Jan. 2011. DOI: 10.2514/6.2011-146.

[115] T. Sant, V. Del Campo, D. Micallef, *et al.*, "Evaluation of the lifting line vortex model approximation for estimating the local blade flow fields in horizontal-axis wind turbines," *Journal of Renewable and Sustainable Energy*, vol. 8, no. 2, Mar. 2016. DOI: 10.1063/1.4942785.

[116] F. Grasso, A. Van, G. Schepers, *et al.*, "Development and validation of generalized lifting line based code for wind turbine aerodynamics," *49th AIAA Aerospace Sciences Meeting, 30th ASME Wind Energy Symposium*, Jan. 2011. DOI: 10.2514/6.2011-146.

[117] J. Jonkman, S. Butterfield, W. Musial, *et al.*, "Definition of a 5-mw reference wind turbine for offshore system development," National Renewable Energy Lab.(NREL), Golden, CO (United States), Tech. Rep., 2009.

[118] B. Xu, T. Wang, Y. Yuan, *et al.*, "A Simplified Free Vortex Wake Model of Wind Turbines for Axial Steady Conditions," *Applied Sciences*, vol. 8, no. 6, 866, May 2018. DOI: 10.3390/app8060866.

[119] B. Dose, H. Rahimi, I. Herráez, *et al.*, "Fluid-structure coupled computations of the nrel 5-mw wind turbine by means of cfd," *Renewable Energy*, vol. 129, 2018. DOI: https://doi.org/10.1016/j.renene.2018.05.064.

A

V&V of K-TWIST

A.1. Consistency checks

This section presents the results from the consistency checks of the verification procedure. The K-TWIST framework correctly implements fundamental vortex-induced velocity behavior and reference frame conventions. Figure A.1 demonstrates that the K-TWIST framework correctly implements the Biot–Savart law and converges to the analytical solution of a semi-infinite vortex filament. Figure A.2 confirms that the vortex-induced velocity aligns with the right-hand rule, as expected from theory. Figure A.3 illustrates how the contributions of the different segments of a vortex ring element combine to produce the total induced velocity, in perfect agreement with analytical predictions. Finally, Figure A.4 confirms the orientation of the wind turbine rotation and presents the three-dimensional reference system of the simulation domain.

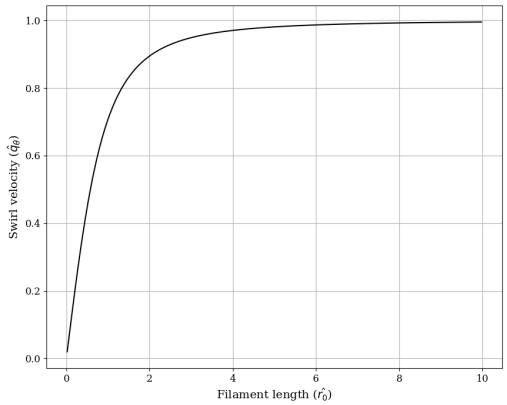

Figure A.1: Swirl velocity around an isolated vortex filament of increasing length

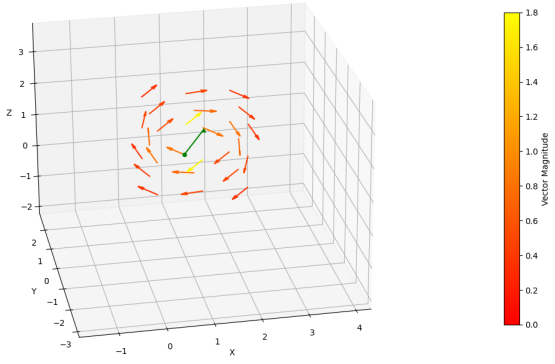

Figure A.2: Induced velocity field of an isolated vortex filament

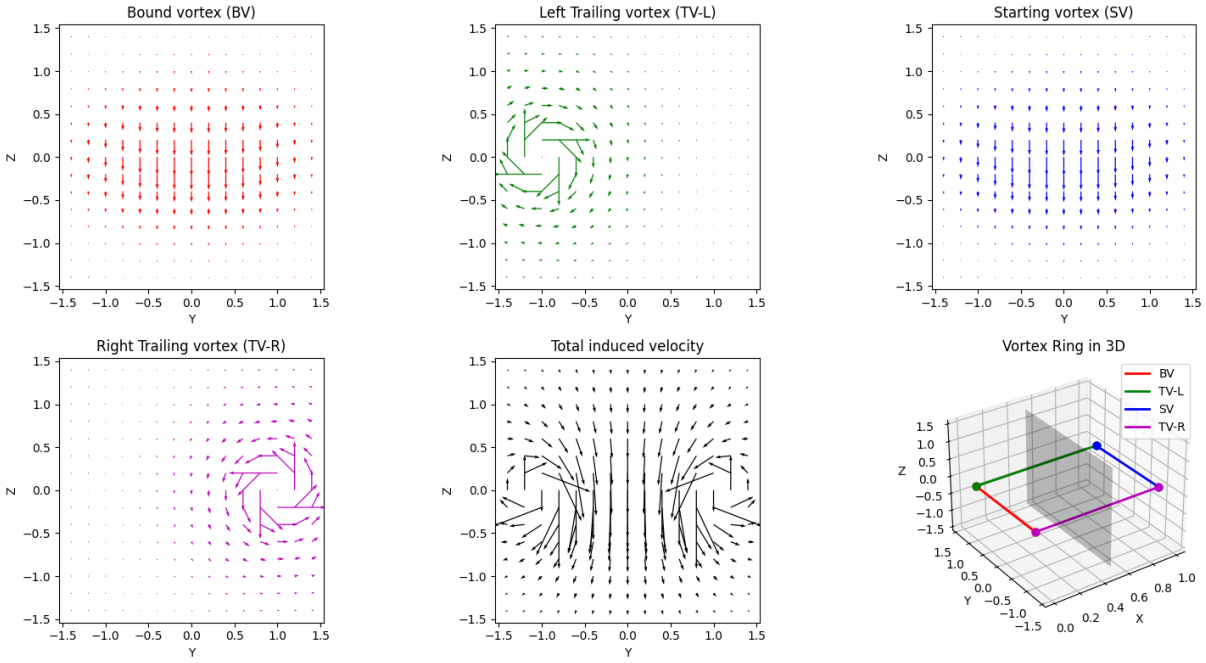

Figure A.3: Velocity field induced by a single three-dimensional vortex ring element

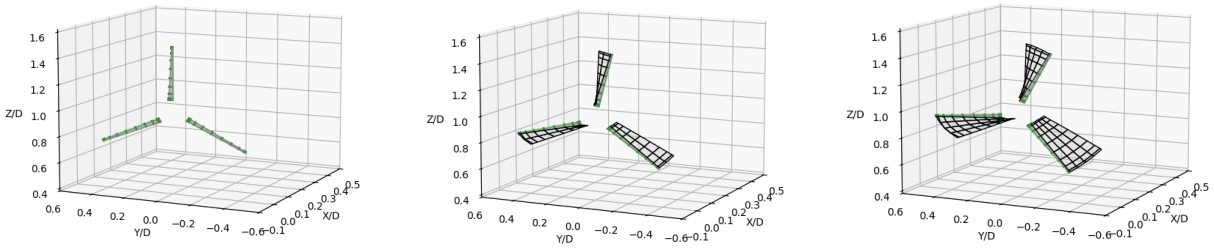

t=0 t=1 t=2

Figure A.4: Snapshots of the turbine wake geometry at three successive time steps

A.2. Configuration trials

This section shows the additional results from the set of aerodynamic configuration trials used to confirm the model's physical accuracy. Figure A.5 shows the distribution of bound circulation for a single, untwisted elliptical wing, confirming that zero angle of attack produces no lift, a positive angle matches the analytical elliptical distribution, and a negative angle shows the expected anti-symmetric response. Figure A.6 presents the wake geometry for a force-free helical rotor, in both 3D and side view, displaying the expected helical wake structure. Figure A.7 shows the bound circulation distribution for a three-bladed rotor at constant angular velocity. The model correctly transitions from the near-zero circulation of the force-free rotor to positive lift with a 10% increase in rotational speed. Figure A.8 and Figure A.9 illustrate the final configuration trial for a lightly loaded rotor ($C_T = 0.1$), showing the distribution of bound circulation and lift per unit span, respectively.

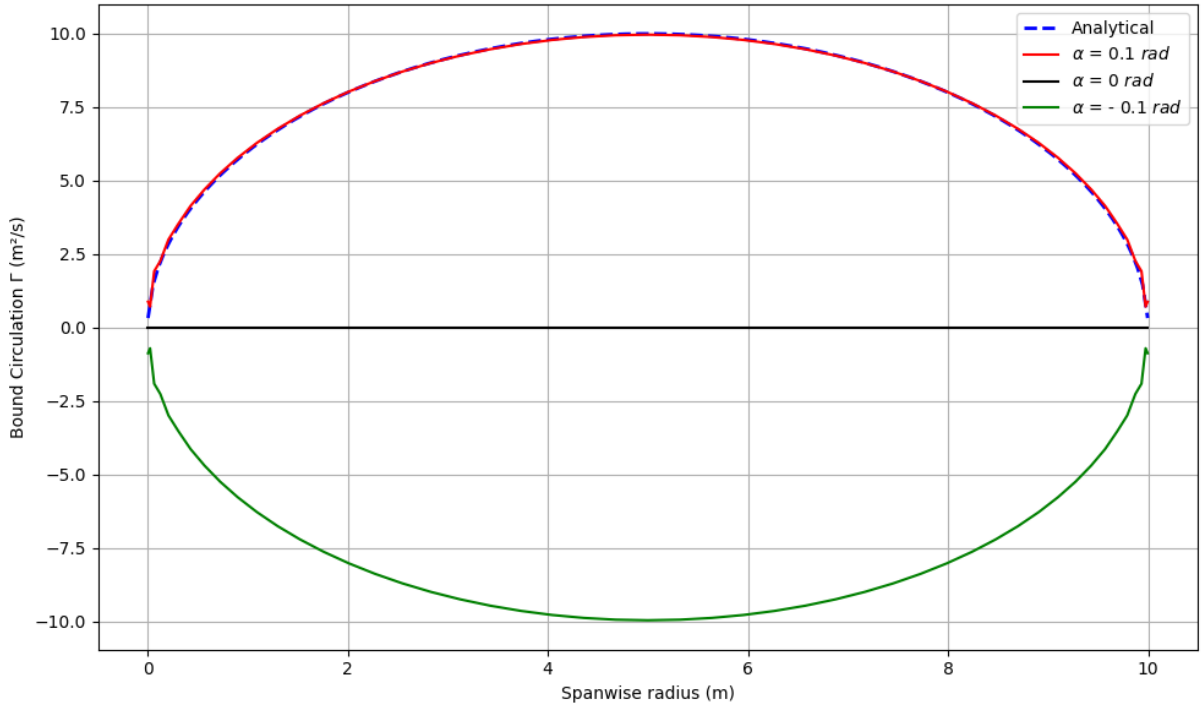

Figure A.5: Distribution of bound circulation for the test cases of a single, untwisted, elliptical wing

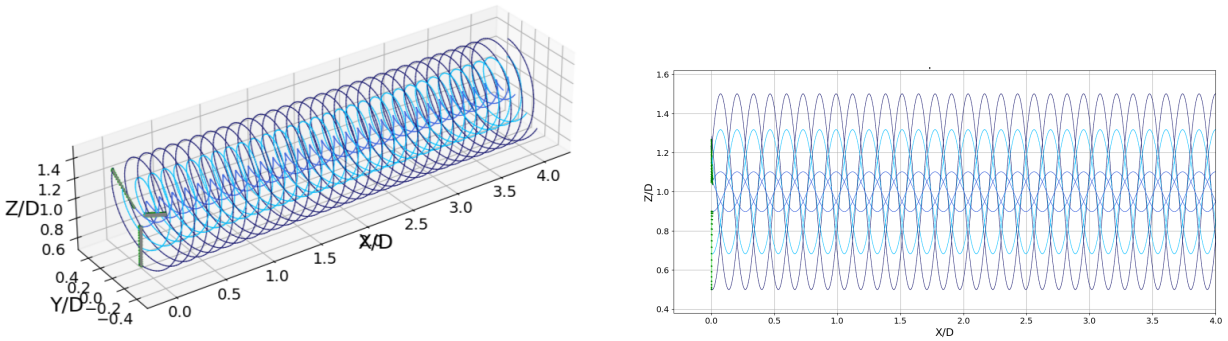

3D Side view

Figure A.6: Wake geometry of the test case of an helical, force-free rotor

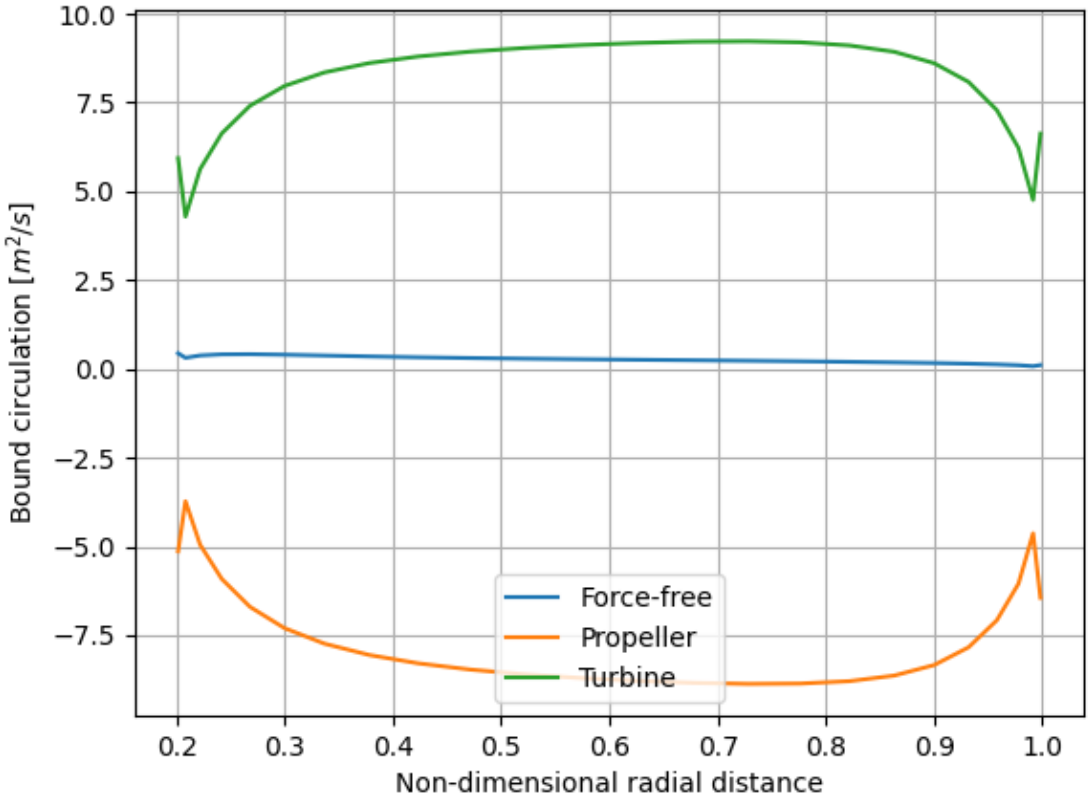

Figure A.7: Distribution of bound circulation for the test cases of a three-bladed rotor at constant angular velocity, while varying the tip speed ratio

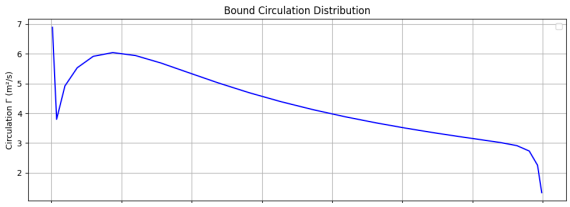

Figure A.8: Distribution of bound circulation for the test case of a constant, lightly loaded rotor ($C_T = 0.1$)

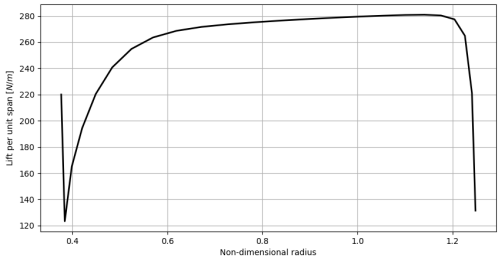

Figure A.9: Distribution of lift per unit span for the test case of a constant, lightly loaded rotor ($C_T = 0.1$)

A.3. Sensitivity analysis on CPU cores

This section further illustrates the effect of varying CPU cores on computational workload and parallel efficiency. Figure A.10 presents the evolution of computational workload, highlighting that the number of elements grows more rapidly with increasing CPU cores. This demonstrates the necessity of using normalized values when comparing results across different core counts. Figure A.11 shows the parallel efficiency, indicating that the relative speed-up deviates from the ideal linear scaling for higher numbers of cores, but remains significant.

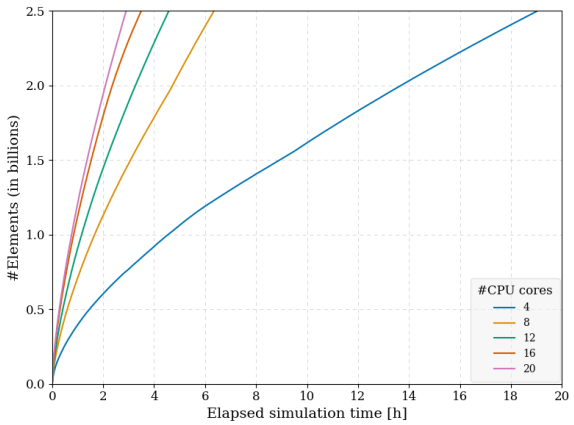

Figure A.10: Time evolution of the computational workload, expressed as the number of elements per time step

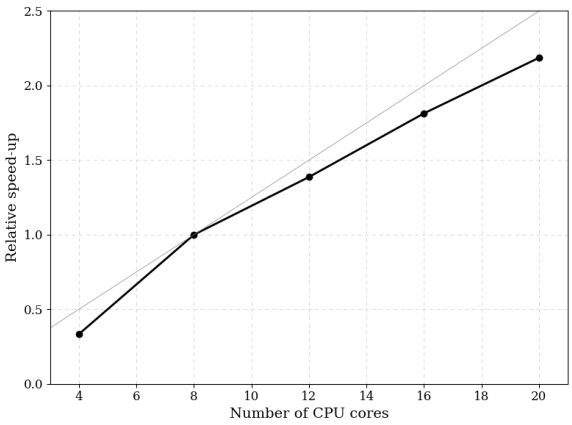

Figure A.11: Parallel efficiency expressed as relative speedup versus number of CPU cores, with respect to the 8-CPU runtime

A.4. Validation

This section presents the main validation results from the AWSM model by van Garrel [101]. Figure A.12 compares the spanwise normal force with wind tunnel experiments on the NREL Phase VI turbine, while Figure A.13 and Figure A.14 compare the downstream axial velocity with PIV measurements from the MEXICO project. These results confirm that the K-TWIST model is based on a validated mid-fidelity aerodynamic framework.

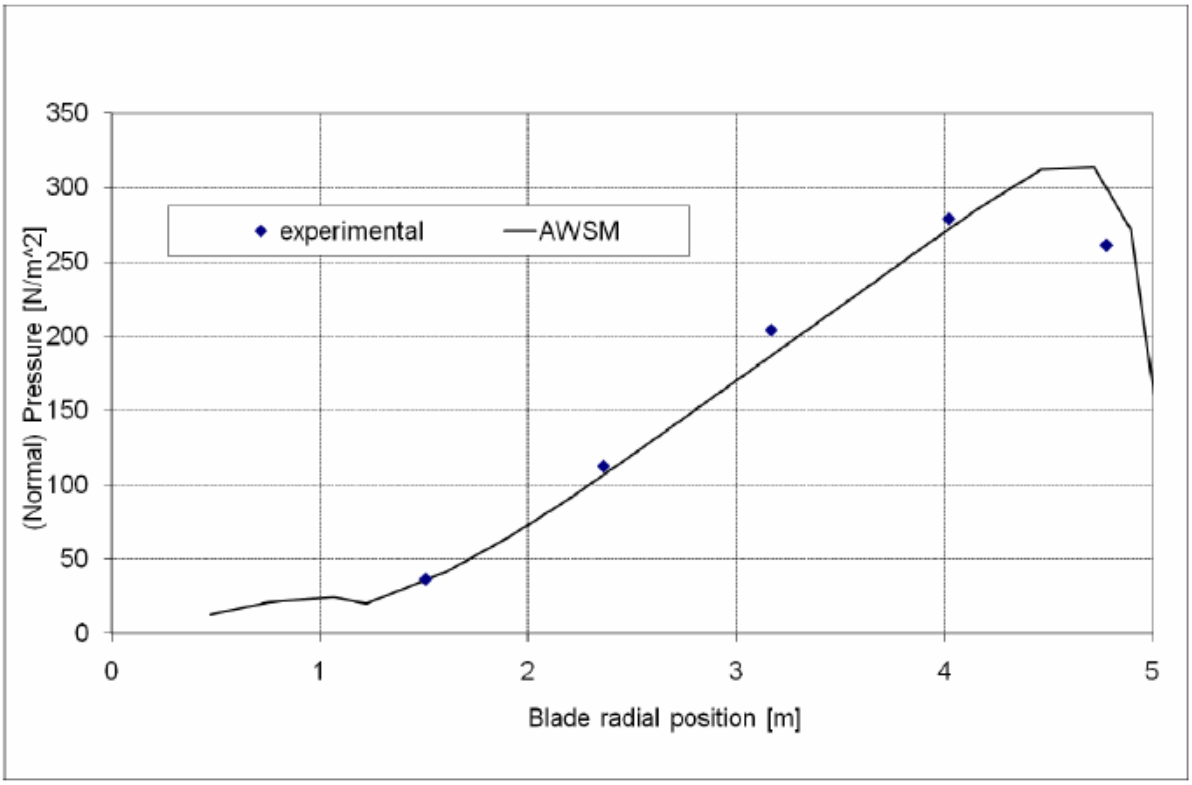

Figure A.12: Normal force along the spanwise position of the blade. Validation results of the AWSM model with wind tunnel experiments (NREL Phase VI wind turbine, below-stall, axial conditions). Adapted from [116]

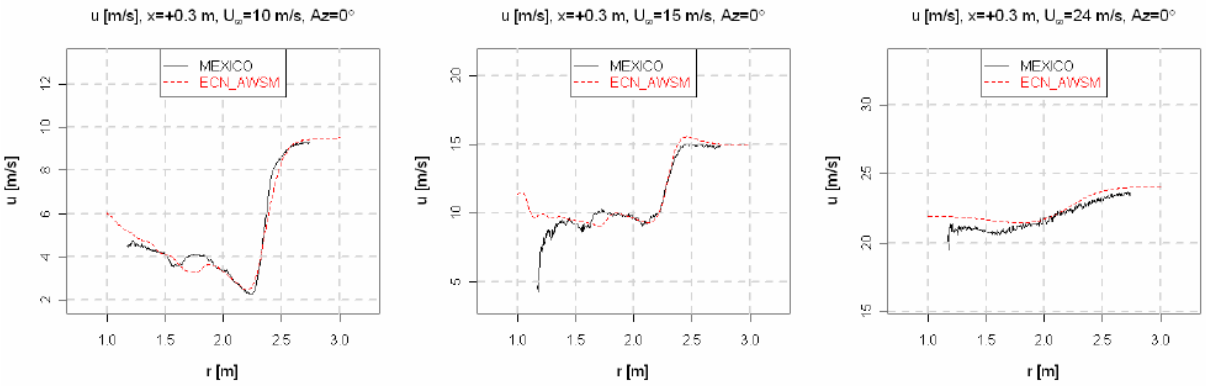

Figure A.13: Downstream radial distribution of the axial velocity component (u), at inflow conditions of $U_\infty = 10, 15, 24$. Validation results of the AWSM model with PIV measurements of the *MEXICO project* (below-stall, axial conditions). Adapted from [116]

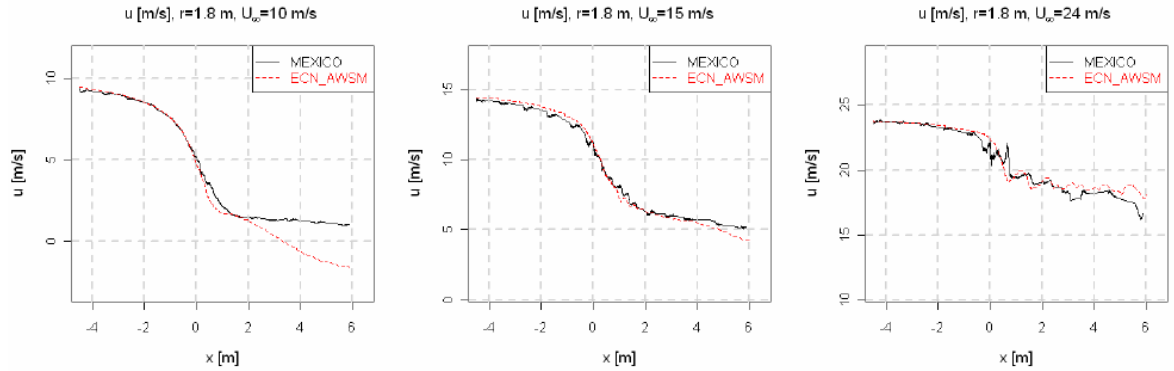

Figure A.14: Downstream radial distribution of the axial velocity component (u), at inflow conditions of $U_\infty = 10, 15, 24$ m/s. Validation results of the AWSM model with PIV measurements of the *MEXICO project* (below-stall, axial conditions). Adapted from [116]

B

Case study

B.1. NREL-2MW Wind turbine

This section of the appendix provides a detailed overview of the aerodynamic and geometric data that is used for the scaled 2MW wind turbine model of the case study Section 12.1. The data is derived from publicly available documentation of the NREL-5MW wind turbine [117], which is scaled down using scaling laws (Table 12.2). The main turbine characteristics are presented in Table B.1. For the complete overview of the design parameters, the reader is referred to the NREL reference data.

Table B.1: Turbine properties of the scaled NREL-2MW wind turbine model, adapted from [117]

Turbine property	Symbol	Value	Unit
Rotor Orientation		Upwind	
Number of blades	N_B	3	
Design tip-speed ratio	λ_{opt}	7	
Turbine rated power	P_R	2	MW
Cut-in wind speed	$U_{\text{cut-in}}$	3	m/s
Rated wind speed	U_{rated}	11.4	m/s
Cut-out wind speed	$U_{\text{cut-out}}$	25	m/s

B.1.1. Blade geometry

The blade geometry of the NREL-2MW wind turbine is specified by spanwise distribution functions. For computational efficiency, the blade is discretized into 15 spanwise segments, each represented by a distinctive cross-section. The 2D geometry of each slice is approximated by a chord length (c), twist angle (β_t) and airfoil type. These parameters are defined at the end points of the segment. Between the edges, the geometric parameters (c, β_t) are assumed to vary linearly with the radial distance r. This way, the blade can be described at any spanwise location by linear interpolation. The resulting blade geometry after scaling is summarized in Table B.2.

Table B.2: Blade geometry of the scaled NREL-2MW wind turbine model. Data is derived from publicly available data of the NREL-5MW wind turbine [117]

Number	Radial distance $\hat{r}_R$	Radial distance r [m]	Section length Δr [m]	Twist angle β_t [°]	Chord length c [m]	Airfoil type
1	0.0000	0.000	7.940	13.308	0.0000	-
2	0.2000	7.940	2.038	13.308	2.8709	DU40
3	0.2516	9.978	2.590	11.480	2.9308	DU35
4	0.3167	12.568	2.577	10.162	2.8085	DU35
5	0.3817	15.145	2.582	9.0110	2.6769	DU30
6	0.4468	17.727	2.588	7.7950	2.5244	DU25
7	0.5119	20.315	2.582	6.5440	2.3612	DU25
8	0.5770	22.897	2.580	5.3610	2.2063	DU21
9	0.6421	25.477	2.590	4.1880	2.0513	DU21
10	0.7071	28.067	2.585	3.1250	1.8963	NACA-64A17
11	0.7722	30.652	2.553	2.3190	1.7413	NACA-64A17
12	0.8373	33.205	2.175	1.5260	1.5863	NACA-64A17
13	0.8915	35.380	1.733	0.8630	1.4572	NACA-64A17
14	0.9349	37.113	1.704	0.3700	1.3142	NACA-64A17
15	0.9783	38.817	0.883	0.1060	0.8940	NACA-64A17

B.1.2. Aerodynamic airfoil data

The NREL-2MW wind turbine model consists of six different airfoil types: *DU40, DU35, DU30, DU25, DU21, NACA-64A17*, with varying shape and aerodynamic characteristics. The aerodynamic data is acquired from the open-access documentation of the NREL-5MW [117]. Here, the 2D aerodynamic data has already been corrected by the NREL for three-dimensional effects, such as rotational stall delay, finite aspect ratio and dynamic stall. For each airfoil type, a C_l-α table is provided in Tables B.3–B.8, respectively. For clarity, the aerodynamic drag and pitching moment coefficients are not shown, but can be found in the reference source. The main differences in the airfoil types are visualized in a combined lift curve plot in Figure B.1.

Table B.3: Airfoil data - DU40-A17

α	C_l	α	C_l	α	C_l	α	C_l
-180	0	-21	-0.706	4.5	0.776	25	1.872
-175	0.218	-20	-0.685	5	0.841	26	1.881
-170	0.397	-19	-0.662	5.5	0.904	28	1.894
-160	0.642	-18	-0.635	6	0.967	30	1.904
-155	0.715	-17	-0.605	6.5	1.027	32	1.915
-150	0.757	-16	-0.571	7	1.084	35	1.929
-145	0.772	-15	-0.534	7.5	1.14	40	1.903
-140	0.762	-14	-0.494	8	1.193	45	1.82
-135	0.731	-13	-0.452	8.5	1.242	50	1.69
-130	0.68	-12	-0.407	9	1.287	55	1.522
-125	0.613	-11	-0.36	9.5	1.333	60	1.323
-120	0.532	-10	-0.311	10	1.368	65	1.106
-115	0.439	-8	-0.208	10.5	1.4	70	0.88
-110	0.337	-6	-0.111	11	1.425	75	0.658
-105	0.228	-5.5	-0.09	11.5	1.449	80	0.449
-100	0.114	-5	-0.072	12	1.473	85	0.267
-95	-0.002	-4.5	-0.065	12.5	1.494	90	0.124
-90	-0.12	-4	-0.054	13	1.513	95	0.002
-85	-0.236	-3.5	-0.017	13.5	1.538	100	-0.118
-80	-0.349	-3	0.003	14.5	1.587	105	-0.235
-75	-0.456	-2.5	0.014	15	1.614	110	-0.348
-70	-0.557	-2	0.009	15.5	1.631	115	-0.453
-65	-0.647	-1.5	0.004	16	1.649	120	-0.549
-60	-0.727	-1	0.036	16.5	1.666	125	-0.633
-55	-0.792	-0.5	0.073	17	1.681	130	-0.702
-50	-0.842	0	0.137	17.5	1.699	135	-0.754
-45	-0.874	0.5	0.213	18	1.719	140	-0.787
-40	-0.886	1	0.292	19	1.751	145	-0.797
-35	-0.875	1.5	0.369	19.5	1.767	150	-0.782
-30	-0.839	2	0.444	20.5	1.798	155	-0.739
-25	-0.777	2.5	0.514	21	1.81	160	-0.664
-24	-0.761	3	0.58	22	1.83	170	-0.41
-23	-0.744	3.5	0.645	23	1.847	175	-0.226
-22	-0.725	4	0.71	24	1.861	180	0

Table B.4: Airfoil data - DU35-A17

α	C_l	α	C_l	α	C_l	α	C_l
-180	0	-21	-0.714	4.5	0.809	25	1.546
-175	0.223	-20	-0.693	5	0.875	26	1.539
-170	0.405	-19	-0.671	5.5	0.941	28	1.527
-160	0.658	-18	-0.648	6	1.007	30	1.522
-155	0.733	-17	-0.624	6.5	1.071	32	1.529
-150	0.778	-16	-0.601	7	1.134	35	1.544
-145	0.795	-15	-0.579	7.5	1.198	40	1.529
-140	0.787	-14	-0.559	8	1.26	45	1.471
-135	0.757	-13	-0.539	8.5	1.318	50	1.376
-130	0.708	-12	-0.519	9	1.368	55	1.249
-125	0.641	-11	-0.499	9.5	1.422	60	1.097
-120	0.56	-10	-0.48	10	1.475	65	0.928
-115	0.467	-8	-0.385	10.5	1.523	70	0.75
-110	0.365	-6	-0.359	11	1.57	75	0.57
-105	0.255	-5.5	-0.36	11.5	1.609	80	0.396
-100	0.139	-5	-0.355	12	1.642	85	0.237
-95	0.021	-4.5	-0.307	12.5	1.675	90	0.101
-90	-0.098	-4	-0.246	13	1.7	95	-0.022
-85	-0.216	-3.5	-0.24	13.5	1.717	100	-0.143
-80	-0.331	-3	-0.163	14.5	1.712	105	-0.261
-75	-0.441	-2.5	-0.091	15	1.703	110	-0.374
-70	-0.544	-2	-0.019	15.5	1.671	115	-0.48
-65	-0.638	-1.5	0.052	16	1.649	120	-0.575
-60	-0.72	-1	0.121	16.5	1.621	125	-0.659
-55	-0.788	-0.5	0.196	17	1.598	130	-0.727
-50	-0.84	0	0.265	17.5	1.571	135	-0.778
-45	-0.875	0.5	0.335	18	1.549	140	-0.809
-40	-0.889	1	0.404	19	1.544	145	-0.818
-35	-0.88	1.5	0.472	19.5	1.549	150	-0.8
-30	-0.846	2	0.54	20.5	1.565	155	-0.754
-25	-0.784	2.5	0.608	21	1.565	160	-0.677
-24	-0.768	3	0.674	22	1.563	170	-0.417
-23	-0.751	3.5	0.742	23	1.558	175	-0.229
-22	-0.733	4	0.71	24	1.552	180	0

Table B.5: Airfoil data - DU30-A17

α	C_l	α	C_l	α	C_l	α	C_l
-180	0	-21	-0.963	4.5	0.879	25	1.354
-175	0.274	-20	-1.013	5	0.944	26	1.332
-170	0.547	-19	-1.067	5.5	1.008	28	1.293
-160	0.685	-18	-1.125	6	1.072	30	1.265
-155	0.766	-17	-1.185	6.5	1.135	32	1.253
-150	0.816	-16	-1.245	7	1.197	35	1.264
-145	0.836	-15	-1.29	7.5	1.256	40	1.258
-140	0.832	-14	-1.229	8	1.305	45	1.217
-135	0.804	-14	-1.148	9	1.39	50	1.146
-130	0.756	-12	-1.052	9.5	1.424	55	1.049
-125	0.69	-11	-0.965	10	1.458	60	0.932
-120	0.609	10	-0.867	10.5	1.488	65	0.799
-115	0.515	-8	-0.756	11	1.512	70	0.657
-110	0.411	-6	-0.525	11.5	1.533	75	0.509
-105	0.3	-5.5	-0.451	12	1.549	80	0.362
-100	0.182	-5	-0.382	12.5	1.558	85	0.221
-95	0.061	-4.5	-0.314	13	1.47	90	0.092
-90	-0.061	-4	-0.251	13.5	1.398	95	-0.03
-85	-0.183	-3.5	-0.189	14	1.354	100	-0.15
-80	-0.302	-3	-0.12	14.5	1.336	105	-0.267
-75	-0.416	-2.5	-0.051	15	1.333	110	-0.379
-70	-0.523	-2	0.017	15.5	1.326	115	-0.483
-65	-0.622	-1.5	0.085	16	1.329	120	-0.578
-60	-0.708	-1	0.152	16.5	1.326	125	-0.66
-55	-0.781	-0.5	0.219	17	1.321	130	-0.727
-50	-0.838	0	0.288	17.5	1.331	135	-0.777
-45	-0.877	0.5	0.354	18	1.333	140	-0.807
-40	-0.895	1	0.421	19	1.362	145	-0.815
-35	-0.889	1.5	0.487	19.5	1.382	150	-0.797
-30	-0.858	2	0.554	20.5	1.426	155	-0.75
-25	-0.832	2.5	0.619	21	1.437	160	-0.673
-24	-0.852	3	0.685	22	1.418	170	-0.547
-23	-0.882	3.5	0.749	23	1.397	175	-0.274
-22	-0.919	4	0.815	24	1.376	180	0

Table B.6: Airfoil data - DU25-A17

α	C_l	α	C_l	α	C_l	α	C_l
-180	0	-20	-0.815	4.5	1.013	24	1.251
-175	0.368	-19	-0.833	5	1.062	25	1.215
-170	0.735	-18	-0.854	6	1.161	26	1.181
-160	0.695	-17	-0.879	6.5	1.208	28	1.12
-155	0.777	-16	-0.905	7	1.254	30	1.076
-150	0.828	-15	-0.932	7.5	1.301	32	1.056
-145	0.85	-14	-0.959	8	1.336	35	1.066
-140	0.846	-13	-0.985	8.5	1.369	40	1.064
-135	0.818	-12	-0.953	9	1.4	45	1.035
-130	0.771	-11	-0.9	9.5	1.428	50	0.98
-125	0.705	-10	-0.827	10	1.442	55	0.904
-120	0.624	-9	-0.753	10.5	1.427	60	0.81
-115	0.53	-8.5	-0.691	11	1.374	65	0.702
-110	0.426	-7.5	-0.555	11.5	1.316	70	0.582
-105	0.314	-6.5	-0.413	12	1.277	75	0.456
-100	0.195	-5.5	-0.271	12.5	1.25	80	0.326
-95	0.073	-5	-0.22	13	1.246	85	0.197
-90	-0.05	-4.5	-0.152	13.5	1.247	90	0.072
-85	-0.173	-4	-0.084	14	1.256	95	-0.05
-80	-0.294	-3.5	-0.018	14.5	1.26	100	-0.17
-75	-0.409	-3	0.049	15	1.271	105	-0.287
-70	-0.518	-2.5	0.115	15.5	1.281	110	-0.399
-65	-0.617	-2	0.181	16	1.289	115	-0.502
-60	-0.706	-1.5	0.247	16.5	1.294	120	-0.596
-55	-0.78	-1	0.312	17	1.304	125	-0.677
-50	-0.839	-0.5	0.377	17.5	1.309	130	-0.743
-45	-0.879	0	0.444	18	1.315	135	-0.792
-40	-0.898	0.5	0.508	18.5	1.32	140	-0.821
-35	-0.893	1	0.573	19	1.33	145	-0.826
-30	-0.862	1.5	0.636	19.5	1.343	150	-0.806
-25	-0.803	2	0.701	20	1.354	155	-0.758
-24	-0.792	2.5	0.765	20.5	1.359	160	-0.679
-23	-0.789	3	0.827	21	1.36	170	-0.735
-22	-0.792	3.5	0.89	22	1.325	175	-0.368
-21	-0.801	4	0.952	23	1.288	180	0

Table B.7: Airfoil data - DU21-A17

α	C_l	α	C_l	α	C_l	α	C_l
-180	0	-20	-0.869	4.5	1.046	24	1.182
-175	0.394	-19	-0.899	5	1.095	25	1.136
-170	0.788	-18	-0.931	5.5	1.145	26	1.093
-160	0.67	-17	-0.964	6	1.192	28	1.017
-155	0.749	-16	-0.999	6.5	1.239	30	0.962
-150	0.797	-15	-1.033	7	1.283	32	0.937
-145	0.818	-13.5	-1.05	7.5	1.324	35	0.947
-140	0.813	-12	-0.953	8	1.358	40	0.95
-135	0.786	-11	-0.9	8.5	1.385	45	0.928
-130	0.739	-10	-0.827	9.5	1.401	50	0.884
-125	0.675	-8	-0.536	10	1.358	55	0.821
-120	0.596	-7.5	-0.467	10.5	1.313	60	0.74
-115	0.505	-7	-0.393	11	1.287	65	0.646
-110	0.403	-6.5	-0.311	11.5	1.274	70	0.54
-105	0.294	-6	-0.245	12	1.272	75	0.425
-100	0.179	-5.5	-0.178	12.5	1.273	80	0.304
-95	0.06	-5	-0.113	13	1.273	85	0.179
-90	-0.06	-4.5	-0.048	13.5	1.273	90	0.053
-85	-0.179	-4	0.016	14	1.272	95	-0.073
-80	-0.295	-3.5	0.08	14.5	1.273	100	-0.198
-75	-0.407	-3	0.145	15	1.275	105	-0.319
-70	-0.512	-2.5	0.208	15.5	1.281	110	-0.434
-65	-0.608	-2	0.27	16	1.284	115	-0.541
-60	-0.693	-1.5	0.333	16.5	1.296	120	-0.637
-55	-0.764	-1	0.396	17	1.306	125	-0.72
-50	-0.82	-0.5	0.458	17.5	1.308	130	-0.787
-45	-0.857	0	0.521	18	1.308	135	-0.836
-40	-0.875	0.5	0.583	18.5	1.308	140	-0.864
-35	-0.869	1	0.645	19	1.308	145	-0.869
-30	-0.838	1.5	0.706	19.5	1.307	150	-0.847
-25	-0.791	2	0.768	20	1.311	155	-0.795
-24	-0.794	2.5	0.828	20.5	1.325	160	-0.711
-23	-0.805	3	0.888	21	1.324	170	-0.788
-22	-0.821	3.5	0.948	22	1.277	175	-0.394
-21	-0.843	4	0.996	23	1.229	180	0

Table B.8: Airfoil data - NACA-64A17

α	C_l	α	C_l	α	C_l	α	C_l
-180	0	-23	-0.89	8	1.257	30	0.926
-175	0.374	-22	-0.911	8.5	1.293	32	0.855
-170	0.749	-21	-0.934	9	1.326	35	0.8
-160	0.659	-20	-0.958	9.5	1.356	40	0.804
-155	0.736	-19	-0.982	10	1.382	45	0.793
-150	0.783	-18	-1.005	10.5	1.4	50	0.763
-145	0.803	-17	-1.082	11	1.415	55	0.717
-140	0.798	-16	-1.113	11.5	1.425	60	0.656
-135	0.771	-15	-1.105	12	1.434	65	0.582
-130	0.724	-14	-1.078	12.5	1.443	70	0.495
-125	0.66	-13.5	-1.053	13	1.451	75	0.398
-120	0.581	-13	-1.015	13.5	1.453	80	0.291
-115	0.491	-12	-0.904	14	1.448	85	0.176
-110	0.39	-11	-0.807	14.5	1.444	90	0.053
-105	0.282	-10	-0.711	15	1.445	95	-0.074
-100	0.169	-9	-0.595	15.5	1.447	100	-0.199
-95	0.052	-8	-0.478	16	1.448	105	-0.321
-90	-0.067	-7	-0.375	16.5	1.444	110	-0.436
-85	-0.184	-6	-0.264	17	1.438	115	-0.543
-80	-0.299	-5	-0.151	17.5	1.439	120	-0.64
-75	-0.409	-4	-0.017	18	1.448	125	-0.723
-70	-0.512	-3	0.088	18.5	1.452	130	-0.79
-65	-0.606	-2	0.213	19	1.448	135	-0.84
-60	-0.689	-1	0.328	19.5	1.438	140	-0.868
-55	-0.759	0	0.442	20	1.428	145	-0.872
-50	-0.814	1	0.556	21	1.401	150	-0.85
-45	-0.85	2	0.67	22	1.359	155	-0.798
-40	-0.866	3	0.784	23	1.3	160	-0.714
-35	-0.86	4	0.898	24	1.22	170	-0.749
-30	-0.829	5	1.011	25	1.168	175	-0.374
-25	-0.853	6	1.103	26	1.116	180	0
-24	-0.87	7	1.181	28	1.015		

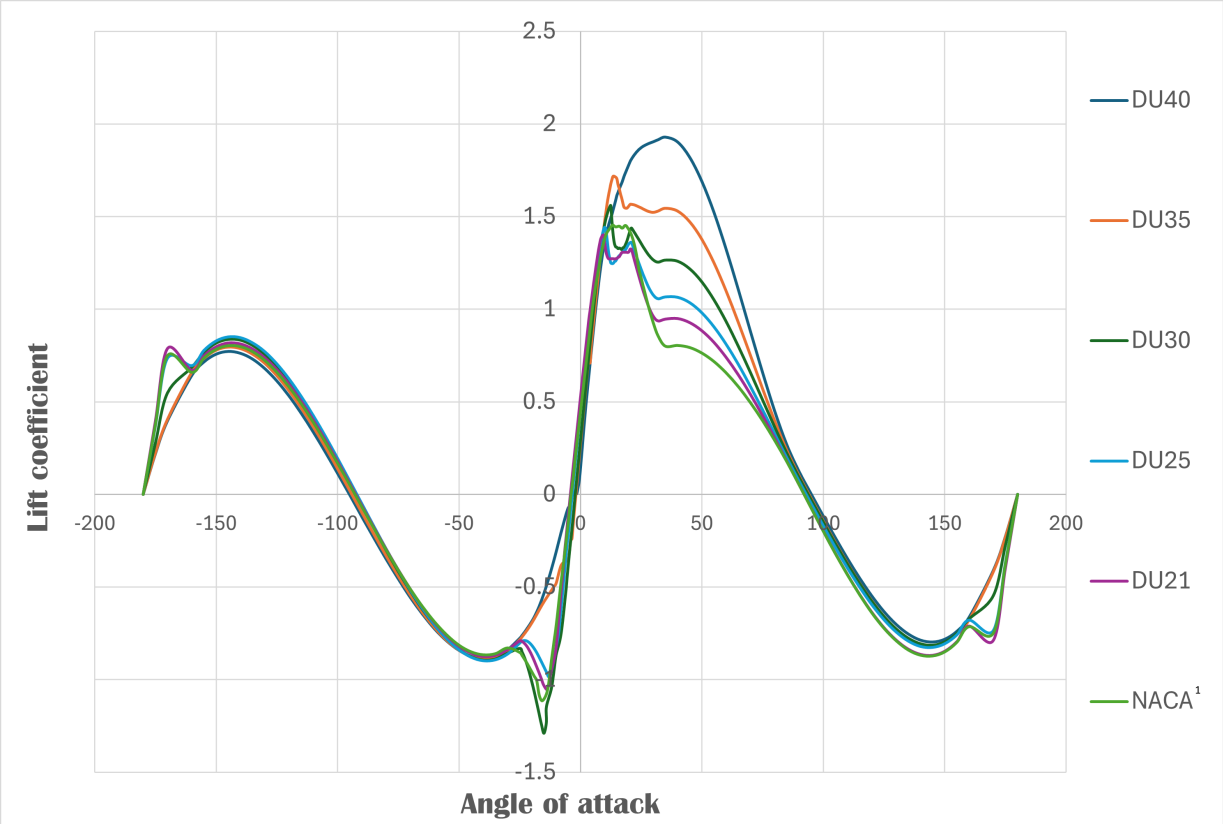

Figure B.1: Three-dimensional lift curve ($C_l - \alpha$) for the different airfoil types used in the scaled NREL-2MW model, adapted from [117] Each airfoil has a relative thickness of 17%. [1] The ”NACA” airfoil refers to the NACA-64A17 type.

B.2. Ram-air kite model

B.2.1. Wing geometry

B.2.2. Aerodynamic airfoil data

Table B.9: Airfoil data - NACA-2412

α	C_l	α	C_l	α	C_l	α	C_l
-180	0.0000	-13	-1.2095	6	0.9089	25	1.5242
-170	0.4268	-12	-1.0911	7	1.0176	30	1.3344
-160	0.8536	-11	-0.9854	8	1.1208	40	1.0753
-150	0.9340	-10	-0.8808	9	1.2241	50	0.8670
-140	0.7527	-9	-0.7735	10	1.3249	60	0.6589
-130	0.6069	-8	-0.6632	11	1.4228	70	0.4390
-120	0.4612	-7	-0.5515	12	1.5168	80	0.2137
-110	0.3073	-6	-0.4390	13	1.6050	90	0.0000
-100	0.1496	-5	-0.3259	14	1.6772	100	-0.1496
-90	0.0000	-4	-0.2124	15	1.7398	110	-0.3073
-80	-0.1496	-3	-0.0987	16	1.7910	120	-0.4612
-70	-0.3073	-2	0.0153	17	1.8310	130	-0.6069
-60	-0.4612	-1	0.1294	18	1.8652	140	-0.7527
-50	-0.6069	0	0.2436	19	1.8825	150	-0.9340
-40	-0.7527	1	0.3576	20	1.8786	160	-0.8536
-30	-0.9340	2	0.4700	21	1.8476	170	-0.4268
-20	-1.2413	3	0.5808	22	1.7865	180	0.0000
-15	-1.4157	4	0.6889	23	1.7114		
-14	-1.3234	5	0.7911	24	1.6215		

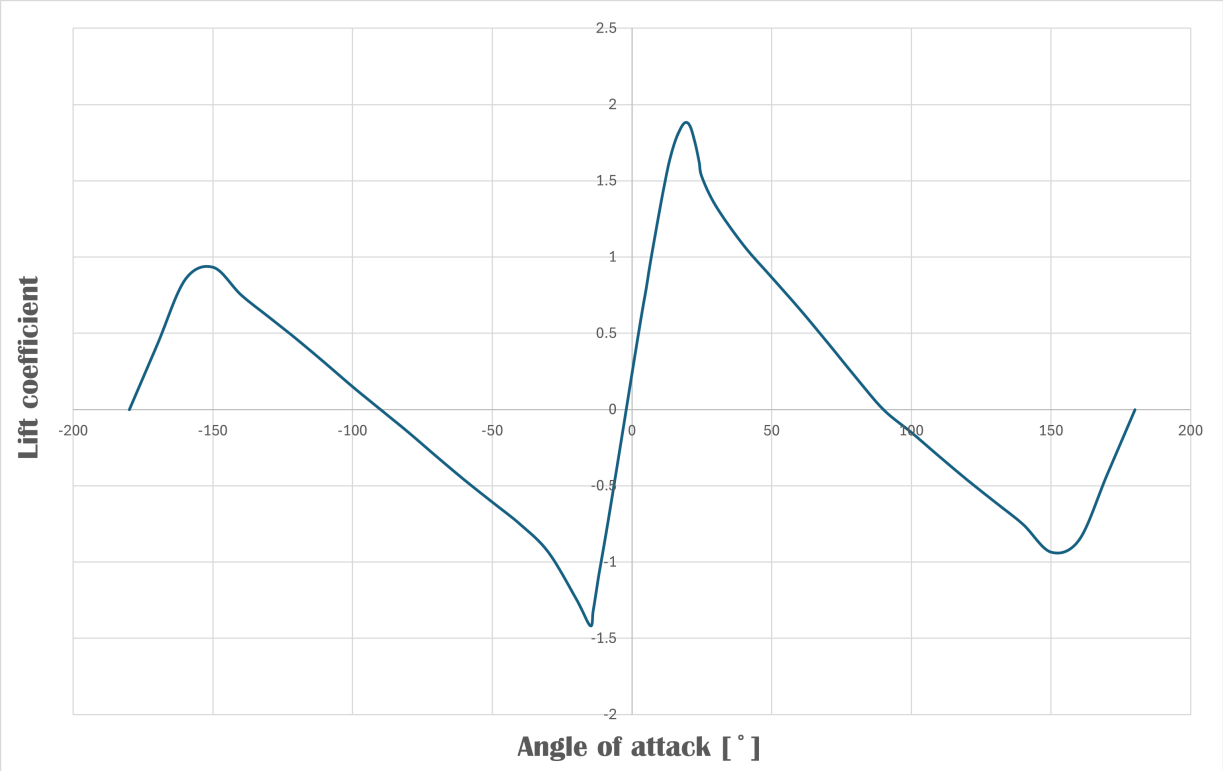

Figure B.2: Three-dimensional lift curve ($C_l - \alpha$) for the NACA-2412 airfoil type used in the RAM-air kite model. Two-dimensional polar data extrapolated using the Viterna method.